Preparation of Inorganic Nanostructured Materials by Stepwise Deposition Using Silica Templates

シリカ鋳型を用いた段階的析出による
無機ナノ構造体の合成

February, 2016

Masaki Kitahara

北原真樹

Preparation of Inorganic Nanostructured Materials by Stepwise Deposition Using Silica Templates

シリカ鋳型を用いた段階的析出による
無機ナノ構造体の合成

February, 2016

Waseda University
Graduate School of Advanced Science and Engineering
Department of Applied Chemistry
Research on Inorganic Synthetic Chemistry

Masaki Kitahara
北原真樹

Preface

Inorganic nanostructured materials are attractive because novel and unique functions can be obtained due to their high surface to volume ratios and quantum confinement effects. Inorganic nanostructured materials are potentially and practically applicable for many applications, such as catalysts, energy materials, electronic devices, and adsorbents. Because the functions of inorganic nanostructured materials depend on the composition, size, structure, and morphology, their precise control is quite important to obtain desired functions for targeted applications. Therefore, development of synthetic chemistry of inorganic nanostructured materials is highly required.

A templating method using inorganic compounds as a template is a powerful route for such precise control. In this method, inorganic nanostructured materials replicated from templates are typically prepared *via* the following three processes; 1) infiltration of precursor into spaces/pores of template, 2) deposition of targeted inorganic compounds within the template, 3) removal of template. Uncontrolled crystal growth of inorganic compounds during the deposition process is strongly inhibited by rigid frameworks of template. Therefore, the method is applicable to various compositions. Among a wide range of inorganic compounds, silica-based compounds with well-defined nanostructures, such as zeolites, mesoporous silica, and silica colloidal crystals, are useful as templates because their sizes, structures, and morphologies can be controlled uniformly and variously. However, the controllability of some parameters (e.g. compositions and crystallite sizes) which are deeply related to deposition processes is still low even by using the templating method.

In this thesis, the use of stepwise deposition within the silica templates for the preparation of inorganic nanostructured materials is described. Because silica templates

can accommodate inorganic compounds, the compounds can be deposited within the templates stepwisely. The appropriate compound is deposited within the templates and/or on their inner surfaces, and subsequent compounds which constitute main frameworks of final product are deposited. This thesis shows the usefulness of the stepwise depositions for precise preparation of inorganic nanostructured materials.

This thesis is composed of six chapters as follows.

Chapter 1 describes the general introduction and background of inorganic nanostructured materials. Preparative methods, features and applications of inorganic nanostructured materials are firstly reviewed. Then, silica templates and characteristics of inorganic nanostructured materials prepared by using such templates are described. After that, deposition methods applicable to the templating method are reviewed. Finally, the current issues of the preparation using the silica templates and significance of this thesis are described.

Chapter 2 describes the preparation of three-dimensional ordered mesoporous TiO_2 with single crystalline frameworks using stepwise deposition of TiO_2 within the silica colloidal crystal template. First, a small amount of TiO_2 was deposited within the template by thermal treatment of titania-incorporated template. Then, TiO_2 with relatively large crystallite sizes was hydrothermally deposited within the template. Because the initially deposited TiO_2 worked as nuclei, the inside deposition using the hydrothermal reaction, which had been unsuitable for the templating method, was successful. By removal of the template, single crystalline ordered mesoporous TiO_2 replicated from the template was obtained. In addition, Nb was doped into the TiO_2 frameworks for tuning their properties, resulting in the formation of not only three-dimensional mesoporous structures replicated from the template but also plate-like

nanostructures with ordered mesoscale dimples. The crystalline phases of mesoporous TiO_2 and plate-like nanostructured TiO_2 were rutile and anatase, respectively. The ratios of the products were controlled by varying the amount of Nb-doping. The unique dimpled structure was formed by the deposition of TiO_2 on the surface of the template, which was shown by scanning electron microscopy (SEM) observation of the products prior to the template removal. This was probably because the deposition occurred prior to the diffusion of titanium species into the template.

Chapter 3 describes the stepwise deposition of TiO_2 and C for preparation of TiO_2 nanoparticles supported mesoporous carbon (mesoporous C/TiO_2). In order to prepare TiO_2 nanoparticles within mesoporous carbon, thermal decomposition of a titanium precursor incorporated into mesoporous carbon is conventionally performed. However, this method suffers from both outer depositions and pore blockings when the amount of a titanium precursor incorporated into the template increases for higher loading amount of TiO_2. Therefore, this chapter has demonstrated the novel preparative method *via* surface deposition of TiO_2 and subsequent deposition of C within two-dimensional hexagonal mesoporous silica (SBA-15). TiO_2 was initially deposited on the surface of the template through reactions between titanium isopropoxide and the surface silanol groups. Then, 2,3-dihydroxynaphthalene, used as a carbon precursor, incorporated into the template was carbonized by high temperature heat treatment under N_2 gas flow. Finally, the final products were obtained by removal of the template. Crystalline TiO_2 nanoparticles were formed within mesoporous carbon as observed by the transmission electron microscopy. Because TiO_2 was immobilized on the surfaces, the outer depositions and the pore blockings would be suppressed.

Chapter 4 describes the stepwise deposition of Au and Pt within SBA-15 for

the preparation of mesoporous bimetallic Au-Pt with a phase segregated heterostructure. Chapter 4 consists of two sections as follows.

Section 4.1 describes a novel deposition method of Au within SBA-15 and control of its particle shape within SBA-15. The previous deposition methods typically require surface organic modifications for inside deposition of Au. This section has demonstrated that the use of hexane and 1,1,3,3-tetramethyldisiloxane (TMDS) as a solvent and reducing agent, respectively, enable Au deposition exclusively within the SBA-15 without using the surface modifications. In non-polar solvent such as hexane, the interaction between polar silanol groups and Au precursor becomes stronger, resulting in the suppression of Au species, and consequently, the inside deposition. In addition, the selective formation of Au nanorods replicated from the pore shape of the template or Au nanoparticles was achieved by performing the deposition in the absence or presence of hexadecyltrimethylammonium bromide (C_{16}TMAB). The formation of Au nanoparticles under the presence of C_{16}TMAB was explained by the suppression of the migration and growth of Au species within SBA-15 due to the formation of a complex between a Au precursor and C_{16}TMAB.

Section 4.2 describes the preparation of mesoporous bimetallic Au-Pt with a phase segregated heterostructure through Pt deposition within the Au nanoparticles incorporated SBA-15. Higher loading amount of Au nanoparticles than that of the previous reports was achieved by repeating the deposition process of Au described in section 4.1. The crystal growth of Pt proceeded from the surface of the Au nanoparticles due to a mild condition using vapor of dimethylamine borane. The EDX spectral mappings of the products after the template removal showed that the frameworks were composed of Au nanoparticles sandwiched between Pt nanowires. The measurements of

pre-adsorbed (CO_{ad}) stripping voltammetry and cyclic voltammetry measurements showed that the Au-Pt heterojunctions were formed and the surfaces of Au, Pt, and the heterojunction were electrochemically active. From these data, the usefulness of mesoporous silica as not only a template but also a reaction field of formation of metal-metal heterojunction has been demonstrated.

Chapter 5 describes the applicability of the deposition method described in section 4.1 to Bi deposition within SBA-15 and the preparation of Bi nanowires. After introduction of a Bi precursor into the mesopores of SBA-15, the Bi deposition was performed by using hexane and TMDS, resulting in the formation of Bi nanowires replicated from the pore shape of the template. The deposition using the same condition was successful for the template with different pore sizes between *ca.* 2.7 nm to 8.1 nm. After the template removal, Bi nanowires with 8.4 nm, 7.5 nm, and 6.5 nm in mean diameters were obtained, although the morphology was collapsed for the products prepared by using SBA-15 with smaller diameters. The obtained nanowires were one of the smallest Bi nanowires. Also, the obtained nanowires were non-crystalline. Considering that bulk Bi particles formed by the outer deposition were crystalline, the non-crystalline nature was related to the depositions within the confined nanospaces of the templates.

Chapter 6 describes the conclusion of this thesis. This thesis shows the usefulness of the stepwise depositions within the silica templates for precise preparation of inorganic nanostructured materials. The concept of this thesis will contribute to further precise design of inorganic nanostructured materials.

Contents

Chapter 1

General Introduction

Chapter 1

1.1 Introduction

For the last several decades, numerous studies have been reported on inorganic nanostructured materials. Nanostructured materials are defined as compounds with at least one dimension in a range between 1 nm to 100 nm, and can be classified on the basis of the number of their dimension outside the range (zero-dimensional (0D), one-dimensional (1D), two-dimensional (2D)).[1] Three-dimensional (3D) nanostructured materials generally indicate a 3D assembly of 0D, 1D, or 2D nanostructured materials.

The nanostructured materials are potentially applicable in various fields because of their unique properties, such as optical, magnetic, and catalytic properties.[2] Because their properties are influenced by many parameters (e.g. composition, crystallinity, crystallite size, particle shape, etc.), development of the preparative methods is quite important to obtain desired properties.

Among the various preparative methods, a hard-templating method is promising for the precise control. In particular, the use of nanostructured silica as a template is beneficial due to its controllabilities of size, shape, morphology, and so on. However, there still remains a challenge for the precise control of nanostructured materials even by using the templating method.

Chapter 1 describes the general introduction of inorganic nanostructured materials. An overview of inorganic nanostructured materials is given in Section 1.2. The use of nanostructured silica as a template for the preparation of nanostructured materials is described in Section 1.3. In section 1.4, deposition methods which have been applied for the templating method are described. The significance and objective of this thesis are shown in section 1.5.

1.2 Inorganic nanostructured materials

1.2.1 Preparative methods of inorganic nanostructured materials

Preparative approaches of nanostructured materials may be classified into 1) top-down approach and 2) bottom-up approach.[1] In the top-down approach, nanostructured materials are prepared by breaking down bulk materials into nano-sized materials. In contrast, nanostructured materials are prepared by building up atoms and/or molecules into nano-sized materials in the bottom-up approach. It is generally known that the bottom-up approach is advantageous in the preparation of nanostructured materials with regard to variety and controllability of size, morphology, and composition, etc.[3]

Up to date, numerous nanostructured materials have been prepared *via* the bottom-up approach. Many kinds of chemical reactions, such as hydrothermal reaction and sol-gel reaction, have been applied for the preparation.[4] The chemical reactions applied for the preparation are summarized for each composition in Table 1.1

Table 1.1 Chemical reactions applied for the preparation of nanostructured materials.[4]

Compositions	Chemical reactions
Metals (e.g. Au, Pt, Pd, Ag, Cu, Ru)	Electrochemical reductions, electroless reductions, thermal reductions, etc.
Metal oxides (e.g. SiO_2, Al_2O_3, TiO_2, MnO_2, Fe_2O_3)	Sol-gel reactions, hydrothermal reactions, solvothermal reactions, thermal decompositions, etc.
Carbon	Carbonization of organic compounds, chemical vapor deposition, etc.
Others (e.g. SiC, Si_3N_4, BN, CdS, CdSe)	Thermal decompositions, coprecipitation reactions, etc.

In the bottom-up approach, controls of nucleation and growth processes are required to obtain nanostructured materials with targeted size, shape, crystallinity, etc.[2] Therefore, appropriate choices of chemical reaction and its conditions are essential. For the precise controls, the chemical reactions shown in Table 1.1 are typically performed under the presence of a capping agent[4a,4b,4d,5] and/or a template[4c,6]. Although nanostructured materials can be prepared without using a capping agent and a template by carefully setting the reaction conditions, poorly controlled nanostructures are normally formed.

The use of capping agents, such as organic molecules and polymers, are beneficial for the control of the growth process (Figure 1.1).

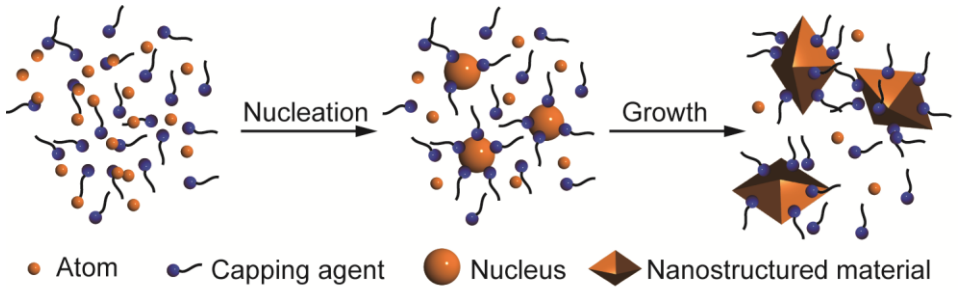

Figure 1.1 A schematic view of the preparation of nanostructured materials using capping agents.

The capping agents can inhibit overgrowth of formed nuclei during the growth process by passivating their surfaces.[4a,4b,4d,5] In addition, the capping agents can induce anisotropic crystal growth by passivating specific crystal planes, which enables the controls of shape and crystal facet of nanostructured materials.[4a,5e,5f,7] The passivation of the surfaces is also beneficial to prevent the formed nanostructured materials from the formation of their aggregates.[8] Because the effects of the capping agents described here deeply depend on many parameters (organic molecule/polymer used as a capping agent,

composition, crystal structure, and so on), an appropriate choice of the capping agents is required for the preparation of nanostructured materials with desired size, shape, crystallinity, etc. Although the preparative method using the capping agents is quite effective to control shape, crystallinity, crystal structure, and composition, the obtained nanostructured materials often suffer from residual capping agents on their surfaces.[8] This means that the surface properties are undesirably influenced by the residual capping agents.[8]

Another useful method to prepare nanostructured materials with controlled structures is a templating method using inorganic nanostructures, such as zeolite, mesoporous silica, and anodic aluminum oxide as a template (Figure 1.2).[4c,6]

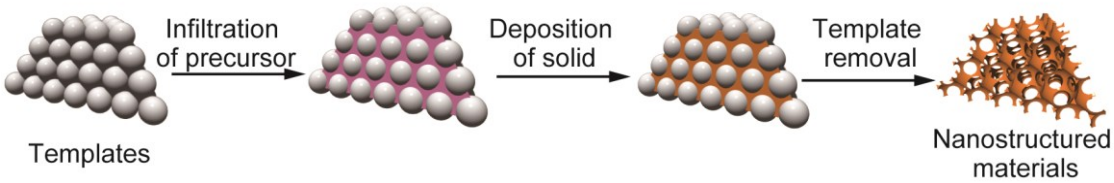

Figure 1.2 A schematic view of the preparation of nanostructured materials using the templating method.

In this method, nanostructured materials are typically obtained *via* the following three steps:[6e] 1) infiltration of a precursor inside spaces/pores of a template, 2) deposition of a targeted inorganic compound inside the spaces/pores, and 3) removal of the template. The growth of formed nuclei within the template is strongly inhibited by its rigid frameworks, resulting in the formation of nanostructured materials replicated from the template. Therefore, a precise design of the template is the first key step to prepare well-defined nanostructured materials. Among various inorganic nanostructures, nanostructured silica, such as zeolite, mesoporous silica and silica colloidal crystal, are especially useful as a template due to variableness and preciseness of their structural

controls. The usefulness of nanostructured silica as a template will be described in detail in section 1.3. Although the templating method is multi-step processes, this method holds well-defined nanostructured materials.[6a]

1.2.2 Features and applications of inorganic nanostructured materials[2,9]

Nanostructured materials exhibit unique properties which cannot be obtained from bulk materials because of their high surface to volume ratios and quantum confinement effects. Therefore, nanostructured materials have opened up new applications, and they have been actively studies so far.

One attractive feature of nanostructured materials is their high surface to volume ratios. Because surface atoms have fewer bonds with neighbor atoms, and accordingly larger unsaturated sites than interior atoms, the surface atoms are chemically more active. Furthermore, additional electronic states are formed by the presence of the unsaturated atoms, which work as electron or hole trap centers. The contribution of the surface nature to overall properties becomes significantly larger in nanostructured materials because of the high surface to volume ratios (Figure 1.3).

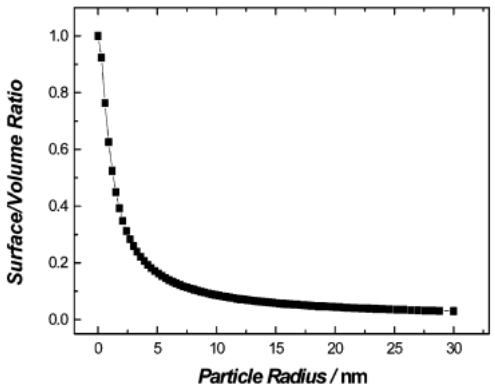

Figure 1.3 Surface to volume ratio as a function of a particle radius. Reprinted with permission from Ref. 2. Copyright 2005 American Chemical Society.

Therefore, nanostructured materials exhibit high catalytic activity,[5f] large storage ability,[5f,6f] unique optical property,[6b] and so on. In addition, physical properties, such as melting point and heat capacitance, are also varied if compared with those of bulk materials.

Another feature of nanostructured materials is quantum confinement effects which occur for metals and semiconductors. When the size of a compound is down to a nanometer range, its band structure is altered from continuous to discontinuous quantized band (Figure 1.4).[9] In the case of metals, their continuous density of states splits into discrete levels. In addition, spacings between energy levels in the bands increase with the decrease in size. Because of such a change of the band structures, when the size decreases to a few nanometers, metals often lose their metallic properties and exhibit semiconducting properties. In contrast to metals, semiconductors originally possess band gap energy between valence and conduction bands. The band gap energy becomes larger with decrease in the size. As a result, transitions of electrons/holes between valence and conduction bands in nanostructured materials are completely different from those in corresponding bulk counterparts.

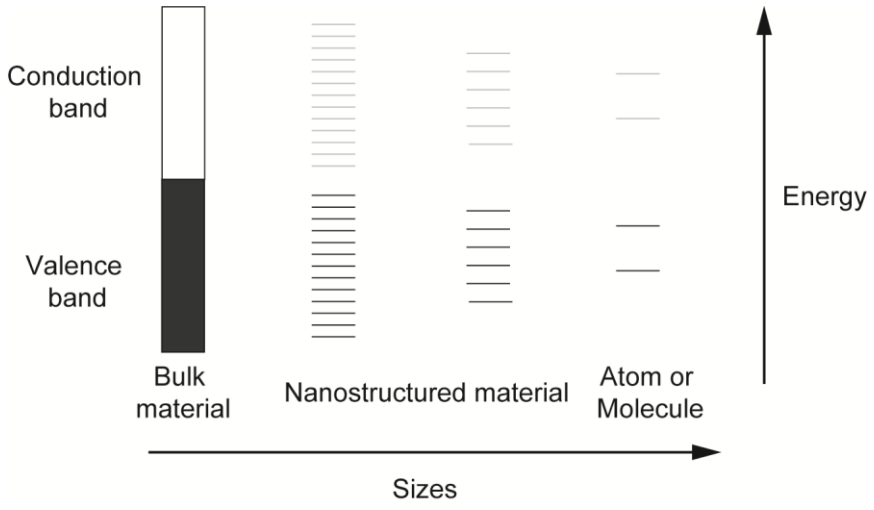

Figure 1.4 Band gap and the density states of nanostructured materials.

Because of both the high surface to volume ratios and the quantum confinement effects, nanostructured materials exhibit distinct properties (e.g. magnetic, optical, and electronic properties). Therefore, nanostructured materials have attracted much attention for various potential applications, such as catalysts, sensors, energy storage/conversion materials, electrodes, and adsorbents. Up to date, numerous studies have been reported on both the preparation and evaluation of their properties for such applications.

As one attractive application of nanostructured materials, thermoelectric materials have been intensively studied recently. The development of thermoelectric materials which can convert heat energy into electrical energy is one of promising solutions to improve the sustainability. The performance of thermoelectric conversion is generally evaluated by dimensionless thermoelectric figure of merit (ZT). ZT is given in the following equation: $ZT = S^2 \sigma T / \kappa$, where S, σ, T, and κ are the Seebeck coefficient, electrical conductivity, temperature, and thermal conductivity, respectively.

The change of band structure by the size reduction to a nanometer range has been theoretically predicted to have a good influence on the increase in both Seebeck coefficient and electrical conductivity.[10] And more, the high surface area of nanostructured materials increases interfacial phonon scattering effectively, resulting in lower thermal conductivity.[10] For these reasons, the use of nanostructured materials is promising for the thermoelectric application. Although enhancements in ZT value by using nanostructured materials if compared with bulk counterparts were recently shown experimentally,[11] the enhancements in most reports are mainly due to significant reduction in thermal conductivity.[12] The increase in Seebeck coefficient and electrical conductivity due to the change in band structure has not been fully understood

experimentally. Therefore, further studies are highly demanded toward the use of nanostructured materials for the thermoelectric application.

1.2.3 Summary

Up to date, numerous studies have been reported on the preparation and applications of nanostructured materials. Nanostructured materials in the most reports are prepared *via* the bottom-up process using various chemical reactions as shown in Table 1.1. In order to prepare well-defined nanostructured materials, the use of capping agent and/or template is quite effective. In addition, nanostructured materials exhibit unique properties because of the high surface to volume ratios and the quantum confinement effects. Therefore, various applications are expected.

1.3 Silica templates used for preparation of inorganic nanostructured materials

As described briefly in section 1.2, a templating method using nanostructured silica, such as zeolite, mesoporous silica, and silica colloidal crystal, as a template is a powerful route to prepare well-defined nanostructured materials. The nanostructured silica possess uniform and controllable pore/space size and shape, meaning that nanostructured materials with uniform and controlled size and shape can be obtained by using the nanostructured silica as a template. For the preparation of nanostructured materials with desired size and shape, an appropriate choice of a template is the first key step. In section 1.3, the use of nanostructured silica as a template for the preparation of inorganic nanostructured materials is reviewed. Because the templating method is frequently applied to the preparation of nanostructured metals, metal oxides, and carbon materials, some key points to be noted and examples of the preparation are described for

the compositions.

1.3.1 Zeolite template

A term of "zeolite" generally indicates crystalline aluminosilicate or silica whose frameworks are composed of TO_4 (T = Si and Al) tetrahedra with uniform and orderly arranged micropores (pore sizes of micropores are defined as less than 2 nm by IUPAC). In addition, zeolites typically possess exchangeable cations within the micropores. The ion-exchange ability of zeolites is used to incorporate a precursor of nanostructured materials when zeolites are used as a template.[13] The size and shape of the micropores of zeolite are mainly dependent on its crystal structures. According to pore arrangement, pore shape, and pore size, there are more than 200 different zeolite structure types currently.[14] These variations are useful as a template to control the size and shape of nanostructured materials.

Although there have been some reports on mesoporous zeolites,[15] the pore size of zeolites are typically less than 2 nm. Therefore, when zeolites are used as a template, clusters (whose sizes are smaller than nanoparticles) are typically formed within the micropores.[16] The clusters formed in zeolites can be present stably because framework oxygen atoms and/or extra-framework cation atoms can stabilize the clusters.[16] Therefore, the formed clusters are used without removing the template. In contrast, three-dimensionally continuous frameworks can be formed for carbon within zeolites. In this case, the formed nanostructured carbon is stable even without the template, and therefore, used after the template removal.[6f]

The use of zeolites as a template enables not only the preparation of nanostructured materials but also control of their arrangements due to the

three-dimensionally ordered arrangement of micropores. The arrangement of the formed nanostructured materials often affects their properties. Because the frameworks of zeolites are thin, the formed clusters can interact with adjacent clusters. In this case, the clusters exhibit unique properties which are different with those of isolated clusters.

Metals

Metal clusters are most common nanostructured materials prepared by using zeolites as a template. There are two major deposition methods of metals within the micropores of the template. One is a direct metal deposition using metal vapor, and the other is a decomposition or reduction of a metal precursor incorporated into the micropores.

The first study to reveal the formation of metal clusters was reported by Kasai in 1965.[17] In this report, Na_4^{3+} clusters were formed in Na-Y zeolite by gamma ray irradiation under a reduced pressure condition. He revealed the formation of the clusters by ESR splitting. A study on the preparation of transition metal clusters was reported in 1977.[18] Ag_6^0 clusters were prepared by partial decomposition of Ag^+ within zeolite A. The Ag clusters formed in zeolite A were sensitive to guest molecules, and their color was varied by adsorption of the guest molecules on their surfaces.[16b] Therefore, the Ag clusters in zeolite A are promising as a high sensitive sensor.

In addition to Na and Ag, K,[19] Fe,[20] Ni,[21] Ru,[22] Rh,[23] Pd,[24] Ir,[25] and Pt[26] clusters have been also prepared by using zeolites as a template. The transition metal clusters work as catalytic sites. Because zeolites also have catalytic activities, the metal clusters/zeolites nanocomposites are useful as bifunctional catalysts. In contrast, K clusters incorporated into micropores of zeolites exhibited ferromagnetic property,

although K metal does not show the property.[19b]

Metal oxides

Metal oxide clusters can be prepared mainly by calcination of a precursor incorporated zeolites. Up to date, La oxide,[27] Zn oxide,[28] Mo oxide,[29] Fe oxide,[30] Cu oxide,[31] and Re-Mo oxide[32] clusters have been prepared by using zeolites as a template. These oxide clusters are useful as catalysts with high thermal stability. The high thermal stability is explained by the formation of M-O-Si (M: metal) bonds between the metal oxide clusters and frameworks of zeolites.

Carbon

The use of zeolites for preparation of nanoporous carbon has been studied since the late 1990s.[33] The nanoporous carbon can be prepared by carbonization after incorporation of an organic compound as a carbon source into the micropores of zeolite templates. After removal of the templates, the nanoporous carbon can be stably obtained because of its three-dimensional networks of frameworks (Figure 1.5). This is contrast to metal and metal oxide clusters which cannot retain the formed nanostructures without the zeolite templates. The nanoporous carbon prepared by using the zeolite templates was not perfect replications of the templates in most of the reports, meaning that the pore size and pore shape of the obtained nanoporous carbon were not uniform.[6f] However, some groups succeeded in the preparation of nanoporous carbon perfectly replicated from the templates.[34] The nanoporous carbon prepared by using zeolite templates offer high surface areas, large pore volume, fast mass transfers.[6f]

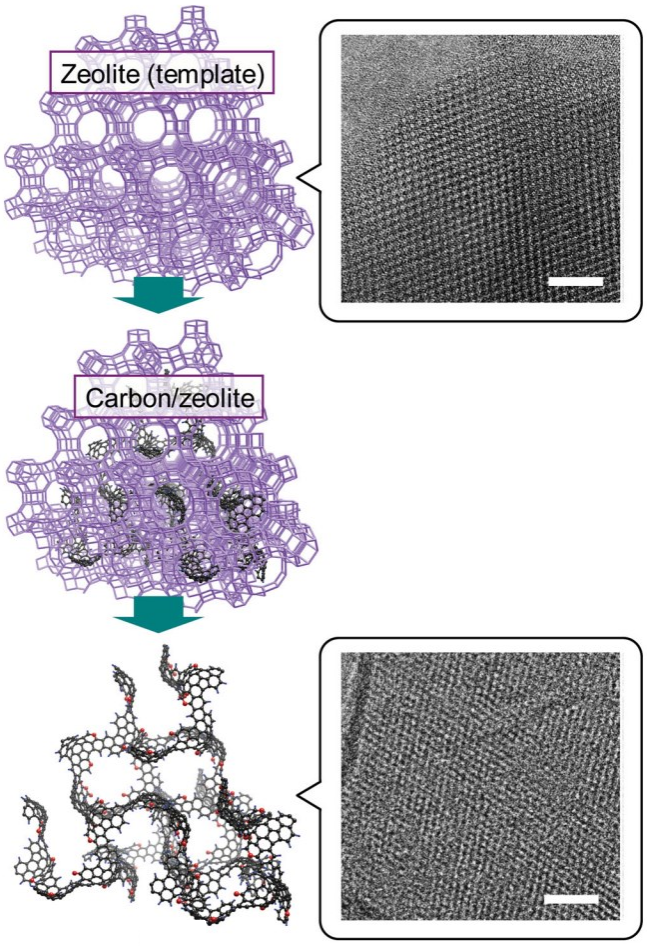

Figure 1.5 A scheme for preparation of nanoporous carbon using zeolites as a template and the TEM images of the template and the nanoporous carbon in the previous report. Scale bars in the TEM images are 10 nm. Reprinted with permission from Ref. 6f. Copyright 2012 John Wiley & Sons, Inc.

1.3.2 Mesoporous silica template

Since the discovery mesoporous silica in the early 1990s,[35] numerous studies have been reported on both its preparation and application.[36] Mesoporous silica has uniform mesopores (pore size of mesopores is defined as between 2 nm to 50 nm by IUPAC) and their ordered arrangement. The pore size can be precisely controlled in a range between *ca.* 2 nm to a few tens of nanometers by using different surfactants, adding pore expanders, and varying aging temperature.[37] The pore shape (cylindrical,

spherical, and their combination) and the pore geometry (some examples are shown in Figure 1.6) can also be controlled variously by appropriately setting the preparative conditions.[36a] In addition, morphology of mesoporous silica (film, powder, and monolith) can be easily controlled.[36a] Because of these controllabilities, mesoporous silica has been used as a template for the preparation of nanostructured materials with different compositions. [4c,6d,38]

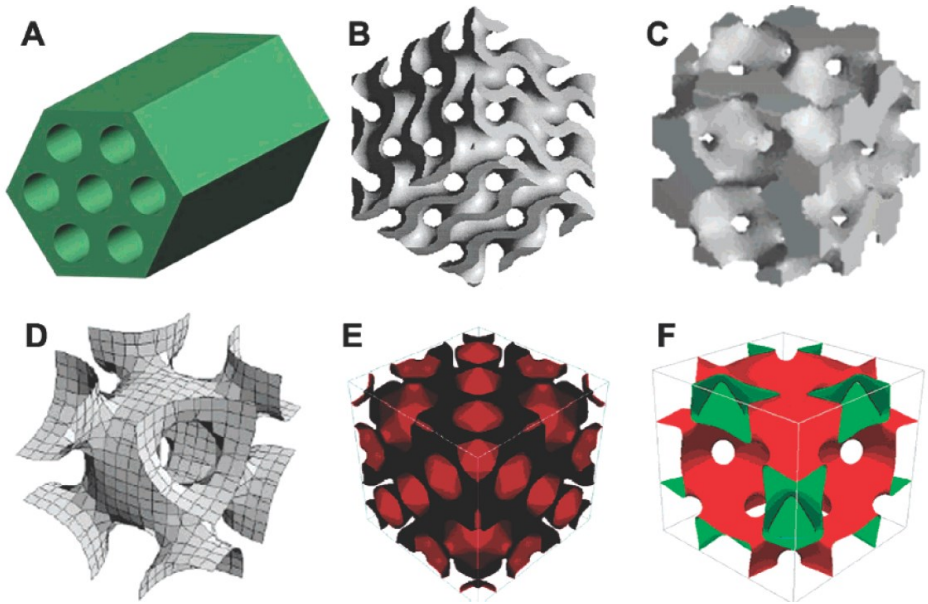

Figure 1.6 Pore models of mesoporous structures with different pore geometries; (A) *p6mm*, (B) $Ia\bar{3}d$, (C) $Pm\bar{3}n$, (D) $Im\bar{3}m$, (E) $Fd\bar{3}m$, and (F) $Fm\bar{3}m$. Reprinted with permission from Ref. 36a. Copyright 2007 American Chemical Society.

The pioneering works on the use of mesoporous silica as a template were reported by R. Ryoo and his coworkers. Mesoporous carbon (CMK-1[39] and CMK-3[40]) were prepared by using mesoporous silica MCM-48 and SBA-15 as templates, respectively. The obtained mesoporous carbon exhibited uniform pore sizes and extremely high surface areas.[39-40] In addition, a fact that the obtained mesoporous carbon CMK-3 possessed an ordered mesostructure, which was same as the original

template, is remarkable. This result was a strong evidence that SBA-15 possessed connecting pores between primary mesochannels, which was different from MCM-41 with the similar 2D mesostructures.[40] Owing to the connecting pores, carbon nanorods replicated from the pore shape of the template were bridged with each other, resulting in the formation of the ordered arrangement of the rods. This report is valuable to show the usefulness of the templating method for not only preparation of novel nanostructured materials but also characterization of mesostructures of mesoporous silica.

As mentioned in the beginning of this section, the templating method consists of the three steps (1) infiltration of a precursor, 2) deposition of a targeted compound, 3) template removal). Because the pore sizes of mesoporous silica are much larger than those of zeolites, the introduction of a precursor is not so difficult. In general, solvent evaporation method, two-solvent method, solid-liquid method, and impregnation method are used for the introduction.[38a] An appropriate method should be chosen to obtain desired nanostructures because the introduction methods sometimes affect the formed nanostructures.[41] The deposition process is the most important step for the successful preparation and the control of the nanostructures of the replicas. The details of the deposition process will be described in section 1.4. The template removal is performed by using aq. HF or basic aqueous solution such as aq. NaOH. In order to avoid structural collapse of nanostructured materials during the template removal, the reactivity between an etching solution and the formed nanostructured materials must be considered. In addition, surface states of the obtained nanostructured materials after the template removal should also be considered, although they are not characterized in most of the previous reports. When aq. NaOH is used for the template removal, Si species often remain on the surfaces of the obtained replicas owing to the formation of Si-O-M

(M: metal) bonds.[42]

The connecting pores between primary mesopores as mentioned above are one of characters of mesoporous silica.[36a] The connecting pores are often co-formed along with primary mesopores when mesoporous silica is prepared by using block copolymers including a poly(ethylene oxide) chain as a surfactant. When mesoporous silica having such the connecting pores is used as a template, the nanostructures of replicas differ by the conditions whether solid is deposited within the connecting pores or not (Figure 1.7).[38a] For example, nanorods/wires replicated from the pore shape of SBA-15 are obtained without deposition within the connecting pores. In contrast, mesoporous materials are obtained when solid is deposited within the connecting pores along with the primary mesochannels. Therefore, the controlled deposition is essential to obtain desired structure. However, there still remains a challenge in such a controlled deposition. The deposition behavior depends on composition, the amount of deposited compound, and deposition method.

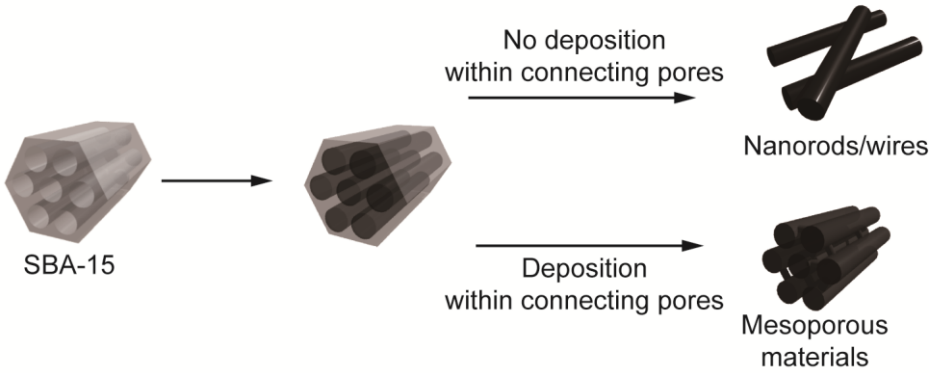

Figure 1.7 A schematic view of the templating method using SBA-15 as a template.

In addition, modifiable silanol groups located on the surfaces with organic molecules are also characteristics of mesoporous silica.[43] Interactions between guest

species and mesoporous silica can be varied by the surface organic modificatons.[44] The surface modifications with functional groups which strongly interact with the precursors facilitate their introduction into the mesopores.[44] The strong interaction also has a good influence for inside deposition by suppressing migration of guest species. The surface modifications are often used for Au depositions as described below.

Metals

Nanostructured metals are prepared by reducing metal cations within the mesopores. The reduction of metal cations is typically performed by chemical reduction, thermal reduction under H_2 gas flow, or electrochemical reduction.[38c,38d] Metals tend to deposit outside the template and form bulk particles because of their high surface energy. In addition, morphology and crystallinity of deposited metals strongly depend on various parameters (precursors, pore size of the template, reduction conditions, etc.). Therefore, judicious choices of the parameters are essential for the successful preparation.

Up to date, the preparation of nanostructured metals using mesoporous silica template have been achieved in various metals (Co,[45] Ni,[46] Cu,[45] Ru,[47] Pd,[48] Ag,[49] Pt,[48-49] and Au[48-49]). In addition to the monometallic materials, nanostructured bimetallic materials have been prepared.[50] The bimetallic materials often exhibit superior catalytic activity to the monometallic materials owing to synergistic effects of two kind of metals.[50]

The surface organic modifications with amine, thiol, or ammonium groups are typically required for Au deposition mainly because of weak interaction between Au species and the surfaces of the template (Figure 1.8).[48,51] In contrast, the inside

deposition of most of the metals except Au within the template are easily achieved without such surface modifications.

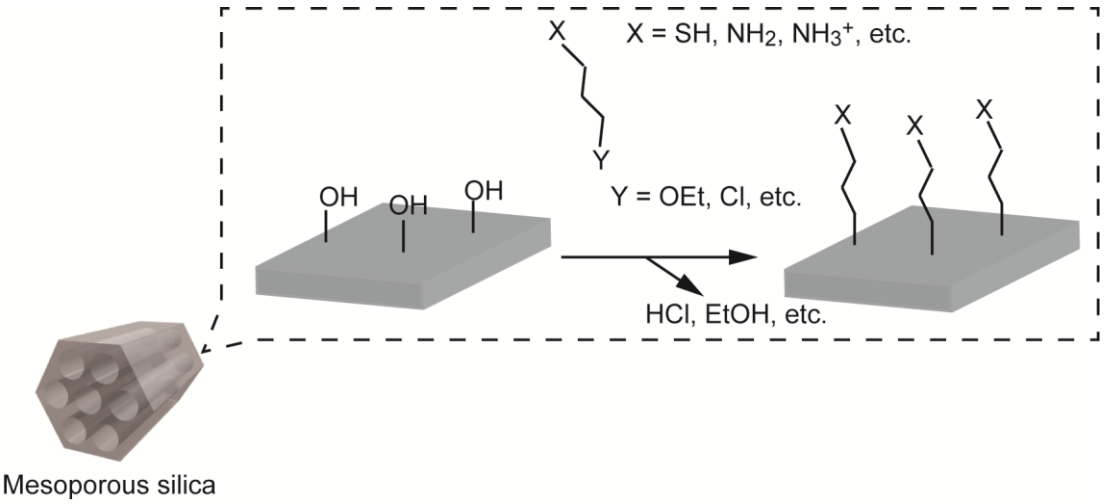

Figure 1.8 A schematic view of surface organic modifications of the surface of mesoporous silica.

Conventional nanostructures, such as nanoparticles and nanorods/wires, tend to form aggregates, resulting in low effective use of their surfaces. In contrast, mesoporous metals, which are one of the nanostructures prepared by using mesoporous silica template, have been good candidates to overcome the drawback of the conventional nanostructured metals owing to their high inner surface area and accessibility of guest species. In addition, the continuous frameworks are advantageous for better electrical conductivity.

Metal oxides

In most of the previous reports, metal oxides are deposited within the template by thermal decomposition after the infiltration of a precursor.[38a] The inside deposition is not so difficult for metal oxides as compared with metals. This would be explained by

the formation of Si-O-M (M: metal) bonds between the template and metal oxide replicas during the thermal decomposition. It should be noted that the templating method using mesoporous silica cannot be applied to some compositions, such as Al_2O_3 and ZnO, because of their reactivities with both HF aq. and base solutions. In this case, other template such as mesoporous carbon should be used instead of mesoporous silica.[52]

In the case of metal oxides, crystallized frameworks are required to obtain desired properties.[38a] In general, high temperature calcination is required to achieve fully crystallized and/or single crystalline frameworks. However, high temperature calcination often results in structural collapse of the template by crystallization of the amorphous silica frameworks and/or formation of metal silicates by reaction between the silica template and metal oxide replicas. These are drawbacks of mesoporous silica template for the preparation of nanostructured metal oxides. In order to overcome these drawbacks, effective crystallization methods at low temperature are demanded. The use of metal nitrates as a metal precursor has been reported to be effective to obtain crystallized frameworks by low temperature calcination, which is explained by low decomposition temperature of metal nitrates.[53] However, in the previous reports, the characterization on the crystallinity is not enough.

Carbon

The preparation of nanostructured carbon (in most cases, mesoporous carbon materials were prepared) has been most common and developed in the templating method using mesoporous silica. Various mesoporous carbon materials with different pore size, pore geometry, or wall thickness have been prepared.[4c,38b]

The properties of mesoporous carbon are dependent on mesostructures (pore size, wall thickness, pore geometry, etc.) and graphitization degree of frameworks. Therefore, the control of both the mesostructure and the graphitization degree has been studied. The former was easily achieved by varying the mesostructure of the template. The high graphitization degree, which is desired for capacitors and electrodes because of higher electronic conductivity, was achieved by using aromatic compounds as a carbon source[54] and adding catalysts to promote the graphitization of the frameworks.[55]

In the conventional preparation, the mesopores of the template are completely filled with carbon. In contrast, R. Ryoo et al. reported that the partial filling of the mesopores of SBA-15 resulted in the formation of mesoporous carbon with tubular frameworks (named CMK-5, Figure 1.9).[56] Because of the tubular structures, both inner and outer surface can be used, resulting in the higher surface area than conventional mesoporous carbon.[56]

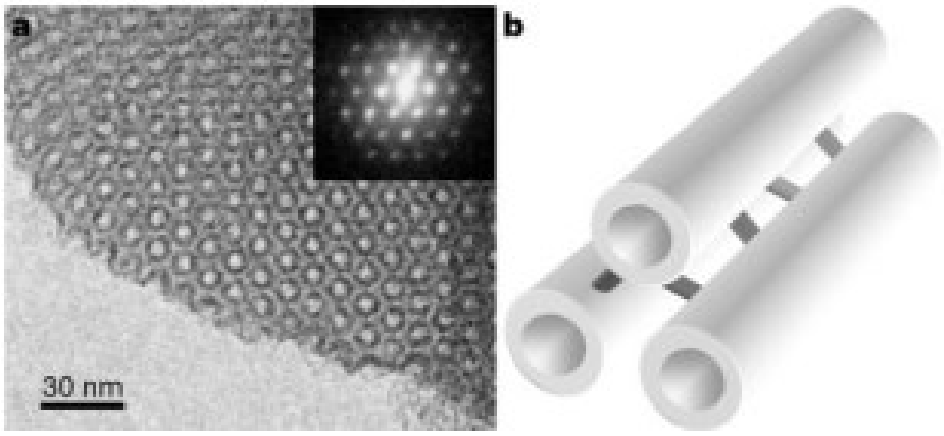

Figure 1.9 (a) The TEM image and (b) a schematic model of CMK-5. Reprinted with permission from Ref. 56. Copyright 2001 Nature Publishing Group.

The use of mesoporous carbon as a host material to incorporate metal oxide nanoparticles has been one of the most promising applications. Mesoporous carbon can provide high surface area, mechanical stability and electrical conductivity to metal

oxides nanoparticles. Therefore, these nanocomposites are potentially applicable as catalysts, capacitors, electrodes, and so on.[57] Although a lot of studies have been reported on the preparation of nanocomposites, the preparative method has not been so developed.[57a] Metal oxide nanoparticles are conventionally prepared within the mesopores by thermal decomposition after the incorporation of a metal oxide precursor into the mesopores. However, the method suffers from low controllabilities of the loading amount and the size of metal oxide nanoparticles formed within mesoporous carbon.

1.3.3 Silica colloidal crystal template

Silica colloidal crystals are close-packed arrays (typically face-centered-cubic (fcc) lattice) of monodisperse silica nanospheres (Figure 1.10A). Therefore, by using silica colloidal crystals as a template, three-dimensional ordered macro/mesoporous (3DOM/m) materials can be obtained (Figure 1.10B).[6e] Although the controllability of pore shape and geometry using silica colloidal crystal templates is low, pore size of 3DOM/m materials can be controlled in a wide range between *ca.* 10 nm to 1 μm because particles size of silica nanospheres can be controlled in this range.[58] This wide range controllability of pore size is one of the advantage points of the colloidal crystal template if compared with those of zeolite and mesoporous silica templates.

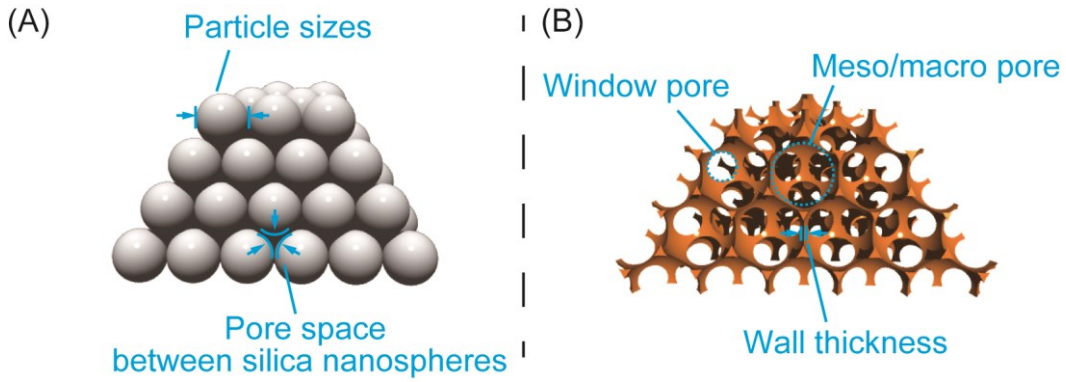

Figure 1.10 Diagrams of (A) silica colloidal crystals and (B) 3DOM/m materials.

Considering the fcc arrangement of silica nanospheres, 3DOM/m materials should consists of 74% pore space. In addition, each pore of 3DOM/m materials connects with twelve neighboring pores through window pores (Figure 1.10B). Owing to these characteristics of 3DOM/m materials, the mass transport through 3DOM/m materials is more effective than other porous materials. Therefore, 3DOM/m materials should have better kinetic properties in various applications, such catalysts, sensors, electrodes, etc.

The control of wall thickness of 3DOM/m materials is also required for tuning their properties.[6e,59] The spaces between silica nanospheres, where the frameworks of 3DOM/m materials are formed, are defined by the sphere size. Therefore, it is difficult to control both the pore size and wall thickness of 3DOM/m materials independently. Although thinner wall thickness than expected from the pore space of the template can be achieved by inducing large shrinkage of frameworks, the precise and uniform control are normally difficult. When the wall thickness is thick, additional meso/micropores can be incorporated into the frameworks.[6e] These hierarchical porous structures can be prepared by adding surfactants or small nanoparticles along with a precursor into the pore spaces of the template.[6e] The formation of hierarchical structures has good

influence on the mass transport properties.

The key points to be considered and the applicability of compositions in the templated preparation using silica colloidal crystals are almost same as those using mesoporous silica. Therefore, some examples which are unique to the use of silica colloidal crystal templates are shown below.

Metals

As described above, 3DOM/m materials are obtained when silica colloidal crystals are used as a template. Meanwhile, Y. Kuroda and K. Kuroda reported the formation of plate-like nanostructured Au with ordered mesoscale dimples on the both sides using silica colloidal crystals composed of silica nanospheres with 40 nm in diameter as a template (Figure 1.11).[60] Crystal growth of Au in the interstices of the template induced the cleavage of the template, and the unique structure was formed by replication of the cleaved surface. One of the key points of the formation was the low density of Si-O-Si bonds between the constituent silica nanospheres. Because of this, the cleavage was caused by the crystal growth of Au.

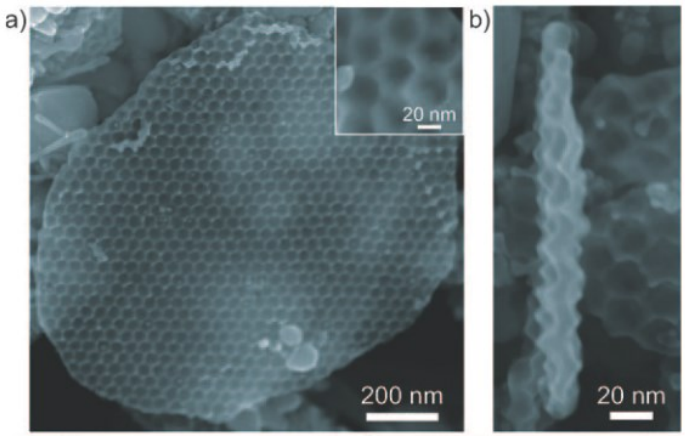

Figure 1.11 (a) The surface and (b) cross section SEM images of the plate-like nanostructured Au. Reprinted with permission from Ref. 60. Copyright 2010 John Wiley & Sons, Inc.

Metal oxides

The formation of single crystalline metal oxide frameworks is one of the vital goals to be achieved in the templated preparation of nanostructured metal oxides. Recently, preparation of mesoporous TiO_2 with single crystalline frameworks was reported, although its pore arrangement was not ordered.[61] The preparative method is a sort of seed-growth process. A small amount of TiO_2 was deposited within the assembly of silica nanospheres prior to hydrothermal deposition of TiO_2. The pre-deposited TiO_2 within the template worked as a nucleus to prevent the outer deposition of TiO_2. In addition, the reaction conditions of the hydrothermal treatment were suitable to form single crystalline TiO_2 frameworks.[62]

Carbon

3DOM/m carbon materials are used for various applications, such as capacitors, electrodes, sensors, etc. because of their high surface area and mass transport properties. One unique application of 3DOM carbon is a template for preparation of spherical shaped zeolite particles with uniform size.[63] 3DOM carbon provided a reaction field for the formation of zeolite by the hydrothermal treatment. The relatively large pore space of 3DOM carbon would be more suitable for the formation of zeolites than mesoporous carbon such as CMK-3.

1.3.4 Summary

Various nanostructured materials have been prepared by using nanostructured silica, such as zeolites, mesoporous silica, and silica colloidal crystals, as a template. The nanostructured silica is advantageous as a template from the viewpoint of

controllability of size, structures, and morphology.

Zeolite template is used mainly for the preparation of metal clusters and nanoporous carbon. Because the formed clusters are prevented from further growth and formation of aggregates by the frameworks of zeolite, the nearly bare surface of the clusters can be used under the presence of zeolite template. The frameworks of nanoporous carbon prepared by using zeolite template are thin due to the micropores of the template, resulting in extremely high surface area.

Because the pore size of mesoporous silica is much larger than that of zeolite, the size of the frameworks of the formed nanostructures is also larger. Therefore, the formed nanostructures can retain their nanostructures even after removal of the templates. Owing to the variabilities of pore shapes, sizes and geometry of mesoporous silica, various nanostructured materials can be prepared.

3DOM/m materials with fcc arranged uniform pores can be obtained when silica colloidal crystals are used as a template. The controllable range of pore size of 3DOM/m materials is much wider than that of other porous materials prepared by using zeolite and mesoporous silica templates because the particle size of silica nanospheres can be controlled in a range between *ca.* 10 nm to 1 μm. 3DOM/m materials exhibit superior mass transport properties to other porous materials because each pore of 3DOM/m materials connects with twelve neighboring pores.

1.4 Deposition methods applied for the templating method

In the templating method, deposition process is most influential to nanostructures of replicas. For instance, crystallite size of nanostructured materials formed within templates depends on not only size of spaces/pores of the templates but

also deposition methods. Therefore, an appropriate deposition method should be applied to obtain desired nanostructured materials. The most typical templates described in this section are the silica templates such as zeolites, mesoporous silica and silica colloidal crystals.

For the successful preparation of nanostructured materials replicated from the templates, an inorganic compound must be deposited within the templates. This prerequisite for the successful preparation limits deposition methods applicable to the templating method. In this section, deposition methods which have been applied for the templating method are overviewed for each composition.

1.4.1 Deposition methods of metals

In the templated preparation of nanostructured metals, metals are deposited by reducing corresponding metal cations. Metal species tend to migrate from inside to outside the templates during the reduction to form larger particles in order to minimize their surface energy. Therefore, the migration of metal species needs to be suppressed. The suppression is generally achieved by surface organic modification of the templates with thiol, amine, or ammonium groups because of the strong interaction between the metal species and the functional groups. In addition, reducing agents (electron donors) are also required to be effectively introduced into the templates.

The reduction rate of a metal precursor is a decisive factor on the crystallite size and particle shape of formed nanostructures. When the reduction rate is relatively fast, a lot of nuclei are formed, resulting in the formation of metal nanoparticles or metal replicas with small crystallite size. In contrast, metal replicas with large crystallite size are formed when the reduction rate is relatively slow. Therefore, a deposition

method which can control the reduction rate is suitable.

Thermal reduction under H_2 gas flow

Thermal reduction under H_2 gas flow is used for the deposition of metals whose redox potential is higher than that of H_2. The reaction is typically performed at 373 K –573 K under a mixed gas flow of H_2 and Ar/N_2. Because of its small molecule size, H_2 can access even into the micropores of zeolites.[20-21] Therefore, the deposition method can be applied for zeolites, mesoporous silica, and silica colloidal crystal templates. In addition, the method is applicable to various morphologies, such as powder, film, and monolith.

The increase rate of the temperature sometimes affects the nanostructures of replicas. R. Ryoo et al. reported the preparation of nanostructured Pt using MCM-48 as a template.[64] In the report, continuous Pt frameworks replicated from the template were formed when the increase rate of the temperature was relatively slow. In contrast, discrete Pt nanoparticles with 3 nm – 5 nm were formed when the increase rate was relatively fast. This difference should be caused by the different reduction rates due to the varied increase rates.

In general, the thermal deposition is performed after incorporation of a metal precursor into the templates. In contrast, some studies reported the preparation of 3DOM/m metals *via* the thermal reduction of the corresponding 3DOM metal oxides.[65] During the reduction from metal oxides to corresponding metals, the frameworks of 3DOM materials shrank more than 30%. Therefore, the periodicity of 3DOM metals prepared by this process is lower than that prepared from metal precursors. Furthermore, this process is not suitable for mesoporous metals because their frameworks are too thin

to retain the porous structures after the shrinkage.

Electrodeposition

An electrodeposition is a powerful method for the metal deposition because the reduction rate can be easily controlled by varying an applied voltage, although the method can be applied only to nanostructured silica films on conductive substrates. The reduction of metal cations occurs on surfaces of the substrates, meaning that metal atoms are formed on the surface of the substrates. This leads to the formation of nuclei, and subsequently continuous networks of metals on the surfaces. Therefore, outer depositions of metals can be easily avoided, and nanostructured metals replicated from the templates are obtained.

Because the reduction occurs on the surfaces of the substrates, nanostructures of the templates near the surfaces are vital for the successful deposition within the templates as demonstrated by Kanno et al.[66] In the report, Au was electrochemically deposited within a mesoporous silica film with 2D hexagonally arranged mesochannels on an ITO substrate. When all mesochannels lie parallel to a substrate, the film was cleaved by deposited Au. In contrast, when a film possess mesochannels aligned vertically to the substrate in addition to the mesochannels lying parallel to the substrate, Au was successfully deposited within the mesochannels without the cleavage of the film to form Au nanowires replicated from the template.

As mentioned above, the control of the reduction rate is facile in the electrodeposition method. U.-H. Lee et al.[67] reported the formation of single crystalline Pt nanowires by electrochemical deposition of Pt within mesoporous silica template. Although there is no detailed description on the formation of single crystalline Pt

frameworks, the use of electrodeposition method would be critical. In the electrodeposition method, because electrons are supplied through predeposited metals, metal precursors tend to be reduced on the surfaces of the predeposited metals. In addition, the formation of new nuclei during crystal growth of metals can be avoided by carefully tuning the applied voltage. Due to these natures of electrochemical deposition process, the formation of single crystalline frameworks was achieved.

Electroless chemical deposition

Electroless chemical deposition using chemical compounds as a reducing agent is also a powerful method due to variability of reducing agents which enables the control of the reduction rates. Although the controllability of the reduction rates of the chemical deposition method would be lower than that of electrodeposition method, the method can be applied to not only films but also powder and monolith. Solvents are not used for the metal deposition under the presence of the templates because metal precursors incorporated into the templates tend to flow to outside the templates by the dissolution in the solvents.

A typical procedure of the chemical deposition is performed by dropping a small amount of an aqueous solution of reducing agent, such as sodium tetrahydroborate on the metal precursor incorporated templates. The amount of the aqueous solution should be small because water elutes the metal precursors outside the templates and enhances the migration of metal species during the reduction. H. Wang et al. have demonstrated that the use of ascorbic acid as a reducing agent enables both size- and shape-controlled preparation of mesoporous Pt using KIT-6 as a template. The obtained mesoporous Pt possesses single crystalline frameworks and a polyhedral particle shape.

High redox potential of ascorbic acid is critical for the formation of the single crystalline frameworks. Due to the high redox potential, the reduction rate of Pt precursors and supply rate of Pt atoms were slow. Therefore, Pt nuclei were formed within the templates and crystal growth of Pt proceeded from the formed nuclei without formation of new nuclei, resulting in the formation of single crystalline Pt with polyhedral particle shape. In contrast to ascorbic acid, the use of sodium borohydride and dimethylamine borane (DMAB), whose redox potentials are much higher than that of ascorbic acid, resulted in the formation of mesoporous Pt with undefined particles shapes. As shown in this report, the choice of the reducing agent largely affects nanostructures of the replicas.

The use of vapor of DMAB as a reducing agent is also valuable for the metal deposition. Noble metal (Pt, Ag, and Au) nanowires were successfully prepared by using SBA-15 as a template through the vapor infiltration of DMAB. Because the method does not require any solvents, the elution of metal precursors to outer surfaces due to dissolution of metal precursors can be avoided. In addition, the choice of DMAB is smart because the metal deposition can procced under its mild condition near room temperature thanks to the volatile nature of DMAB around room temperature.

A phase of reducing agent should be taken into consideration for the metal deposition even if same reducing agent is used. When Au was deposited with vapor of DMAB within silica colloidal crystal template, 2D plate-like nanostructured Au with dimpled surface was formed as already shown in Figure 1.11.[60] In contrast, when Au deposition was performed by mixing a solid of DMAB and the Au precursor incorporated template, 3DOm Au replicated from the template was obtained.[60] This difference was mainly due to the different reduction rates. The reduction rate of vapor

phase infiltration of DMAB was slower than that of the solid phase reduction. The slow reduction rate enabled continuous crystal growth of Au within the template, which caused strain in the template. This resulted in the cleavage of the template and the formation of the dimpled nanostructure.

UV reduction

The reduction of metal precursors using UV irradiation typically requires organic compounds as an electron donor. By UV irradiation, the organic compounds incorporated into the template are decomposed and consequently release electrons to reduce metal precursors. In fact, a previous report on preparation Pt nanowires using mesoporous silica template has demonstrated that the reduction of Pt precursor did not occur under the absence of methanol.[68] The reduction rate of UV reduction is slow and the reduction can be stopped easily by turning off the UV irradiation, which is promising for size-controlled preparation of nanostructured materials.

Vapor phase deposition method

Vapor phase deposition methods, such as chemical vapor deposition (CVD), are one of physical processes which can be applied for the templating method. Vapor of metals are infiltrated into templates, and metal frameworks are formed. In this method, because metal atoms are directly deposited without the reduction process, the method can be applied for metals with low redox potential. For example, because of the low redox potential of Si and its high affinity with oxygen, it is hard to apply the reduction processes described above to Si deposition within the template. In contrast, the use of vapor deposition method was demonstrated to enable the Si deposition within silica

colloidal crystal template and accordingly preparation of 3DOM Si.[69]

An unique example on the use of vapor deposition of metals for the templating method is reported by M. Kobayashi et al.[70] Cu was deposited on surface of mesoporous silica film by using Cu vapor. Because the vapor falls from above the film, Cu was deposited only near the surface. Therefore, the deposited Cu form nanostructure replicate from only the surface of the film.

1.4.2 Deposition methods of metal oxides

As described in section 1.3, the formation of crystalline frameworks of metal oxides is highly required to obtain desired properties. Therefore, strategies to obtain the crystalline frameworks are crucial in the templated preparation of nanostructured metal oxides. Although sol-gel reaction and layer-by-layer deposition are widely applied for the formation of metal oxide frameworks, the obtained frameworks are typically amorphous. Therefore, thermal treatment at elevated temperature is required to obtain crystalline frameworks. In the following, the deposition methods to obtain crystalline frameworks are directly described.

Thermal decomposition

Thermal decomposition of metal oxide precursors incorporated into the templates is most widely used for the preparation of nanostructured metal oxides with crystalline frameworks.[38a] Metal nitrate, metal chlorides, and metal alkoxides are generally used as a metal oxide precursor. The temperature of heat treatment needs to be decided by considering the decomposition temperatures of the precursors and the crystallization temperature of metal oxide frameworks. However, the decomposition and

crystallization temperatures are often slightly different between under the presence and absence of the templates. The crystallization temperature within the templates is typically higher than that under the absence of the template mainly because of the confined nanospaces and the surrounding silica frameworks.[71] In addition, higher temperature than the crystallization temperature is often required to obtain fully crystallized frameworks.

Although heat treatment at higher temperature is preferable to crystallize metal oxide frameworks, the nanostructures of the templates and corresponding replicas are collapsed by heat treatment at such high temperature. This is because the crystallization of silica frameworks of the templates induces the collapse. The crystallization occurs at higher than *ca.* 900 °C. In addition, some metal species formed metal silicates with the silica templates during the heat treatment. Therefore, appropriate temperature should be investigated for each composition.

In order to achieve full crystallization at lower temperatures, the use of metal nitrates as a metal precursor has been reported to be beneficial due to low decomposition temperature of metal nitrates.[53] However, the crystallinity of the metal oxide frameworks in the previous report was not characterized sufficiently.

Hydrothermal deposition

Hydrothermal deposition of metal oxides is a great candidate to obtain crystalline metal oxides because the reaction proceeds at much lower temperature. In addition, the control of shape and crystallite size of metal oxides is achieved by varying the reaction conditions and/or adding capping agents.[72] However, hydrothermal deposition is not suitable for inside deposition within the templates because metal oxide

precursors incorporated into the templates tend to flow to outside the templates due to the dissolution of the precursors in water. In addition, there is no strong driving force to form nuclei and grow crystals exclusively within the templates in such hydrothermal processes. If hydrothermal deposition, which enables the control of shapes and crystallite size of metal oxides, can be applied for the templating method, further precise design of nanostructured metal oxides will be achieved.

Recently, inside deposition of TiO_2 within an assembly of silica nanospheres was achieved by using hydrothermal reaction.[61] A key point to achieve the inside deposition is preparation of TiO_2 nanoparticles within the template prior to the hydrothermal reaction.[61] Because the preformed TiO_2 nanoparticles worked as nuclei, TiO_2 was hydrothermally deposited within the templates. In addition, single crystalline frameworks were successfully formed within the templates in the report by using appropriate reaction conditions to form large crystalline domains.[62] As shown in this report, the use of hydrothermal deposition enables further design of nanostructured metal oxides which cannot be achieved by the conventional process using the thermal treatment.

1.4.3 Deposition methods of carbon

Deposition of carbon is mostly performed by high temperature heat treatment of organic compounds under inert gas flows. The degree of graphitization is most influential to the properties of carbon frameworks. Therefore, various strategies have been developed to achieve high degree of graphitization. CVD method at high temperature is also applied for the preparation of nanostructured carbon using the templating method.

Carbonization by high temperature heat treatment

The procedures of carbon deposition within silica templates are as follows. After introduction of organic compounds into the templates, acid catalysts, such as sulfonic acid and oxalic acid, are added to the carbon incorporated templates to promote dehydration condensation between the carbon precursors. The templates are heated at 100–300 °C, and then 700–900 °C under inert gas flows. Finally, the silica templates were removed with HF aq. or NaOH aq. Although heat treatment at higher temperature is desirable for graphitization (graphite is typically formed at 2300 °C), the collapse of nanostructures and/or formation of silicon carbide are undesirably occurred. Therefore, there need strategies to graphitize the carbon frameworks at lower temperature.

The use of aromatic compounds, such as naphthalene and anthracene, enables the formation of more graphitic frameworks. Because the compounds possess similar structures with graphite, the graphitic structures tend to form even at lower temperature. R. Ryoo et al. achieved the preparation of mesoporous carbon with graphitic frameworks using catalysts, such as Fe and Al, along with the aromatic compounds.[55] The transition metal catalysts are modified on the surfaces of the templates or incorporated into the templates. Owing to the use of the aromatic compounds and the catalysts, the carbon frameworks can be graphitized at moderate temperatures of *ca.* 900 °C.[55]

Chemical vapor deposition (CVD)

Although CVD method requires a special equipment, the method provides high degree of pore filling, resulting in dense pore walls without micropores within the frameworks.[4c] Owing to the use of vapor to incorporate carbon, the method is applied

for various templates. In addition, in order to fully fill the templates, the method is also used for additional incorporation of carbon after initial carbonization.[34a]

The degree of graphitization depends on both the temperature and carbon precursors. The use of acetonitrile was reported to be more effective to form highly graphitized carbon frameworks.[73]

1.4.4 Deposition methods of other compounds

In addition to metals, metal oxides, and carbon, various compositions, such as carbides, nitrides, fluorides, and chalcogenides, can be applied to the templating method. The deposition methods within the templates for such compounds may be roughly classified into the following three methods:[6d] 1) thermal decomposition of precursors including constituent atoms of targeted compounds (under inert gas flows if needed), 2) heat treatment of precursors under reactive gas flows, 3) heat treatment of corresponding metal oxides under reactive gas flows. In the thermal decomposition of precursors, the choice and/or preparation of appropriate precursors are the most important step. Inert gas flows are sometimes required for non-oxygen containing compounds to avoid oxygen impurities. The process of heat treatment of precursors under reactive gas flows is almost similar process with the metal deposition using H_2 gas flow. Outer deposition during the reactions must be avoided. In the process of heat treatment of corresponding metal oxides under reactive gas flows, much attention must be paid for the volume change during the transformation from oxides to targeted compounds. When the volume change is large, the nanostructures will collapse.

1.4.5 Summary

The deposition methods which have been applied for the templated preparation of nanostructured materials are overviewed for each composition. In the templating method, the inside deposition must be achieved for the successful preparation. Therefore, the deposition methods should be appropriately chosen. The applicable deposition methods are summarized in Table 1.2.

Table 1.2 Deposition methods applicable to the templating method.

Composition	Deposition method
Metals	Thermal reduction under H_2 gas flow, electrodeposition, electroless chemical deposition, UV reduction, and vapor phase deposition method
Metal oxides	Thermal decomposition and hydrothermal deposition
Carbon	Carbonization by high temperature heat treatment and chemical vapor deposition
Others (e.g. carbides, nitrides, and fluorides)	Thermal decomposition, heat treatments under reactive gas flows, and heat treatments of corresponding metal oxides under reactive gas flows

1.5 Significance and objective of this thesis

The templating method using nanostructured silica as a template has been demonstrated to be useful for the preparation of nanostructured materials as shown above. However, the controllability of several structural factors, such as crystallite sizes and crystal structures, is yet to be low, which is mainly because the deposition processes are not sufficiently sophisticated.

The purpose of this PhD study is to develop the deposition processes by rationally separating the processes into multistep for further design of nanostructured materials. The initially deposited compounds are expected to work as not only components of final products but also a seed to induce the crystal growth of the following deposited compounds. The seed compounds will be helpful for inside deposition of the following deposited compounds. In addition, the stepwise deposition should be advantageous for the preparation of nanostructured materials composed of two different compounds because appropriate deposition methods can be separately applied to deposition processes of each component. The ratio of the two components can be easily controlled by varying the number of deposition times.

The preparative methodologies using stepwise deposition within the templates, described in this thesis, enable further precise design of nanostructured materials which have not been achieved by conventional one step deposition. Therefore, this thesis surely contributes to synthetic chemistry of nanostructured materials, and accordingly nanomaterial chemistry.

1.6 References

1) G. A. Ozin, A. C. Arsenault, L. Cademartiri, "Nanochemistry A Chemical Approach to Nanomaterials, 2nd edition″, RSC Publishing, London (2009).

2) C. Burda, X. Chen, R. Narayanan, M. A. El-Sayed, *Chem. Rev.* **2005**, 105, 1025.

3) G. Schmid, "Nanoparticles from Theory to Application″, Wiley-VCH, Weinheim (2004).

4) a) G. R. Patzke, Y. Zhou, R. Kontic, F. Conrad, *Angew. Chem. Int. Ed.* **2011**, 50, 826; b) S. Guo, E. Wang, *Nano Today* **2011**, 6, 240; c) Y. Xia, Z. Yang, R. Mokaya,

Nanoscale **2010**, 2, 639; d) Z. Zhuang, Q. Peng, Y. Li, *Chem. Soc. Rev.* **2011**, 40, 5492.

5) a) B. Wu, N. Zheng, *Nano Today* **2013**, 8, 168; b) J. Gu, Y. W. Zhang, F. Tao, *Chem. Soc. Rev.* **2012**, 41, 8050; c) X. Liu, D. Wang, Y. Li, *Nano Today* **2012**, 7, 448; d) L. Carbone, P. D. Cozzoli, *Nano Today* **2010**, 5, 449; e) M. Niederberger, *Acc. Chem. Res.* **2007**, 40, 793; f) Z. Y. Zhou, N. Tian, J. T. Li, I. Broadwell, S. G. Sun, *Chem. Soc. Rev.* **2011**, 40, 4167.

6) a) Y. Liu, J. Goebl, Y. Yin, *Chem. Soc. Rev.* **2013**, 42, 2610; b) M. R. Jones, K. D. Osberg, R. J. MacFarlane, M. R. Langille, C. A. Mirkin, *Chem. Rev.* **2011**, 111, 3736; c) K. Egeblad, C. H. Christensen, M. Kustova, C. H. Christensen, *Chem. Mater.* **2008**, 20, 946; d) Y. Shi, Y. Wan, D. Zhao, *Chem. Soc. Rev.* **2011**, 40, 3854; e) A. Stein, B. E. Wilson, S. G. Rudisill, *Chem. Soc. Rev.* **2013**, 42, 2763; f) H. Nishihara, T. Kyotani, *Adv. Mater.* **2012**, 24, 4473; g) S. J. Hurst, E. K. Payne, L. Qin, C. A. Mirkin, *Angew. Chem. Int. Ed.* **2006**, 45, 2672; h) J. Lee, S. Han, T. Hyeon, *J. Mater. Chem.* **2004**, 14, 478.

7) S. E. Lohse, N. D. Burrows, L. Scarabelli, L. M. Liz-Marzán, C. J. Murphy, *Chem. Mater.* **2014**, 26, 34.

8) Z. Niu, Y. Li, *Chem. Mater.* **2014**, 26, 72.

9) E. Roduner, *Chem. Soc. Rev.* **2006**, 35, 583.

10) a) L. D. Hicks, M. S. Dresselhaus, *Phys. Rev. B* **1993**, 47, 16631; b) L. D. Hicks, M. S. Dresselhaus, *Phys. Rev. B* **1993**, 47, 12727; c) L. D. Hicks, T. C. Harman, M. S. Dresselhaus, *Appl. Phys. Lett.* **1993**, 63, 3230.

11) H. Ohta, S. Kim, Y. Mune, T. Mizoguchi, K. Nomura, S. Ohta, T. Nomura, Y. Nakanishi, Y. Ikuhara, M. Hirano, H. Hosono, K. Koumoto, *Nature Mater.* **2007**, 6, 129.

12) S. K. Bux, J. P. Fleurial, R. B. Kaner, *Chemical Communications* **2010**, 46, 8311.

13) R. Xu, W. Pang, J. Yu, Q. Huo, J. Chen, "Chemistry of Zeolites and Related Porous

Materials″, Wiley-VCH, Weinheim (2007).

14) K. Na, M. Choi, R. Ryoo, *Microporous Mesoporous Mater.* **2013**, 166, 3.

15) a) K. Na, C. Jo, J. Kim, K. Cho, J. Jung, Y. Seo, R. J. Messinger, B. F. Chmelka, R. Ryoo, *Science* **2011**, 333, 328; b) W. Fan, M. A. Snyder, S. Kumar, P. S. Lee, W. C. Yoo, A. V. McCormick, R. Lee Penn, A. Stein, M. Tsapatsis, *Nature Mater.* **2008**, 7, 984.

16) a) G. D. Stucky, J. E. Mac Dougall, *Science* **1990**, 247, 669; b) G. A. Ozin, C. Gil, *Chem. Rev.* **1989**, 89, 1749.

17) P. H. Kasai, *J. Chem. Phys.* **1965**, 43, 3322.

18) Y. Kim, K. Seff, *J. Am. Chem. Soc.* **1977**, 99, 7055.

19) a) T. Goto, Y. Nozue, T. Kodaira, *Mater. Sci. Eng. B* **1993**, 19, 48; b) Y. Nozue, T. Kodaira, S. Ohwashi, T. Goto, O. Terasaki, *Phys. Rev. B* **1993**, 48, 12253.

20) T. Bein, F. Schmidt, P. A. Jacobs, *Zeolites* **1985**, 5, 240.

21) M. Che, M. Richard, D. Olivier, *J. Chem. Soc., Faraday Trans. 1* **1980**, 76, 1526.

22) D. J. Elliott, J. H. Lunsford, *J. Catal.* **1979**, 57, 11.

23) L. F. Rao, A. Fukuoka, N. Kosugi, H. Kuroda, M. Ichikawa, *J. Phys. Chem.* **1990**, 94, 5317.

24) K. Moller, D. C. Koningsberger, T. Bein, *J. Phys. Chem.* **1989**, 93, 6116.

25) N. D. Triantafillou, J. T. Miller, B. C. Gates, *J. Catal.* **1995**, 155, 131.

26) J. De Graaf, A. J. Van Dillen, K. P. De Jong, D. C. Koningsberger, *J. Catal.* **2001**, 203, 307.

27) H. S. Park, K. Seff, *J. Phys. Chem. B* **2000**, 104, 2224.

28) J. E. Readman, I. Gameson, J. A. Hriljac, P. P. Edwards, P. A. Anderson, *Chem. Commun.* **2000**, 595.

29) Y. Okamoto, Y. Kobayashi, T. Imanaka, *Catal. Lett.* **1993**, 20, 49.

30) A. Carlsson, T. Oku, J. O. Bovin, G. Karlsson, Y. Okamoto, N. Ohnishi, O. Terasaki, *Chem. Eur. J.* **1999**, 5, 244.

31) E. I. Berdanova, A. M. Larin, O. L. Shakhnovskaya, B. V. Romanovsky, *Russ. Chem. Bull.* **1997**, 46, 1667.

32) A. L. Kustov, V. G. Kessler, B. V. Romanovsky, G. A. Seisenbaeva, D. V. Drobot, P. A. Shcheglov, *J. Mol. Catal. A: Chem.* **2004**, 216, 101.

33) a) S. A. Johnson, E. S. Brigham, P. J. Ollivier, T. E. Mallouk, *Chem. Mater.* **1997**, 9, 2448; b) T. Kyotani, T. Nagai, S. Inoue, A. Tomita, *Chem. Mater.* **1997**, 9, 609.

34) a) Z. Ma, T. Kyotani, A. Tomita, *Chem. Commun.* **2000**, 2365; b) H. Nishihara, Q. H. Yang, P. X. Hou, M. Unno, S. Yamauchi, R. Saito, J. I. Paredes, A. Martínez-Alonso, J. M. D. Tascón, Y. Sato, M. Terauchi, T. Kyotani, *Carbon* **2009**, 47, 1220.

35) a) T. Yanagisawa, T. Shimizu, K. Kuroda, C. Kato, *Bull. Chem. Soc. Jpn.* **1990**, 63, 988; b) J. S. Beck, J. C. Vartuli, W. J. Roth, M. E. Leonowicz, C. T. Kresge, K. D. Schmitt, C. T. W. Chu, D. H. Olson, E. W. Sheppard, S. B. McCullen, J. B. Higgins, J. L. Schlenker, *J. Am. Chem. Soc.* **1992**, 114, 10834; c) C. T. Kresge, M. E. Leonowicz, W. J. Roth, J. C. Vartuli, J. S. Beck, *Nature* **1992**, 359, 710.

36) a) Y. Wan, D. Zhao, *Chem. Rev.* **2007**, 107, 2821; b) K. Ariga, A. Vinu, Y. Yamauchi, Q. Ji, J. P. Hill, *Bull. Chem. Soc. Jpn.* **2012**, 85, 1.

37) M. Kruk, *Acc. Chem. Res.* **2012**, 45, 1678.

38) a) Y. Ren, Z. Ma, P. G. Bruce, *Chem. Soc. Rev.* **2012**, 41, 4909; b) H. Yang, D. Zhao, *J. Mater. Chem.* **2005**, 15, 1217; c) C. Zhu, D. Du, A. Eychmüller, Y. Lin, *Chem. Rev.* **2015**, 115, 8896; d) S. Yang, X. Luo, *Nanoscale* **2014**, 6, 4438.

39) R. Ryoo, S. H. Joo, S. Jun, *J. Phys. Chem. B* **1999**, 103, 7743.

40) S. Jun, J. Sang Hoon, R. Ryoo, M. Kruk, M. Jaroniec, Z. Liu, T. Ohsuna, O.

Terasaki, *J. Am. Chem. Soc.* **2000**, 122, 10712.

41) M. Imperor-Clerc, D. Bazin, M. D. Appay, P. Beaunier, A. Davidson, *Chem. Mater.* **2004**, 16, 1813.

42) W. Yue, C. Random, P. S. Attidekou, Z. Su, J. T. S. Irvine, W. Zhou, *Adv. Funct. Mater.* **2009**, 19, 2826.

43) F. Hoffmann, M. Cornelius, J. Morell, M. Fröba, *Angew. Chem. Int. Ed.* **2006**, 45, 3216.

44) Y. Wan, H. Yang, D. Zhao, *Acc. Chem. Res.* **2006**, 39, 423.

45) T. A. Crowley, K. J. Ziegler, D. M. Lyons, D. Erts, H. Olin, M. A. Morris, J. D. Holmes, *Chem. Mater.* **2003**, 15, 3518.

46) H. Li, H. Lin, S. Xie, W. Dai, M. Qiao, Y. Lu, H. Li, *Chem. Mater.* **2008**, 20, 3936.

47) A. Takai, Y. Doi, Y. Yamauchi, K. Kuroda, *Chem. - Asian J.* **2011**, 6, 881.

48) C. M. Yang, H. S. Sheu, K. J. Chao, *Adv. Funct. Mater.* **2002**, 12, 143.

49) Y. J. Han, J. M. Kim, G. D. Stucky, *Chem. Mater.* **2000**, 12, 2068.

50) P. Karthika, H. Ataee-Esfahani, Y. H. Deng, K. C. W. Wu, N. Rajalakshmi, K. S. Dhathathreyan, D. Arivuoli, K. Ariga, Y. Yamauchi, *Chem. Lett.* **2013**, 42, 447.

51) A. Takai, Y. Doi, Y. Yamauchi, K. Kuroda, *J. Phys. Chem. C* **2010**, 114, 7586.

52) a) A. Chernikov, S. Horst, T. Waitz, M. Tiemann, S. Chatterjee, *J. Phys. Chem. C* **2011**, 115, 1375; b) Q. Liu, A. Wang, X. Wang, T. Zhang, *Chem. Mater.* **2006**, 18, 5153.

53) C. Dickinson, W. Zhou, R. P. Hodgkins, Y. Shi, D. Zhao, H. He, *Chem. Mater.* **2006**, 18, 3088.

54) C. H. Kim, D. K. Lee, T. J. Pinnavaia, *Langmuir* **2004**, 20, 5157.

55) T. W. Kim, I. S. Park, R. Ryoo, *Angew. Chem. Int. Ed.* **2003**, 42, 4375.

56) S. H. Joo, S. J. Choi, I. Oh, J. Kwak, Z. Liu, O. Terasaki, R. Ryoo, *Nature* **2001**, 412,

169.

57) a) H. Jiang, J. Ma, C. Li, *Adv. Mater.* **2012**, 24, 4197; b) H. Huwe, M. Fröba, *Carbon* **2007**, 45, 304.

58) a) Y. Xia, B. Gates, Y. Yin, Y. Lu, *Adv. Mater.* **2000**, 12, 693; b) R. Watanabe, T. Yokoi, E. Kobayashi, Y. Otsuka, A. Shimojima, T. Okubo, T. Tatsumi, *J. Colloid Interface Sci.* **2011**, 360, 1.

59) S. G. Rudisill, Z. Wang, A. Stein, *Langmuir* **2012**, 28, 7310.

60) Y. Kuroda, K. Kuroda, *Angew. Chem. Int. Ed.* **2010**, 49, 6993.

61) a) W. Jiao, Y. Xie, R. Chen, C. Zhen, G. Liu, X. Ma, H. M. Cheng, *Chem. Commun.* **2013**, 49, 11770; b) E. J. W. Crossland, N. Noel, V. Sivaram, T. Leijtens, J. A. Alexander-Webber, H. J. Snaith, *Nature* **2013**, 495, 215.

62) H. G. Yang, C. H. Sun, S. Z. Qiao, J. Zou, G. Liu, S. C. Smith, H. M. Cheng, G. Q. Lu, *Nature* **2008**, 453, 638.

63) W. C. Yoo, S. Kumar, Z. Wang, N. S. Ergang, W. Fan, G. N. Karanikolos, A. V. McCormick, R. L. Penn, M. Tsapatsis, A. Stein, *Angew. Chem. Int. Ed.* **2008**, 47, 9096.

64) H. J. Shin, R. Ryoo, Z. Liu, O. Terasaki, *J. Am. Chem. Soc.* **2001**, 123, 1246.

65) a) H. Yan, C. F. Blanford, B. T. Holland, M. Parent, W. H. Smyrl, A. Stein, *Adv. Mater.* **1999**, 11, 1003; b) H. Yan, C. F. Blanford, J. C. Lytle, C. Barry Carter, W. H. Smyrl, A. Stein, *Chem. Mater.* **2001**, 13, 4314.

66) Y. Kanno, T. Suzuki, Y. Yamauchi, K. Kuroda, *J. Phys. Chem. C* **2012**, 116, 24672.

67) U. H. Lee, J. H. Lee, D. Y. Jung, Y. U. Kwon, *Adv. Mater.* **2006**, 18, 2825.

68) A. Fukuoka, M. Ichikawa, *Top. Catal.* **2006**, 40, 103.

69) A. Blanco, E. Chomski, S. Grabtchak, M. Ibisate, S. John, S. W. Leonard, C. Lopez, F. Meseguer, H. Miguez, J. P. Mondla, G. A. Ozin, O. Toader, H. M. Van Driel, *Nature*

2000, 405, 437.

70) M. Kobayashi, Y. Kanno, K. Kuroda, *Chem. Lett.* **2014**, 43, 846.

71) Q. Jiang, M. D. Ward, *Chem. Soc. Rev.* **2014**, 43, 2066.

72) X. Chen, S. S. Mao, *Chem. Rev.* **2007**, 107, 2891.

73) Y. Xia, R. Mokaya, *Adv. Mater.* **2004**, 16, 1553.

Chapter 2

The Critical Effect of Niobium Doping on the Formation of Mesostructured TiO_2: Single-Crystalline Ordered Mesoporous Nb-TiO_2 and Plate-like Nb-TiO_2 with Ordered Mesoscale Dimples

Chapter 2

2.1 Introduction

Since the discovery of ordered mesoporous silica in the early 1990s,[1] ordered mesoporous materials with different chemical compositions have been actively studied. Among various mesoporous materials, mesoporous TiO_2 is one of the most attractive materials because of various potential applications, such as catalysts, dye-sensitized solar cells, and lithium-ion batteries.[2] For these applications, the mesostructure of TiO_2 (for example, surface area, pore volume, pore size, and so on) must be controlled. Also, the crystal structure, crystallite size, and the level of doping of heteroatoms into TiO_2 must be controlled, which is essentially important, because all of these three factors greatly affect the properties of mesoporous TiO_2. For example, higher electrical conductivity and higher efficiency of charge carrier separation of TiO_2 has been realized by 1) doping of heteroatoms into the frameworks, 2) full crystallization, and 3) increase in the crystallite size.[2,3] Furthermore, doping of heteroatoms enables visible light to be absorbed, which is due to the formation of intermediate energy levels, thus meaning that solar energy can be used more effectively.[2] One of the ultimate goals in the development of this field is to prepare mesoporous TiO_2 with single-crystalline frameworks and controlled doping. However, there have been no successful reports on this topic.

Two major approaches to prepare mesoporous TiO_2 are soft-[4] and hard-templating methods.[2,5] Neither crystallinity nor doping of mesoporous TiO_2 can be controlled by soft templating. Preparation of mesoporous TiO_2 by soft templating is carried out through cooperative assembly between titanium species and organic surfactants, followed by template removal. Precise control of hydrolysis and condensation rates of Ti precursors is required to achieve the cooperative assembly because Ti precursors tend to form precipitates prior to the cooperative assembly owing

to their high reactivity. Therefore, the method is unsuitable to control the dopant concentration because the addition of different metal species into a Ti precursor solution affects the hydrolysis and condensation rates of the precursor. Furthermore, formed mesostructures tend to collapse during the removal of templates and the subsequent crystallization by calcination. In particular, high-temperature calcination, which is generally required to obtain fully crystallized TiO_2 frameworks with controlled crystallite size or a high-temperature phase (rutile), inevitably causes serious collapse of the mesostructure.[2a,c,4b,f] Therefore, the method is unsuitable to control the crystallite size and crystal structure along with retaining the mesostructure.[6]

Mesoporous TiO_2 can be prepared by hard-templating method by the following three steps: 1) infiltration of Ti precursor inside spaces/pores of hard templates, 2) deposition of TiO_2 typically by calcination, and 3) removal of the template. However, the method has suffered from controlling the single-crystallinity of formed mesoporous TiO_2, because TiO_2 frameworks prepared by this method reported to date are nanocrystalline even after full crystallization, which is not useful to achieve higher electrical conductivity and charge carrier separation efficiency.[5] On the other hand, the control of doping of heteroatoms by this method is easier than by the soft-templating method because the process of the method is very simple without complicated sol–gel processes.[5b–d]

Recently, single-crystalline mesoporous TiO_2 has been successfully prepared by using a silica nanoparticle assembly as template,[3] though we should point out that the mesostructure is not so ordered. In those reports, the single-crystalline frameworks were achieved by using a hydrothermal process that had not been used for hard-templating method. Another efficient key is the introduction of Ti species into hard templates prior

to a hydrothermal process to deposit TiO_2 exclusively inside the template. Because it is generally known that the crystal structure, crystallite size, and dopant concentration of TiO_2 can be better controlled by the hydrothermal process than calcination,[7] it is expected that more sophisticated mesoporous TiO_2 can be prepared by using the method reported previously.[3] However, single-crystalline mesoporous TiO_2 with ordered mesostructure, which is promising for higher diffusivity of guest species,[2c] has not yet been achieved. Furthermore, doping of heteroatoms into the single-crystalline mesoporous TiO_2 frameworks has not been achieved, either.

This chapter shows that mesoporous TiO_2 with both ordered mesostructure and single-crystalline frameworks was prepared by using silica colloidal crystals as a template (Scheme 2.1), and the ordering is much higher than those reported previously.[3] Because the diameter of silica nanoparticles, which determines the pore size of mesoporous TiO_2, can be controlled in a wide range from nanometer to submicrometers,[8] the template was chosen. Furthermore, Nb, which is very promising to effectively enhance the performance of TiO_2 among other dopants,[9] is doped into the single-crystalline TiO_2 frameworks. This is the first report that has achieved the preparation of ordered mesoporous TiO_2 with single-crystalline and Nb-doped TiO_2 frameworks. Furthermore, to our surprise, the addition of a Nb precursor leads to the formation of plate-like Nb-doped TiO_2 with ordered mesoscale dimples (Scheme 2.1). This Nb-doped TiO_2 is thought to be formed by crystal growth directly on the surface of the silica template.

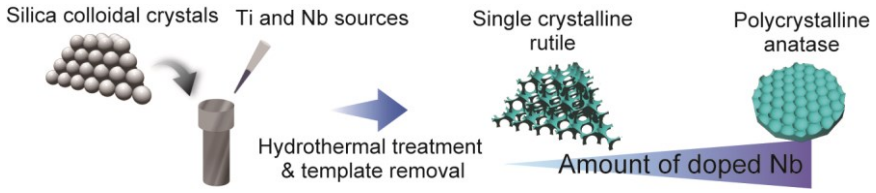

Scheme 2.1 Preparation of single-crystalline mesoporous Nb-TiO_2 and plate-like Nb-doped TiO_2 with ordered mesoscale dimples

2.2 Experimental

2.2.1 Materials

Tetraethoxysilane (TEOS, Wako Pure Chemical Industries, Ltd.) and tris(hydroxymethyl)aminomethane (THAM, Wako Pure Chemical Industries, Ltd.) were used for the preparation of silica colloidal crystals. Titanium tetrachloride (Wako Pure Chemical Industries, Ltd.) was used for the preparation of Ti-containing silica colloidal crystals. Tetrabutoxytitanium (TBOT, Wako Pure Chemical Industries, Ltd.) was purified by distillation. The purified TBOT and niobium(V) chloride (Wako Pure Chemical Industries, Ltd.) were used as the Ti and Nb precursors, respectively. Concentrated hydrochloric acid (Wako Pure Chemical Industries, Ltd.) was used for the hydrothermal process.

2.2.2 Preparation of silica colloidal crystals

Silica colloidal crystals were prepared by slightly modifying the conditions reported previously.[15] THAM (12.1 g, 1.00×10^{-2} mol) was dissolved in water (500 mL), and the solution was stirred at 80 °C for 10 min. TEOS (100 mL, 0.451 mol) was added into the solution, and the mixture was stirred at 80 °C for 24 h. Then, the colloidal solution was cooled to room temperature. To grow the particles size of silica nanoparticles, the procedure described above was basically repeated (seed-growth

method). An aqueous solution of THAM (0.2 M, 375 mL) was mixed with the obtained colloidal solution (125 mL), and the mixture was stirred at 80 °C C for 10 min. TEOS (175 mL, 0.790 mol) was added to the mixture, and the mixture was stirred at 80 °C for 24 h. Then, the obtained colloidal solution was cooled to room temperature. Silica colloidal crystals were obtained by drying the colloidal solution at 50 °C, and by the subsequent calcination at 550 °C for 6 h. The obtained silica colloidal crystals were lump-like with a few millimeters in size.

2.2.3 Preparation of Ti-containing silica colloidal crystals

The Ti-containing silica colloidal crystals that were used as a template were prepared according to a previous report.[3] As explained previously,[3] the incorporation of Ti species into the silica colloidal crystal is required to deposit TiO_2 by a hydrothermal process exclusively inside the template. A stock solution (2 M $TiCl_4$) was prepared by mixing water (7 mL), conc. HCl (20 mL), and $TiCl_4$ (2 mL) at ice bath temperature. The stock solution was diluted to 15 mM with water. The prepared silica colloidal crystals (5.0 g) were immersed in a 15 mM $TiCl_4$ solution (33 mL) at 70 °C for 1 h. After filtration of the aqueous solution, the colloidal crystals were washed with water. Ti-containing silica colloidal crystals were obtained after calcination at 550 °C for 30 min.

2.2.4 Preparation of single-crystalline mesoporous Nb-TiO_2

TBOT (0.8 mL) and a certain amount of conc. HCl solution of 0.2 M $NbCl_5$ (59 mL, 119 mL, or 240 mL) were added to a mixture of conc. HCl (28 mL) and H_2O (28 mL). The molar ratio of Ti:Nb in the reaction mixture was 1:0.005, 1:0.01, or 1:0.02.

Then the prepared Ti-containing silica colloidal crystals were added to the mixture. Hydrothermal treatment was performed at 150 °C for 12 h. Silica colloidal crystal/TiO_2 nanocomposites were obtained after filtration of the solution and washing with water. Finally, the nanocomposites were stirred in 2 M NaOH aqueous solution at 80 °C for 2 h to remove the silica template. The obtained samples were denoted as Nb(X)-TiO_2, where X means 100×Nb/(Ti+Nb) calculated from the quantitative analysis data by inductively coupled plasma optical emission spectroscopy (ICP-OES) measurement. For comparison, single-crystalline mesoporous TiO_2 was prepared without the addition of Nb.

2.2.5 Characterization

Transmission electron microscopy (TEM) images and selected-area electron diffraction (SAED) patterns were taken by a JEOL JEM-2010 microscope using an accelerating voltage of 200 kV. Scanning electron microscopy (SEM) images were taken by a Hitachi S-5500 electron microscope at an accelerating voltage of 2.0 kV for the silica template or 15.0 kV for TiO_2 samples. Scanning transmission electron microscopy (STEM) images and energy-dispersive X-ray (EDX) spectral mappings were conducted on a JEOL JEM-2100F microscope using an accelerating voltage of 200 kV. Samples for TEM, SEM, and STEM measurements were dispersed in ethanol, and the solutions were dropped on a carbon-coated microgrid (Okenshoji. Co). To conduct SEM observation of the nanocomposite, the lump of the nanocomposite was mounted on the carbon tape after cleaving the lump. The particle size of the silica nanoparticles was estimated by measuring the size of 50 nanoparticles in the TEM images. X-ray diffraction (XRD) patterns at very small diffraction angles were recorded with a Rigaku

NANO-Viewer using CuKα radiation under the operating conditions of 40 kV and 30 mA and a Pilatus 2D X-ray detector (Dectris). N_2 adsorption–desorption isotherms were measured with a MicrotracBEL BELSORP-max at –196 °C. The samples for the N_2 adsorption–desorption measurements were preheated at 120 °C under vacuum. High-angle XRD patterns were recorded with a Rigaku RINT-Ultima III diffractometer using CuKα radiation under the operating conditions of 40 kV and 40 mA. ICP-OES analysis was conducted on a Thermo Scientific iCAP 6500 Duo-ICP-OES. XPS profiles were measured with a ULVAC-PHI PHI 5000 VersaProbe II using monochromated AlKα radiation.

2.3 Results and discussion

2.3.1 Preparation of Ti-containing silica colloidal crystals

The Ti/Si ratio was calculated to be 2.9×10^{-4} from an ICP-OES analysis. The TEM images (Figure 2.1a–c) and the XRD pattern at very small angles (Figure 2.1d) clearly showed that silica nanoparticles *ca.* 30 nm in diameter were arranged in a face-centered

cubic lattice. These data mean that silica colloidal crystals were successfully formed. The steep increase in the N_2 adsorption–desorption isotherm (Figure 2.2) indicates the formation of uniform pores, supporting the formation of the colloidal crystals. In the low-magnification SEM image (Figure 2.3), TiO_2 bulk particles were not observed outside the template, indicating that TiO_2 was deposited inside the template. This is consistent with the effect of a very small amount of Ti atoms located on the surfaces of silica nanoparticles to avoid the deposition outside of the template, reported previously.[3] In the high-angle XRD pattern (Figure 2.4), the broad peak at 2θ=20–30°, which should

be due to amorphous silica, was observed. Considering that TiO_2 should crystallize after calcination at 550 °C, no peaks assignable to TiO_2 phase suggested two possibilities. One is that the amount of TiO_2 in the template was too small to observe the peaks assignable to crystalline TiO_2 in the XRD pattern. The other is that the crystallite size of TiO_2 crystals was too small to detect as peaks in the XRD pattern.

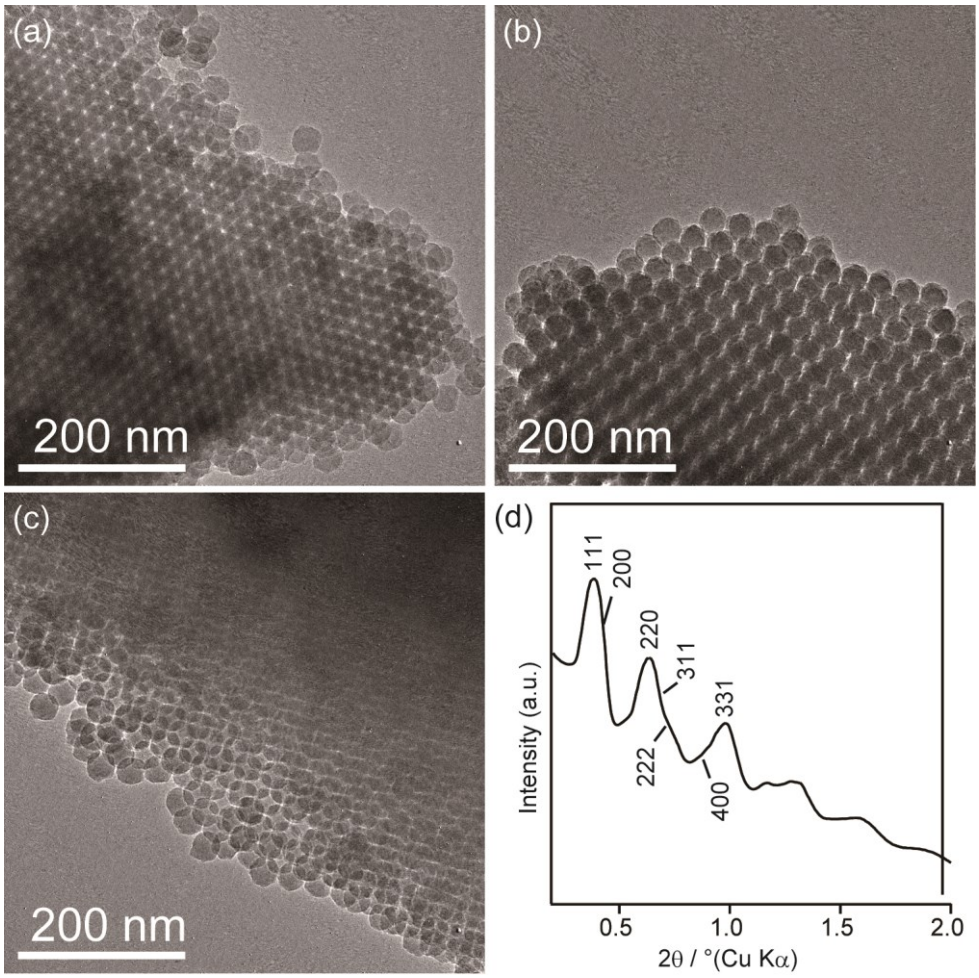

Figure 2.1 TEM images of the Ti-containing silica colloidal crystals taken along a) [111], b) [110], and c) [100] zone axes. d) Small-angle XRD pattern of the Ti-containing silica colloidal crystals.

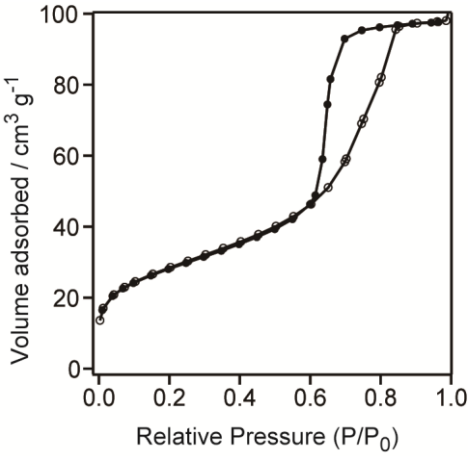

Figure 2.2 N_2 adsorption-desorption of the Ti-containing silica colloidal crystals.

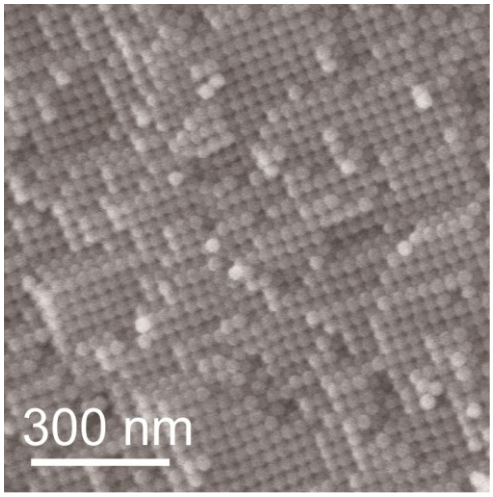

Figure 2.3 Low-magnified SEM image of the Ti-containing silica colloidal crystals.

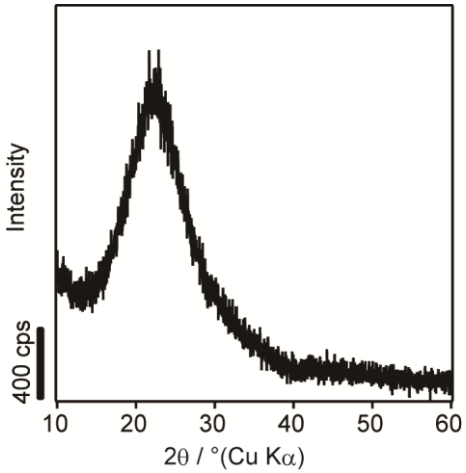

Figure 2.4 XRD pattern of the Ti-containing silica colloidal crystals.

2.3.2 Analysis of chemical composition and crystal structure of Nb(X)-TiO_2

The dopant concentrations of Nb(X)-TiO_2 are shown in Table 2.1. In the three samples prepared by adding Nb, the Nb/(Ti+Nb) ratios were larger than those of the starting reaction mixtures. This may be explained by the preferential deposition of Nb species to Ti species, owing to the stronger Ti–O–Nb bond than Ti–O–Ti bond,[10] under the presence of residual Ti and/or Nb species in the reaction mixture after the hydrothermal treatment.

Table 2.1 Molar ratios of Nb(X)-TiO_2.

Nb/(Ti + Nb) in the starting reaction mixture	Nb/ (Ti + Nb)	Si/ (Ti + Nb)	Sample name
0.0	0.0	0.0	Nb(0)-TiO_2
0.5×10^{-2}	1.6×10^{-2}	3.1×10^{-2}	Nb(1.6)-TiO_2
1.0×10^{-2}	4.4×10^{-2}	2.1×10^{-2}	Nb(4.4)-TiO_2
2.0×10^{-2}	7.4×10^{-2}	1.7×10^{-2}	Nb(7.4)-TiO_2

The XPS peaks at about 464, 458, 210, and 207 eV were assigned to Ti $2p_{1/2}$, Ti $2p_{3/2}$, $Nb3d_{3/2}$, and Nb $3d_{5/2}$, respectively (Figure 2.5). The peaks at 206.8 eV can be assigned to Nb^{5+}, and no peaks due to Nb^{4+} (ca. 206 eV) were observed. The peak at 458.2 eV of Nb(X)-TiO_2 (X=0) and the peaks at 458.4 eV of Nb(X)-TiO_2 (X=1.6, 4.4, and 7.4) were assigned to Ti^{4+}. The difference in the binding energy between pure TiO_2 and Nb-doped TiO_2 samples is attributed to the presence of Nb. The shoulder peaks around 457 eV newly appeared in the XPS profiles of Nb-doped TiO_2 samples, and the peaks became more obvious with the increase in the amount of Nb. The shoulder peaks indicate the presence of Ti^{3+} in the TiO_2 lattice, meaning that the charge compensation of Nb^{5+} can be mainly achieved by reducing Ti^{4+} to Ti^{3+}.[4i,11]

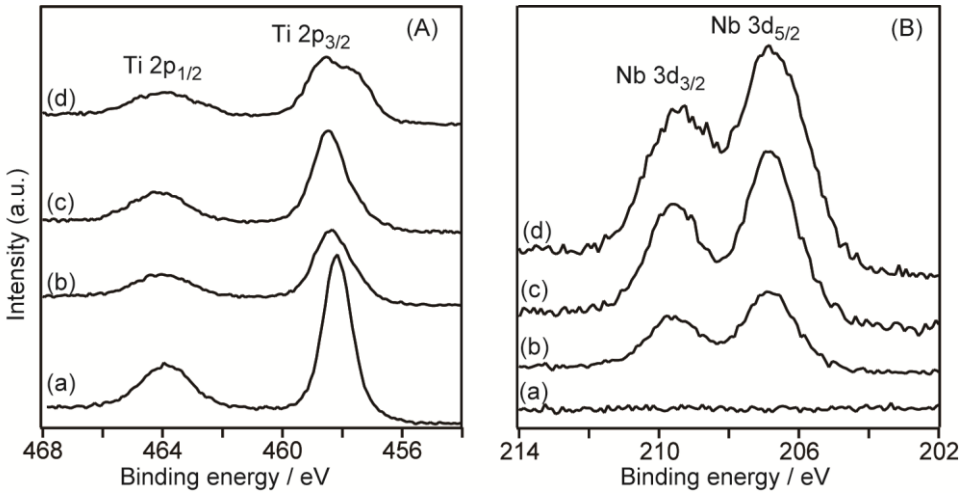

Figure 2.5 XPS profiles of Nb(X)-TiO_2 : X=a) 0, b) 1.6, c) 4.4, and d) 7.4 for A) 454–468 eV and B) 202 eV-214 eV.

The XRD pattern of Nb(0)-TiO_2 (Figure 2.6A) shows that the crystal phase of the product is mainly rutile and peaks due to brookite are slightly observed. It has already been reported that hydrothermal treatment under highly concentrated HCl conditions resulted in the formation of a high-temperature rutile phase.[3a,12]

With an increase in the amount of Nb, the intensity due to peaks of anatase phase increased, and the intensities of the peaks due to rutile and brookite phases decreased. In the XRD pattern of Nb(7.4)-TiO_2, only the peaks that are due to anatase were observed. The formation of an anatase phase in the presence of Nb can be explained by the stronger Nb–O–Ti bond, and the bond hinders the formation of the rutile phas.[9e,10a] Furthermore, all the peaks in the XRD patterns were very sharp, indicating the crystallite sizes were not so small, unlike conventional mesoporous TiO_2 with polycrystalline frameworks.[2,4,5] It should be noted that no peaks that are due to Nb or Nb-Ti oxides were observed, which strongly supports that all Nb atoms are successfully used to substitute with Ti sites of TiO_2 crystals as discussed below.

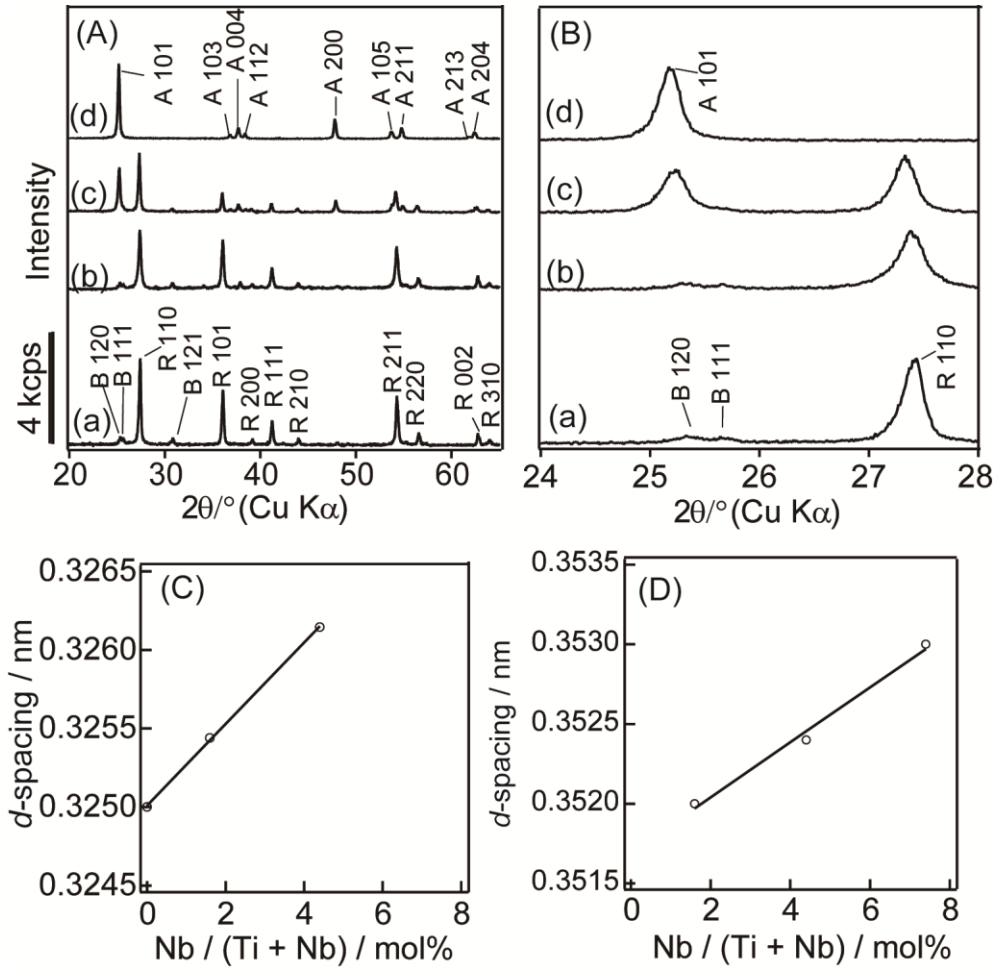

Figure 2.6 XRD patterns of Nb(X)-TiO_2 ; X=a) 0, b) 1.6, c) 4.4, and d) 7.4 for A) between 20–65° and B) between 24–28°. The peaks marked as B, R, and A are assigned to brookite, rutile, and anatase, respectively. The lattice spacings of Nb(X)-TiO_2 (X=0, 1.6, 4.4, or 7.4) calculated from C) the 110 diffraction of rutile phase and D) 101 diffraction of anatase phase as a function of the dopant concentrations.

The diffraction peaks of all Nb-doped samples are shifted to lower angle with the increase in the amount of Nb, corresponding to the increase in the *d*-spacings (Figure 2.6B). This data clearly indicates that Ti was substituted with Nb because both of the ionic radii of Nb^{5+} (0.64 Å) and Ti^{3+} (0.67 Å), which were actually detected in the XPS profiles of the Nb-doped samples, are larger than that Ti^{4+} (0.61 Å). Furthermore, the *d*-spacings of Nb(X)-TiO_2 calculated from the 110 diffraction of rutile and the 101

diffraction of anatase increased linearly with the amount of Nb (Figure 2.6C and 2.6D). Because any peaks that are due to Nb- or Nb-Ti-based oxides were not observed, all Nb atoms must have substituted for Ti sites in the TiO_2 lattice.

2.3.3 Characterization of nanostructured Nb(X)-TiO_2

The SEM image of Nb(0)-TiO_2 (Figure 2.7) showed that the three-dimensionally ordered mesoporous structure replicated from the template was formed. The pore size was estimated as approximately 30 nm, which was almost the same as the size of the silica nanoparticles. To our surprise, not only the three-dimensional mesoporous structure (Figure 2.7b,c) but also a dimpled surface without window pores (Figure 2.8) was observed for Nb(1.6)-TiO_2 and Nb(4.4)-TiO_2. Furthermore, only the dimpled surface was observed for Nb(7.4)-TiO_2. The diameter of the dimples was almost the same as those of the silica nanoparticles, and the arrangement of the dimples were the same as that of the silica nanoparticles. These data clearly show that both the three-dimensional mesoporous structure and the dimpled structure were copresent, formed by replicating the template. These very unique dimpled surface structures will be characterized and discussed later.

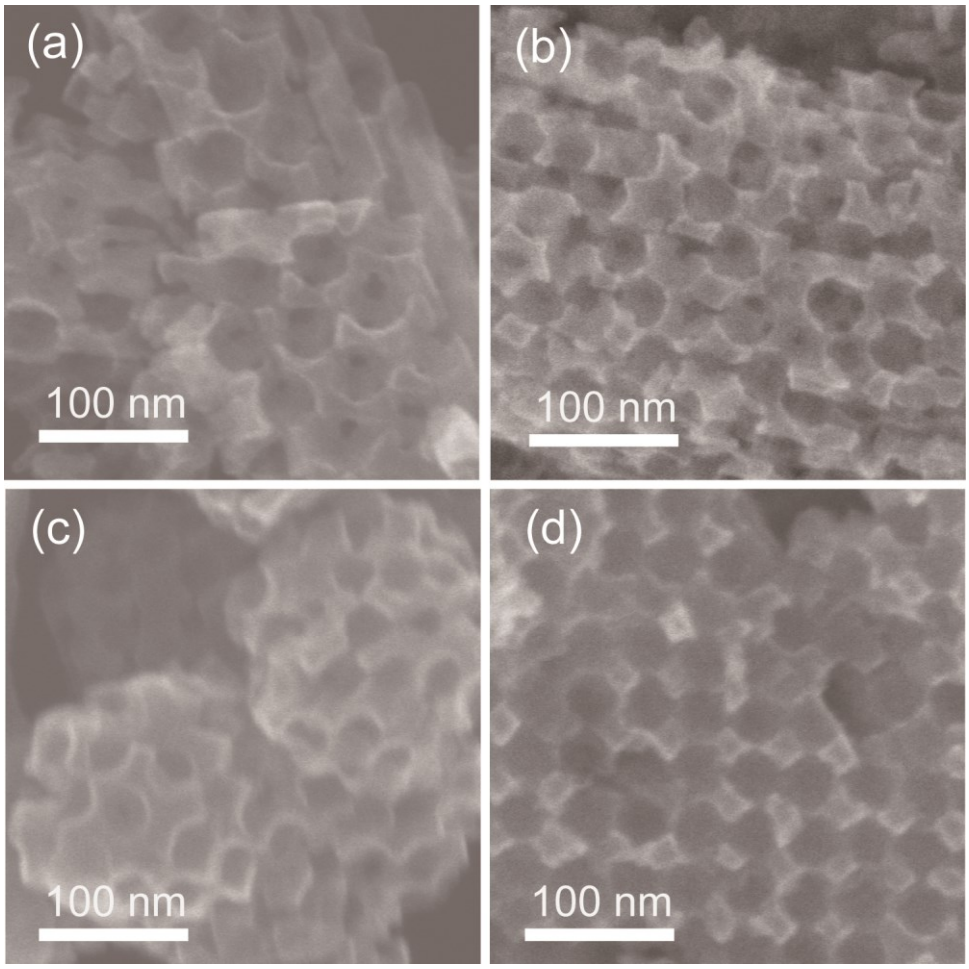

Figure 2.7 SEM images of Nb(X)-TiO_2 ; X=a) 0, b) 1.6, c) 4.4, and d) 7.4.

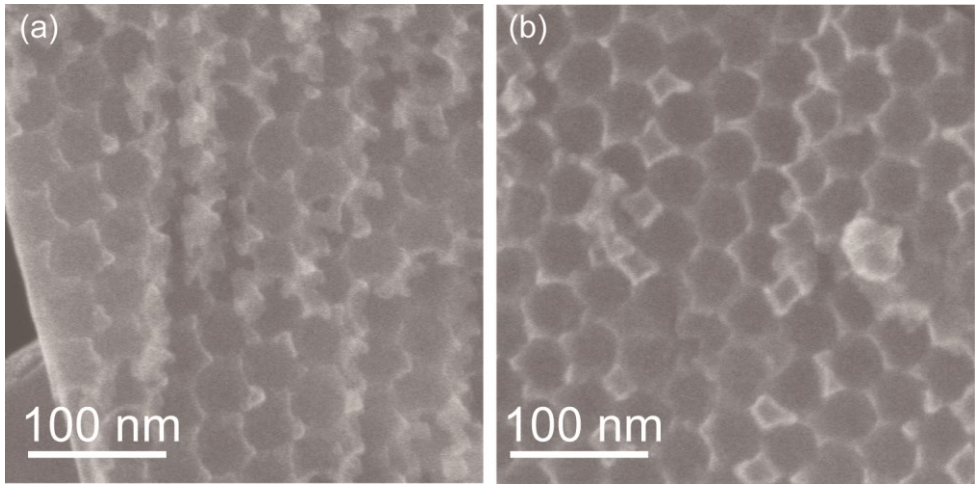

Figure 2.8 SEM images of dimpled Nb-doped TiO_2 observed for (a) Nb(1.6)-TiO_2 and (b) Nb(4.4)-TiO_2.

2.3.4 Characterization of single-crystalline mesoporous Nb-TiO_2

In the TEM images of Nb(X)-TiO_2 (X=0, 1.6, and 4.4; Figure 2.9, top), overlaps of mesopores, which are characteristic of three-dimensional porous materials, were observed. The SAED patterns of the particles with three-dimensional mesoporous structure (Figure 2.9, bottom) showed intense spots that are attributed to the single-crystalline rutile phase, indicating the mesoporous particles had single-crystalline TiO_2 frameworks. Furthermore, Nb atoms were uniformly distributed in mesoporous Nb-doped TiO_2 particles, as shown in EDX spectral mappings (Figure 2.10). These data are consistent with the peak shifts observed in the XRD patterns.

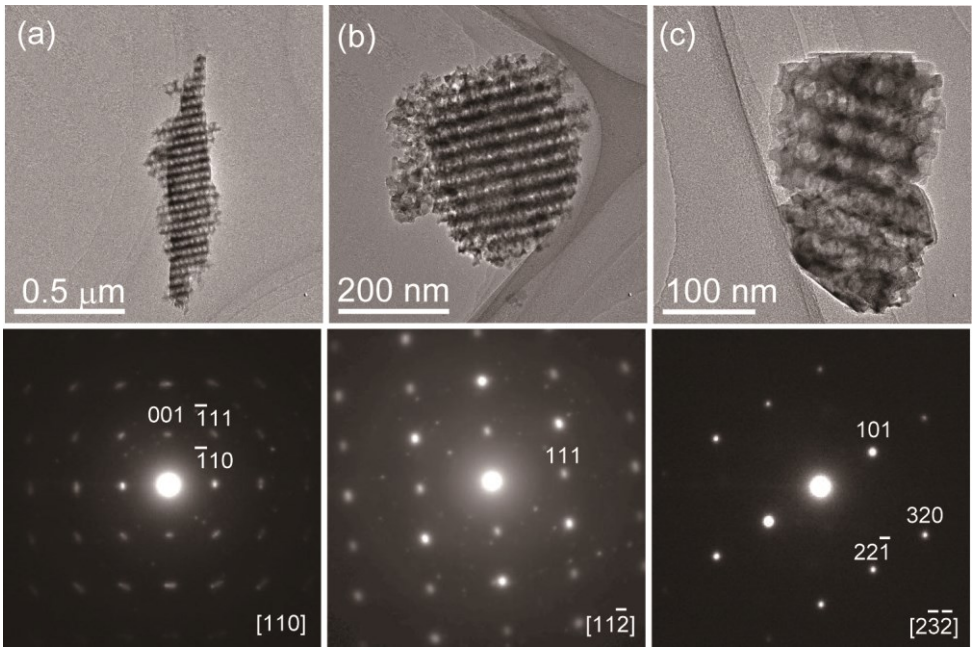

Figure 2.9 TEM images (top) and the corresponding SAED patterns (bottom) of three-dimensional mesoporous Nb-doped TiO_2 observed for a) Nb(0)-TiO_2, b) Nb(1.6)-TiO_2, and c) Nb(4.4)-TiO_2.

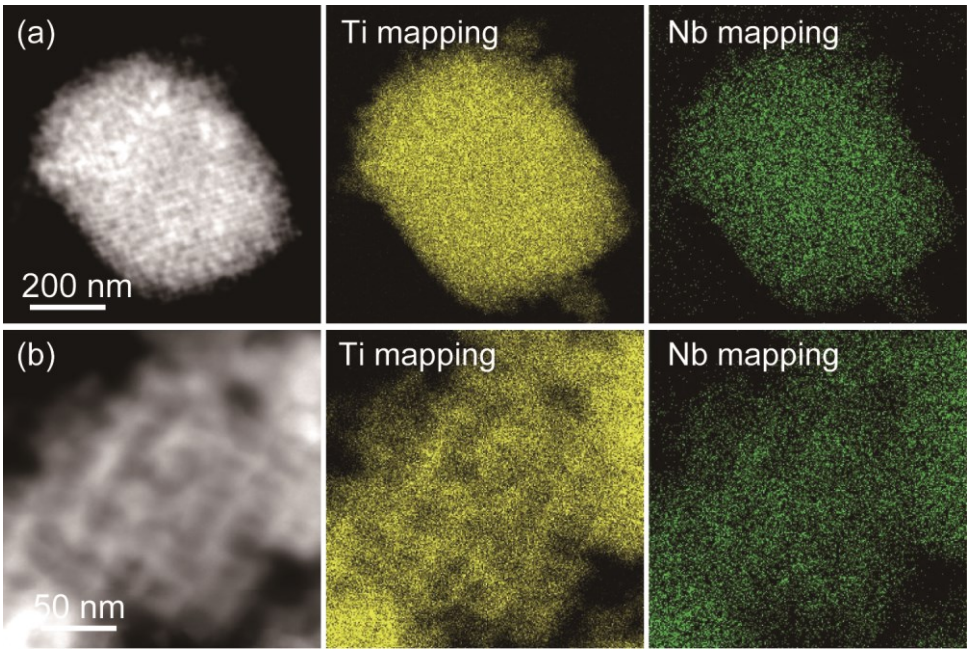

Figure 2.10 BF-STEM images (left) and the corresponding EDX spectral mappings (center and right) of mesoporous Nb-doped TiO_2 observed for (a) Nb(1.6)-TiO_2 and (b) Nb(4.4)-TiO_2.

In the small-angle XRD patterns of Nb(X)-TiO_2 (X=0, 1.6, and 4.4; Figure 2.11), the peaks were observed at the same positions as those of the original silica template though the intensity and resolution of the peaks were slightly lower than those of the template. These results definitely show the successful formation of mesoporous Nb-doped TiO_2 with both single-crystalline frameworks and a highly ordered pore arrangement. The materials reported herein should have higher electrical conductivity than those of conventional polycrystalline mesoporous Nb-doped TiO_2 owing to the single-crystallinity.[4i] Furthermore, the diffusivity of guest species in the samples should be higher than those in single-crystalline mesoporous TiO_2 reported previously owing to the ordered pore arrangement and three-dimensional interconnected pores.[2c,13] For these reasons, the materials reported here are expected to show superior performance in lithium-ion batteries, catalysts, dye-sensitized solar cells, and so on, because almost all requirements for mesoporous Nb-doped TiO_2 are now fulfilled.

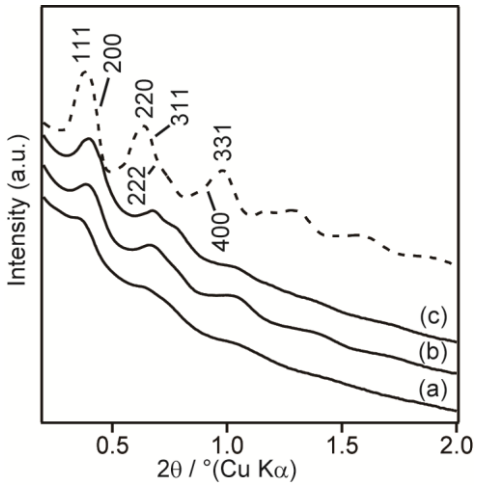

Figure 2.11 Small angle XRD patterns; solid line: Nb(X)-TiO_2 (X = (a) 0, (b) 1.6, and (c) 4.4); dotted line: Ti-containing silica colloidal crystals shown in Figure 2.1.

2.3.5 Characterization of dimpled Nb-doped TiO_2

As shown in Figure 2.7d and 2.8, unique dimpled structures were formed along with the mesoporous structure when the Nb precursor was added. The ratio of the dimpled structure to the mesoporous structure increased with the increase in the amount of Nb, and all the particles observed for Nb(7.4)-TiO_2 were plate-like with dimpled surfaces.

The TEM images and the corresponding SAED patterns of the dimpled structures are shown in Figure 2.12. The SAED patterns showed ring-like patterns with many intense spots attributed to the anatase phase, meaning that the dimpled structures were polycrystalline anatase. The tendency of the increase in the amount of the phase exhibiting dimples is consistent with the increase in the peak intensities of anatase in the XRD patterns. Thus, it is reasonable that the formation of anatase induced by the addition of Nb is strongly related to the formation of the dimpled structures.

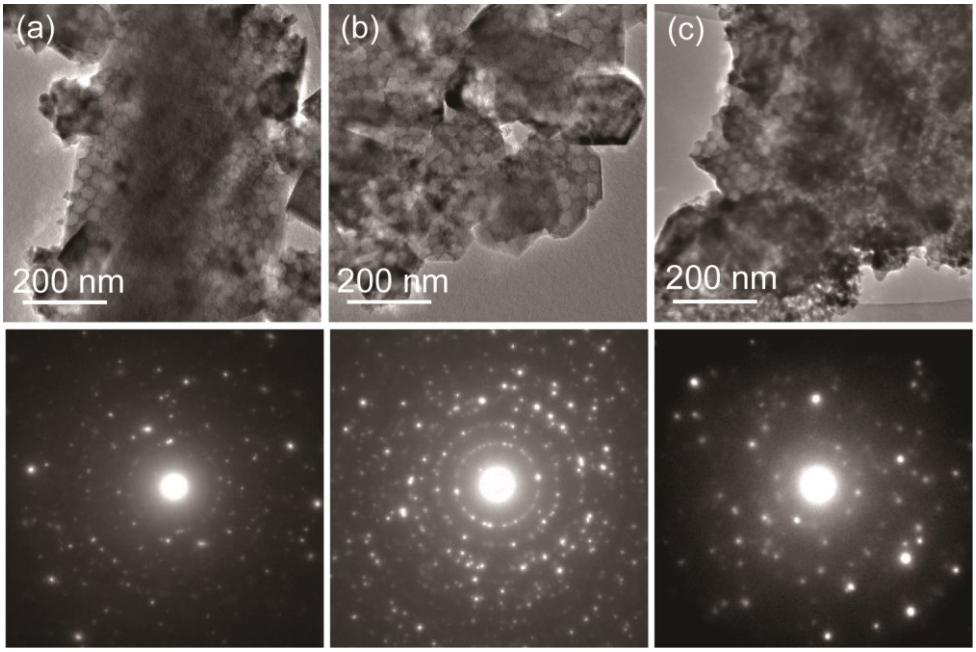

Figure 2.12 TEM images (top) and the corresponding SAED patterns (bottom) of nanodimpled Nb-doped TiO_2 observed for a) Nb(1.6)-TiO_2, b) Nb(4.4)-TiO_2, and c) Nb(7.4)-TiO_2.

The dimpled structures were formed by the deposition of TiO_2 on the surface of the template, as discussed below, which is completely different from dimpled Au nanoplate formed in the interstices of silica nanoparticles.[14]

The surface observation of Nb(7.4)-TiO_2 with the template was conducted after cleaving the nanocomposite (Figure 2.13). The SEM image of cleaved surface, which was not exposed to the solution during the hydrothermal treatment, showed an ordered arrangement of silica nanoparticles without any TiO_2 particles. In contrast, the entire surface of the exposed surface was covered with square-shaped particles. Furthermore, the opposite surface of the particle shown in Figure 2.7d was also covered with the square-shaped particles (Figure 2.14). These data indicate that dimpled structures were formed by replication of the surfaces of the template. The surface replication by a bottom-up process, such as a hydrothermal method, is actually unique because normal

deposition on the surface results in the formation of bulk materials without any specific surfaces. Probably the presence of a small amount of Ti on the silica colloidal crystals influences the initial stage of deposition of Ti species directly on the surfaces of assembled silica nanoparticles.

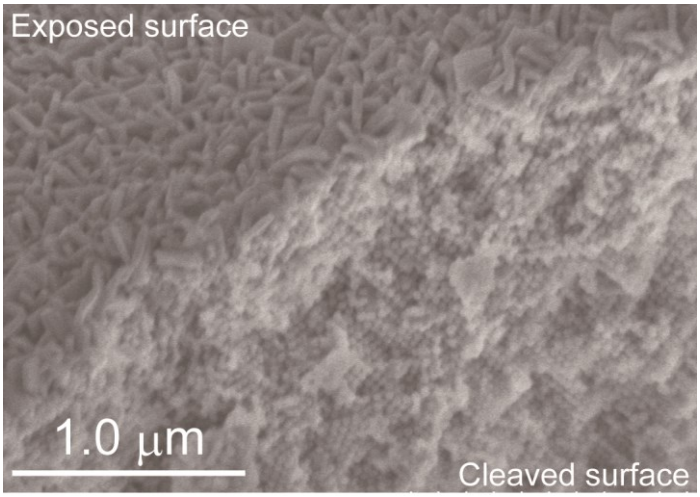

Figure 2.13 SEM image of Nb(7.4)-TiO_2 with the template nanocomposite after cleaving.

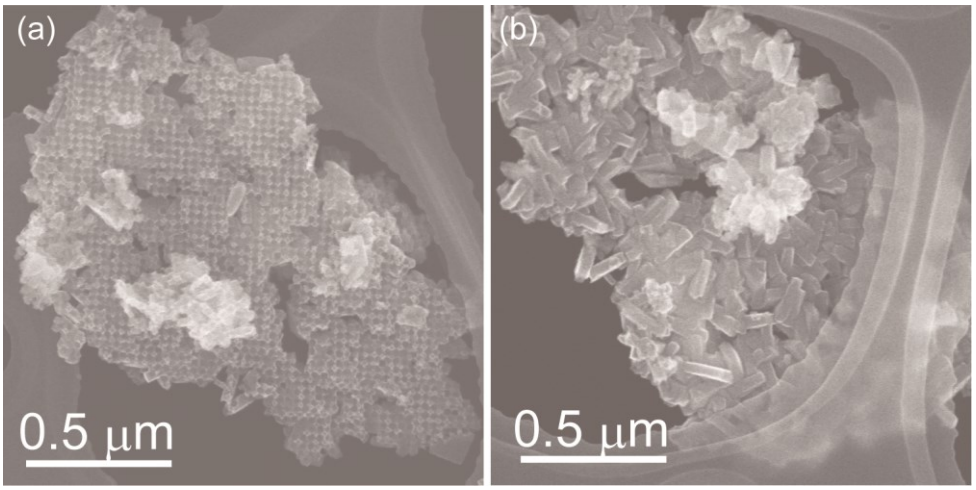

Figure 2.14 SEM images of Nb(7.4)-TiO_2; low-magnified image of (a) the dimpled particles shown in Figure 2.7d and (b) the opposite surface of the particles.

The addition of Nb led to the faster nucleation and crystal growth of TiO_2 than those without Nb, resulting in the deposition of TiO_2 prior to the infiltration of Ti

species into the inside of template. The crystallite size of rutile phase became smaller with the increase in the amount of Nb (Figure 2.9). Furthermore, the anatase phase formed by adding Nb was polycrystalline, which means that the crystallite size of anatase phase is smaller than that of rutile phase. These data suggest that the addition of Nb led to the faster nucleation and crystal growth.

The influence of Nb-doping into TiO_2 on the variation of both crystalline phase and mesostructure has been confirmed in this study. The size of silica nanoparticles forming a silica colloidal crystal template must be quite important to govern the preference of infiltration of precursor solutions. The preparation of highly ordered mesoporous Nb-doped TiO_2 with single-crystalline frameworks prepared in this study should contribute to both deeper understanding of controlled preparation of mesoporous transition metal oxides and various applications as electronically functional materials by tuning the electronic states.

2.4 Conclusion

This chapter showed the preparation of highly ordered mesoporous Nb-doped TiO_2 with single-crystalline frameworks using Ti-containing silica colloidal crystals as a template. The regularity of mesopores was much higher than that of single-crystalline mesoporous TiO_2 reported previously. This high regularity is attributed to the use of the silica nanoparticles assembly with ordered arrangement as a template. This work provides the method and chemistry for the design of mesoporous materials that should be promising for use in various potential applications. The addition of the Nb precursor into this reaction system unexpectedly induces the formation of very unique dimpled structures. This finding provides the preparative methods for not only mesoporous

materials but also plate-like Nb-doped TiO_2 with ordered mesoscale dimples from silica colloidal crystals.

2.5 References

1) a) T. Yanagisawa, T. Shimizu, K. Kuroda, C. Kato, *Bull. Chem. Soc. Jpn.* **1990**, 63, 988; b) J. S. Beck, J. C. Vartuli, W. J. Roth, M. E. Leonowicz, C. T. Kresge, K. D. Schmitt, C. T. W. Chu, D. H. Olson, E. W. Sheppard, S. B. McCullen, J. B. Higgins, J. L. Schlenker, *J. Am. Chem. Soc.* **1992**, 114, 10834; c) C. T. Kresge, M. E. Leonowicz, W. J. Roth, J. C. Vartuli, J. S. Beck, *Nature* **1992**, 359, 710.

2) a) R. Zhang, A. A. Elzatahry, S. S. Al-Deyab, D. Zhao, *Nano Today* **2012**, 7, 344; b) W. Zhou, H. Fu, *ChemCatChem* **2013**, 5, 885; c) W. Li, Z. Wu, J. Wang, A. A. Elzatahry, D. Zhao, *Chem. Mater.* **2014**, 26, 287.

3) a) X. Zheng, Q. Kuang, K. Yan, Y. Qiu, J. Qiu, S. Yang, *ACS Appl. Mater. Interfaces* **2013**, 5, 11249; b) E. J. W. Crossland, N. Noel, V. Sivaram, T. Leijtens, J. A. Alexander-Webber, H. J. Snaith, *Nature* **2013**, 495, 215; c) W. Jiao, Y. Xie, R. Chen, C. Zhen, G. Liu, X. Ma, H. M. Cheng, *Chem. Commun.* **2013**, 49, 11770.

4) a) D. M. Antonelli, J. Y. Ying, *Angew. Chem. Int. Ed. Engl.* **1995**, 34, 2014; *Angew. Chem.* **1995**, 107, 2202; b) D. M. Antonelli, *Microporous Mesoporous Mater.* **1999**, 30, 315; c) H. S. Yun, K. Miyazawa, H. Zhou, I. Honma, M. Kuwabara, *Adv. Mater.* **2001**, 13, 1377; d) D. Grosso, G. J. A. A. De Soler-Illia, F. Babonneau, C. Sanchez, P. A. Albouy, A. Brunet-Bruneau, A. R. Balkenende, *Adv. Mater.* **2001**, 13, 1085; e) B. Tian, H. Yang, X. Liu, S. Xie, C. Yu, J. Fan, B. Tu, D. Zhao, *Chem. Commun.* **2002**, 1824; f) P. C. A. Alberius, K. L. Frindell, R. C. Hayward, E. J. Kramer, G. D. Stucky, B. F. Chmelka, *Chem. Mater.* **2002**, 14, 3284; g) B. Smarsly, D. Grosso, T. Brezesinski, N.

Pinna, C. BoissiÀre, M. Antonietti, C. Sanchez, *Chem. Mater.* **2004**, 16, 2948; h) J. Lee, M. C. Orilall, S. C. Warren, M. Kamperman, F. J. Disalvo, U. Wiesner, *Nat. Mater*. **2008**, 7, 222; i) Y. Liu, J. M. Szeifert, J. M. Feckl, B. Mandlmeier, J. Rathousky, O. Hayden, D. Fattakhova-Rohlfing, T. Bein, *ACS Nano* **2010**, 4, 5373; j) J. M. Szeifert, J. M. Feckl, D. Fattakhova-Rohlfing, Y. Liu, V. Kalousek, J. Rathousky, T. Bein, *J. Am. Chem. Soc.***2010**, 132, 12605; k) J. Zhang, Y. Deng, D. Gu, S. Wang, L. She, R. Che, Z. S. Wang, B. Tu, S. Xie, D. Zhao, *Adv. Energy Mater.* **2011**, 1, 241.

5) a) W. Yue, X. Xu, J. T. S. Irvine, P. S. Attidekou, C. Liu, H. He, D. Zhao, W. Zhou, *Chem. Mater.* **2009**, 21, 2540; b) W. Yue, C. Random, P. S. Attidekou, Z. Su, J. T. S. Irvine, W. Zhou, *Adv. Funct. Mater.* **2009**, 19, 2826; c) J. Xu, B. Yang, M. Wu, Z. Fu, Y. Lv, Y. Zhao, *J. Phys. Chem. C* **2010**, 114, 15251; d) Z. Zhang, F. Zuo, P. Feng, *J. Mater. Chem.* **2010**, 20, 2206.

6) The use of crystalline TiO_2 nanoparticles as Ti source instead of a molecular precursor is a smart strategy to control the crystallite size, crystal structure, and dopant concentration because both complicated sol–gel processes and calcination can be avoided. However, the resultant mesoporous TiO_2 show much lower surface area and structural ordering if compared with that prepared by using a molecular precursor. See Ref. 4i,j.

7) X. Chen, S. S. Mao, *Chem. Rev.* **2007**, 107, 2891.

8) R. Watanabe, T. Yokoi, E. Kobayashi, Y. Otsuka, A. Shimojima, T. Okubo, T. Tatsumi, *J. Colloid Interface Sci.* **2011**, 360, 1.

9) a) Y. Furubayashi, T. Hitosugi, Y. Yamamoto, K. Inaba, G. Kinoda, Y. Hirose, T. Shimada, T. Hasegawa, *Appl. Phys. Lett.* **2005**, 86, 252101; b) X. Lì, X. Mou, J. Wu, D. Zhang, L. Zhang, F. Huang, F. Xu, S. Huang, *Adv. Funct. Mater.* **2010**, 20, 509; c) C.

Das, P. Roy, M. Yang, H. Jha, P. Schmuki, *Nanoscale* **2011**, 3, 3094; d) M. Fehse, S. Cavaliere, P. E. Lippens, I. Savych, A. Iadecola, L. Monconduit, D. J. Jones, J. RoziÀre, F. Fischer, C. Tessier, L. Stievano, *J. Phys. Chem. C* **2013**, 117, 13827; e) X. Lì, W. Yang, Z. Quan, T. Lin, L. Bai, L. Wang, F. Huang, Y. Zhao, *J. Am. Chem. Soc.* **2014**, 136, 419.

10) a) D. A. H. Hanaor, C. C. Sorrell, *J. Mater. Sci.* **2011**, 46, 855; b) R. M. Pittman, A. T. Bell, *J. Phys. Chem.* **1993**, 97, 12178; c) A. M. Ruiz, G. Dezanneau, J. Arbiol, A. Cornet, J. R. Morante, *Chem. Mater.* **2004**, 16, 862.

11) J. Su, X. X. Zou, Y. C. Zou, G. D. Li, P. P. Wang, J. S. Chen, *Inorg. Chem.* **2013**, 52, 5924.

12) a) K. Yanagisawa, J. Ovenstone, *J. Phys. Chem. B* **1999**, 103, 7781; b) H. Cheng, J. Ma, Z. Zhao, L. Qi, *Chem. Mater.* **1995**, 7, 663.

13) A. Stein, B. E. Wilson, S. G. Rudisill, *Chem. Soc. Rev.* **2013**, 42, 2763.

14) a) Y. Kuroda, K. Kuroda, *Angew. Chem. Int. Ed.* **2010**, 49, 6993; *Angew. Chem.* **2010**, 122, 7147; b) Y. Kuroda, Y. Sakamoto, K. Kuroda, *J. Am. Chem. Soc.* **2012**, 134, 8684.

15) K. M. Choi, K. Kuroda, *Chem. Commun.* **2011**, 47, 10933.

Chapter 3

Use of Titanium Oxide Modified Mesoporous Silica as a Template for Preparation of Mesoporous Carbon Incorporating TiO_2 Nanocrystals

Chapter 3

3.1 Introduction

Ordered mesoporous carbon has been intensively studied for various potential applications, such as supercapacitors, Li-ion batteries, and adsorbents, because of its high surface area, large pore volume, uniform mesopores, chemical inertness, mechanical stabilities, and electrical conductivity.[1] Because of these characteristics, mesoporous carbon has also been used as a support to accommodate metal oxide nanoparticles.[2] In fact, there have been some reports on such nanocomposites in various metal oxides so far.[2] However, there still remains a challenge in the preparation of the nanocomposites with high loading amount of metal oxides, although the loading amount is the most influential on the properties of the nanocomposites.[2a]

The nanocomposites are prepared by the following three steps: 1) preparation of mesoporous carbon using hard- or soft-templating methods, 2) infiltration of a metal oxide precursor into the prepared mesoporous carbon, 3) heat treatment of the metal oxide precursor incorporated mesoporous carbon under inert gas flow. When the amount of the introduced precursor is relatively small, dispersed metal oxide nanoparticles can be obtained within the mesopores.[2] However, the increase in the amount of the precursor undesirably induces the formation of bulk particles on the outer surface of mesoporous carbon, which is mainly due to the weak interaction between the carbon and metal oxides.[3] The introduction of oxygen containing functional groups into the surface of carbon frameworks using oxidizing reagents, such as hydrogen peroxide and nitric acid, has been used to vary the interactions between carbon and metal oxides.[4] However, such a functionalization process often induces the deterioration of mesostructures of carbon frameworks due to the harsh conditions of the introduction of oxygen containing functional groups, and the amount of the introduced functional

groups is limited.[3] Therefore, unconventional approach is required for the preparation of metal oxide nanoparticles incorporated mesoporous carbon with the controlled loading amount.

Co-addition of precursors of carbon and metal oxides into a hard template such as mesoporous silica is beneficial to avoid the formation of the bulk particles.[5] Metal oxide nanoparticles are simultaneously formed along with carbon frameworks within the template during the heat treatment. The formation of bulk particles are avoided owing to both the strong interaction between the silica template and metal oxides and doubly confinement by frameworks of silica and carbon.[3] However, the formed nanoparticles were reported to be encapsulated within the carbon frameworks, meaning that the surfaces of the nanoparticles were not effectively used.[5b,5c]

Herein, I have demonstrated that the use of metal oxide modified mesoporous silica SBA-15[6] as a template is quite effective for the successful preparation of metal oxide nanoparticles incorporated mesoporous carbon with high loading amount. In this study, titanium oxide was chosen as an example to demonstrate the usefulness of the preparative approach reported here because a combination of carbon and titanium oxides is one of the most common combinations due to the potential application for Li-ion batteries.[7] Titanium oxides are modified on the surface of mesoporous silica by using a surface sol-gel technique,[8] and subsequently carbon was deposited within the template. The formation of the bulk particles during the heat treatment for carbonization and crystallization of titanium oxide can be avoided because titanium oxide was immobilized on the surface of mesoporous silica template. In addition, the encapsulation should also be avoided because the formation of TiO_2 nanocrystals occurs in the interstices between the frameworks of the silica template and carbon frameworks

owing to the immobilization of titanium oxide on the surface of mesoporous silica. This is in contrast to the previous reports on the use of simultaneous addition of precursors of metal oxide and carbon into the template for the preparation of such complex systems.

3.2 Experimental

3.2.1 Materials

Tetraethoxysilane (TEOS, Kishida Chemical Co.), triblock copolymer $EO_{20}PO_{70}EO_{20}$ (Pluronic 123, Aldrich Co.), hydrochloric acid (35–37 wt%, Wako Pure Chemical Industries Ltd.) were used for preparation of SBA-15. Titanium tetraisopropoxide (TTIP, Wako Pure Chemical Industries Ltd.) was used as a Ti source. Anhydrous toluene (Wako Pure Chemical Industries Ltd.) was used as a solvent for modification of titanium oxide on the surface of SBA-15. 2,3-Dihydroxynaphthalene (Tokyo Chemical Industry Co., Ltd.) and acetone (Wako Pure Chemical Industries Ltd.) were used as a carbon source and solvent for the incorporation of the carbon source into the template, respectively. Sodium hydroxide was used for removal of the silica template.

3.2.2 Modification of titanium oxide on the surface of SBA-15

SBA-15 type mesoporous silica was hydrothermally synthesized at 130 °C according to a literature.[6] After drying SBA-15 (0.6 g) at 120 °C for 3 h, the dried SBA-15 was dispersed in toluene (20 mL), and then TTIP (1.9 mL, 6.5 mmol) was added to the mixture. The mixture was refluxed at 110 °C for 3 h under N_2 flow. Then, the mixture was filtered under N_2 atmosphere. The obtained powder was washed with toluene and hexane, and then dried under reduced pressure. Then, deionized water (200

mL) was added to the powder, and the aqueous mixture was stirred at room temperature for 1 h to hydrolyze the unreacted alkoxy groups of the grafted alkoxide. The formation of hydroxyl groups is required for the subsequent carbon deposition.[9] The powder was recovered by filtration, and dried at 60 °C for 30 min in an oven. The obtained sample was denoted as Ti-SBA-15.

3.2.3 Preparation of mesoporous C/TiO_2 nanocomposites

2,3-Dihydroxynaphthalene was chosen as a carbon source because it does not require acid catalysts, which are reactive with titanium oxides, for its carbonization.[9] The prepared Ti-SBA-15 (0.10 g) was dried at 120 °C for 3 h. Then, 2,3-dihydroxynaphthalene (4.3 g, 27 mmol) was dissolved in acetone (2.0 mL), and the solution was added to the dried Ti-SBA-15. The mixture was placed under reduced pressure to incorporate the carbon source into mesopores of Ti-SBA-15 by a capillary force until the powder became dry. The obtained powder was calcined at 300 °C for 2 h under Ar flow for the dehydration reaction between silanol groups of the surface of the template and hydroxyl groups of the carbon source.[9] The calcined powder was washed with acetone to remove the free carbon source,[9] and then calcined at 900 °C for 5 h under Ar flow. Finally, mesoporous C/TiO_2 was obtained after removal of the silica template with 2 M NaOH aq. The obtained sample was denoted as mp-C/TiO_2 (mp: mesoporous).

3.2.4 Characterization

Transmission electron microscopy (TEM) images and energy dispersive X-ray (EDX) spectra of SBA-15 and Ti-SBA-15 were taken by a JEOL JEM-2010 microscope

using an accelerating voltage of 200 kV. TEM images and high-resolution TEM (HRTEM) image of mp-C/TiO_2 were conducted on a JEOL JEM-2100F microscope using an accelerating voltage of 200 kV. Samples for TEM and EDX measurements were dispersed in ethanol, and the solutions were dropped on a carbon-coated microgrid (Okenshoji. Co). X-ray diffraction (XRD) patterns at small diffraction angles were recorded with a Rigaku NANO-Viewer using CuKα radiation under the operating conditions of 40 kV and 30 mA and a Pilatus 2D X-ray detector (Dectris). N_2 adsorption-desorption isotherms were measured with a BELSORP-max (MicrotracBEL Co.) at –196 °C. Prior to the N_2 adsorption-desorption measurement, samples were heated at 120 °C under reduced pressure. The pore size was determined by using adsorption data. High-angle XRD patterns were recorded with a Rigaku RINT-Ultima III diffractometer using Ni-filtered CuKα radiation under the operating conditions of 40 kV and 40 mA and a high-speed 1D X-ray detector (D/teX Ultra). Inductively coupled plasma optical emission spectroscopy (ICP-OES) analysis was conducted on a Thermo Scientific iCAP 6500 Duo-ICP-OES. TGA measurement was conducted on a Rigaku Thermo plus EVO2/TG-DTA8121 instrument.

3.3 Results and discussion

3.3.1 Modification of titanium oxide on the surface of SBA-15

The Ti/Si ratio of Ti-SBA-15 was calculated to be 0.24 from the ICP-OES measurements. The N_2 adsorption-desorption isotherms of SBA-15 and Ti-SBA-15 were typical type IV (Figure 3.1A). The hysteresis loop in the N_2 adsorption-desorption isotherm slightly shifted to lower relative pressure after the modification, and accordingly the pore size calculated by using non-local density functional theory

(NLDFT) method was reduced (Figure 3.1B). The reduction in the pore sizes indicates the formation of the titanium oxide layers on the surface of SBA-15.

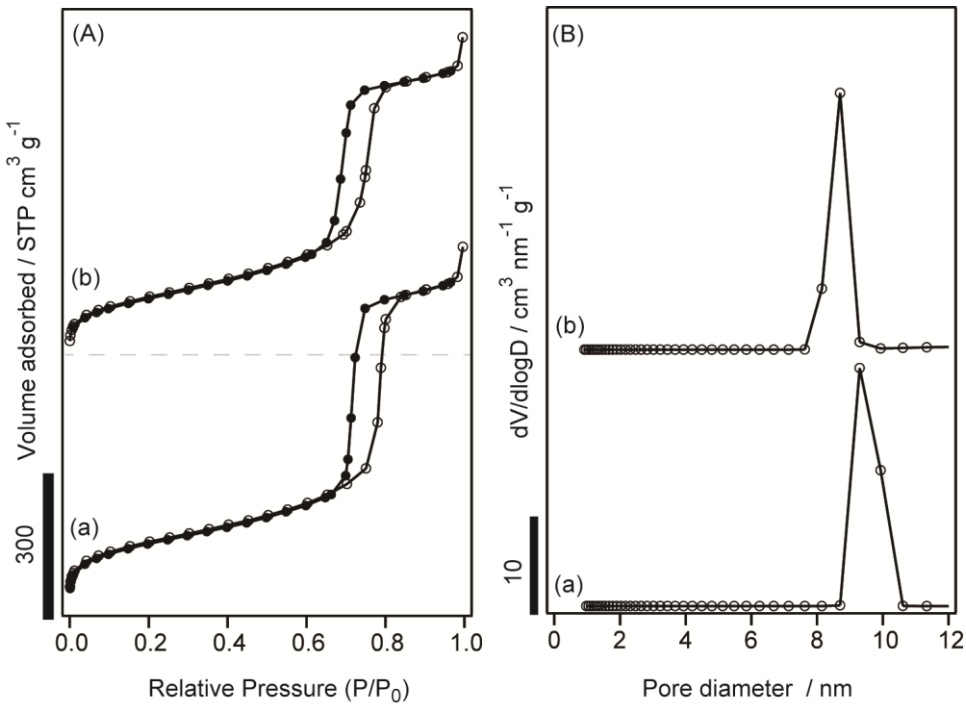

Figure 3.1 (A) N_2 adsorption-desorption isotherms and (B) NLDFT pore size distributions of (a) SBA-15 and (b) Ti-SBA-15.

The small-angle XRD patterns showed that the prepared SBA-15 possessed an ordered 2D hexagonal mesostructure, and the mesostructure was retained after the modification of titanium oxide (Figure 3.2).

It is reasonable that the peaks of Ti-SBA-15 did not shift from the original positions because the size of periodicity should not be varied by the surface modification. The textural properties of SBA-15 and Ti-SBA-15 calculated from the N_2 adsorption-desorption isotherms and the small-angle XRD patterns are shown in Table 3.1. The decrease in the pore volume and BET surface area also supports the surface modification with titanium oxide.

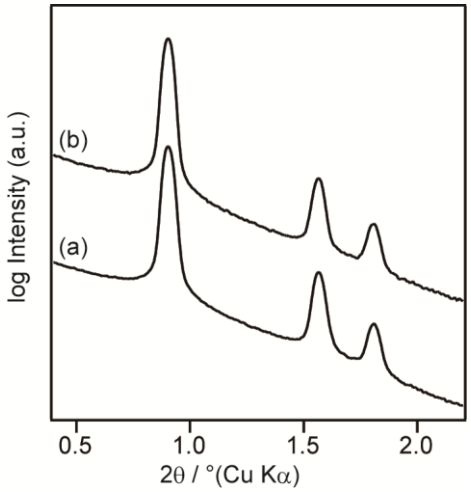

Figure 3.2 Small-angle XRD patterns of (a) SBA-15 and (b) Ti-SBA-15.

Table 3.1 Textural properties of SBA-15 and Ti-SBA-15.

Sample Name	Unit cell parameter [nm]	BET surface area [m^2 g^{-1}]	Pore volume [cm^3 g^{-1}]	NLDFT pore size [nm]	Wall thickness [nm]
SBA-15	11.3	489	1.1	9.3	2.0
Ti-SBA-15	11.3	475	0.98	8.7	2.6

The XRD patterns of SBA-15 and Ti-SBA-15 showed only broad peaks due to the amorphous silica template. This shows that anatase TiO_2 was not formed by non-hydrolytic condensation between TTIP[10] in the reaction conditions used in this study.

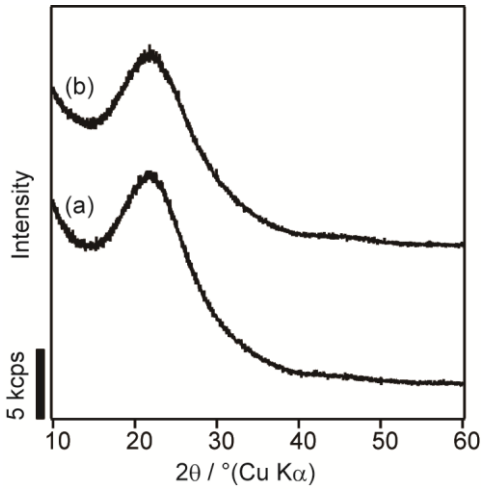

Figure 3.3 XRD patterns of (a) SBA-15 and (b) Ti-SBA-15.

TEM images of Ti-SBA-15 (Figure 3.4) also supported the retention of the mesostructured, as characterized by small-angle XRD patterns. The EDX spectra showed the presence of Ti species in each SBA-15 particle (Figure 3.4).

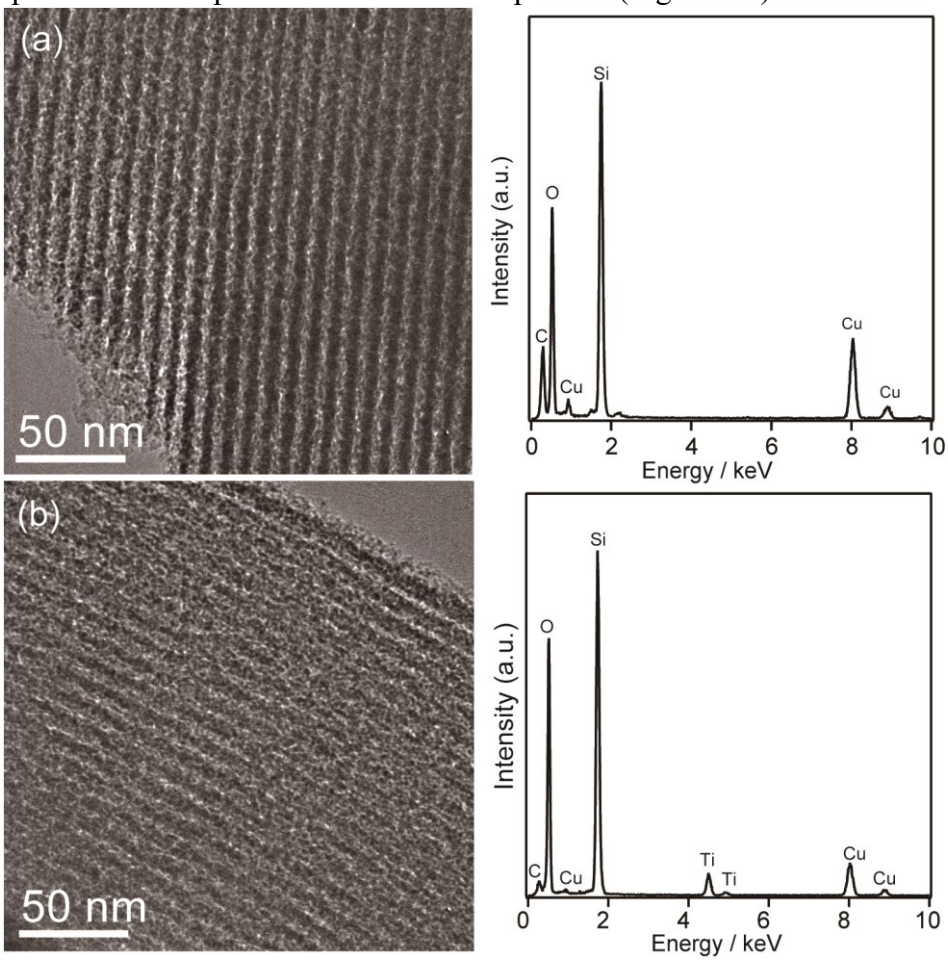

Figure 3.4 TEM images (left) and corresponding EDX spectra (right) of (a) SBA-15 and (b) Ti-SBA-15.

The formation of bulk particles by the outer deposition was not observed. These data described above indicate the successful modification of titanium oxide. It should be noted that the prevention of the formation of bulk titanium oxide particles is successful because N_2 atmosphere was used throughout the reaction between surface OH groups and TTIP and the following filtration to remove unreacted TTIP after the reaction. In fact, when the filtration was performed under air atmosphere as reported previously,[8] the

bulk particles were formed due to the hydrolysis and condensation of the unreacted TTIP (Figure 3.5).

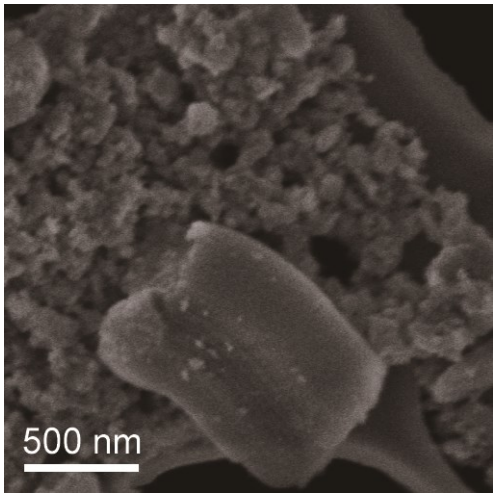

Figure 3.5 SEM image of Ti-SBA-15 prepared by the filtration under air atmosphere.

3.3.2 Preparation of mesoporous C/TiO_2 using Ti-SBA-15 as a template

The weight fraction of carbon in mp-C/TiO_2 was calculated from the TGA curve (Figure 3.6). The weight loss of *ca.* 10 wt% between room temperature to 280 °C is mainly due to elimination of adsorbed water. The major decrease in the weight around 400 °C is due to the combustion of carbon. From the TGA curves, the weight fraction of carbon content of mp-C/TiO_2 calculated from the weight loss is *ca.* 69 wt%. Therefore, the weight fraction of TiO_2 of mp-C/TiO_2 was roughly estimated as 31 wt%.

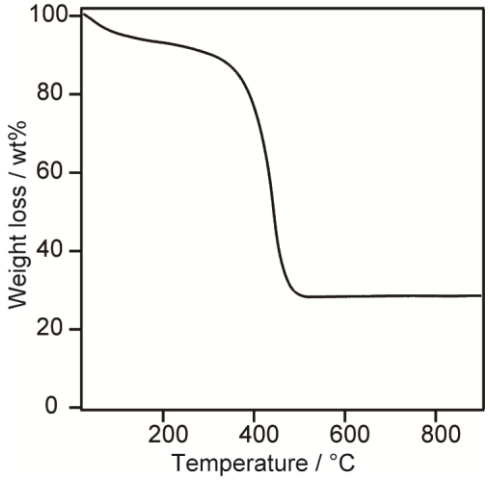

Figure 3.6 TGA curve of mp-C/TiO_2.

The XRD pattern showed the three broad peaks at around 25°, 42° and 48°, respectively (Figure 3.7). The broad peaks at 25° and 48° are due to amorphous carbon frameworks. The peak at 48° can be assigned to anatase TiO_2. The broad peak suggested the formation of small anatase TiO_2 nanocrystals without the accompanying formation of bulk TiO_2 nanoparticles.

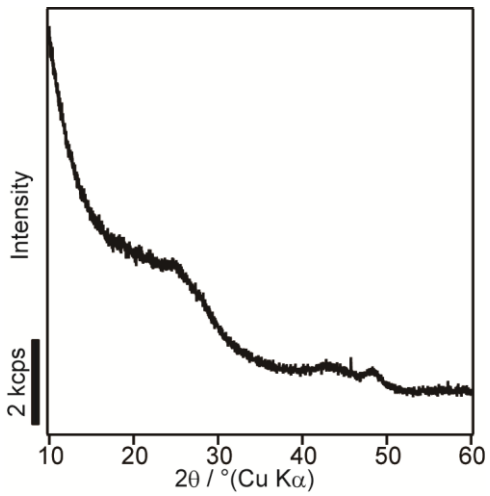

Figure 3.7 XRD pattern of mp-C/TiO_2.

The ordered mesostructure replicated form the template was clearly observed in the TEM images of mp-C/TiO_2 (Figure 3.8).

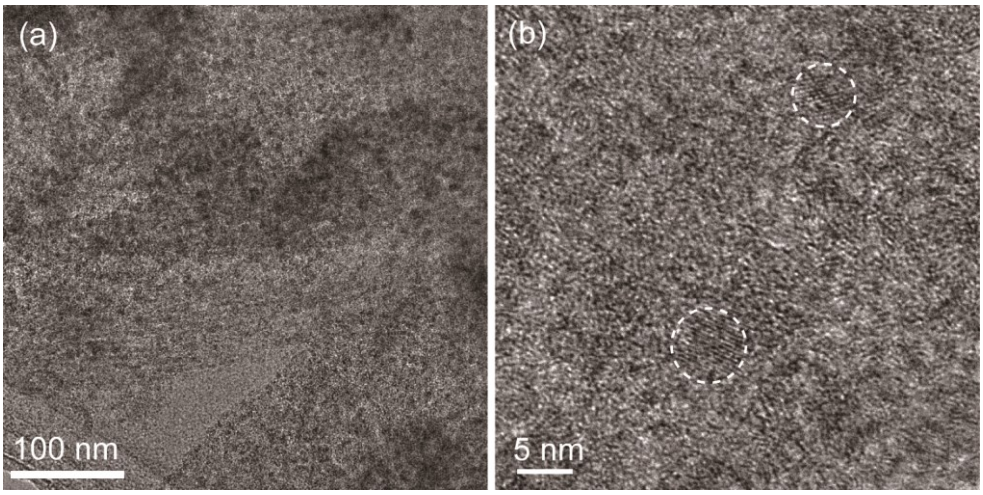

Figure 3.8 (a) TEM and (b) HRTEM images of mp-C/TiO_2. Dotted circles indicate the lattice fringes of the formed TiO_2 nanocrystals.

The peaks observed in the small-angle XRD pattern of mp-C/TiO_2 support the successful replication of the template. The peak positions were slightly shifted to lower angles, which is due to the shrinkage of the frameworks during the high temperature heat treatment. The peak intensities became smaller if compared with those of the original template, meaning that the regularity of the mesostructure was reduced. These are common phenomena for the hard-templating synthesis of mesoporous carbon.[1] In the TEM image, the small black spots were observed, which was due to the formed TiO_2 nanocrystals. In fact, lattice fringes due to anatase TiO_2 were observed as indicated by the two dotted circles in the HRTEM image (Figure 3.11b). Both of the crystallite sizes are estimated to be *ca.* 3 nm and 5 nm, respectively, which is well consistent with the broad peak in the XRD pattern (Figure 3.7). In addition, bulk particles were not observed. These TEM images are the strong and direct evidence for the formation of small TiO_2 nanocrystals without accompanying the formation of bulk particles. The

formation of small crystallites is due to the suppression of the crystal growth by both the silica frameworks of the template and the simultaneously formed carbon frameworks. In addition, the covalent bonds between titanium oxide layer and the template are also crucial. The migration of Ti species within the template during the carbonization was suppressed due to the covalent bonds, resulting in the formation of small crystallite sizes.

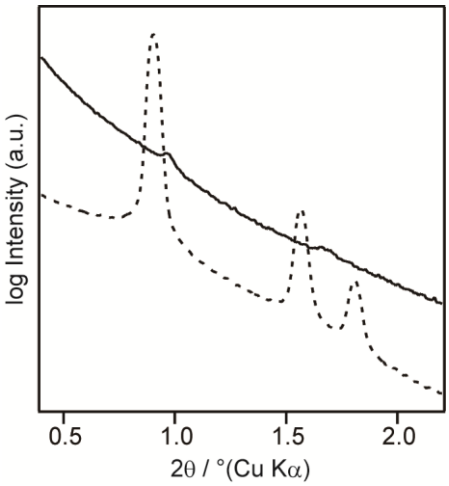

Figure 3.9 Small-angle XRD patterns. Solid line: mp-C/TiO_2; dotted line: SBA-15 (reprint of Figure 3.2a)

The N_2 adsorption-desorption isotherm of mp-C/TiO_2 was type IV with hysteresis loop, indicating the successful formation of mesoporous structure (Figure 3.10A). Because the calculation using NLDFT method was not fitted well, Barrett–Joyner–Halenda method was applied for the calculation of the pore size distribution, although the method assuming a cynlindrical pore shape is not suited the materials reported here. The BJH pore size of mp-C/TiO_2 was *ca.* 3.3 nm in diameter (Figure 3.10B). The pore size is in good agreement with the wall thickness of SBA-15, suggesting that the mesoporous structure was formed by replicating the template. The textural properties of mp-C/TiO_2

calculated from the small-angle XRD pattern and N_2 adsorption-desorption isotherm are summarized in Table 3.2.

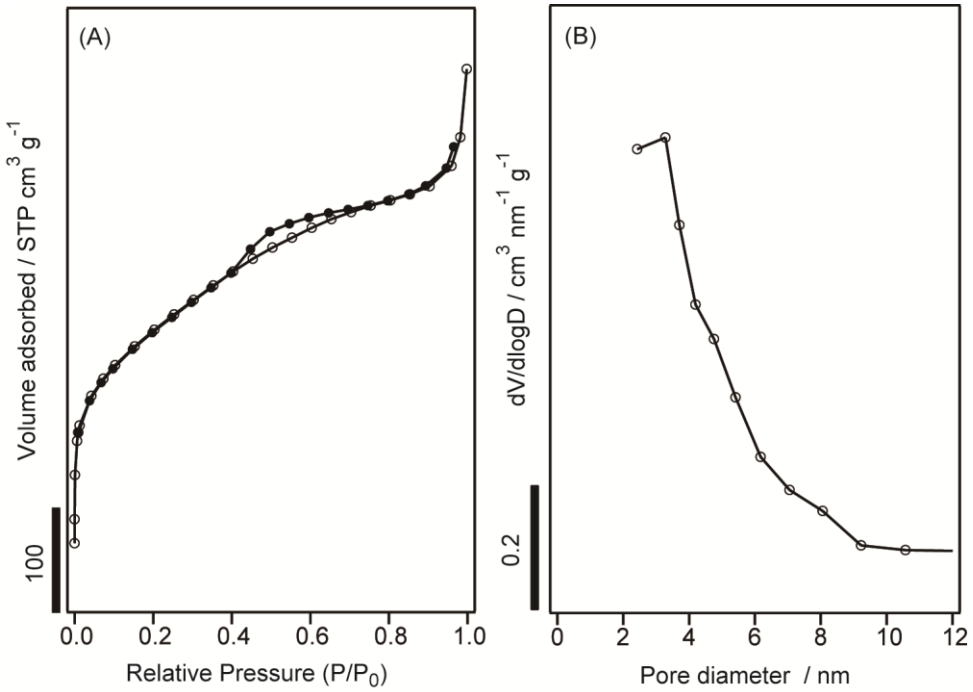

Figure 3.10 (A) N_2 adsorption-desorption isotherm and (B) BJH pore size distribution of mp-C/TiO_2.

Table 3.2 Textural properties of mp-C/TiO_2.

Sample Name	Unit cell parameter [nm]	BET surface area [m^2 g^{-1}]	Pore volume [cm^3 g^{-1}]	BJH pore size [nm]	Wall thickness [nm]
mp-C/TiO_2	10.5	993	0.79	3.3	7.2

The uniqueness of this study is the use of titanium oxide modified mesoporous silica as a template for the preparation of mesoporous C/TiO_2 nanocomposite. Although there have been some reports on the use of mesoporous silica with surface oxide such as aluminum oxide as a template for preparation of mesoporous carbon, the preparation of

the mesoporous nanocomposite has not been achieved. Because the covalent bonds between the oxide layer and the surface of the template suppress the migration of Ti species during the crystallization, small TiO_2 nanocrystals tend to form within the template. The control of loading amount of TiO_2 on mesoporous carbon retaining small crystallite sizes is expected to be achieved by increase in the thickness of the oxide layer.

3.4 Conclusion

We have demonstrated the usefulness of titanium oxide modified mesoporous silica as a template for the preparation of mesoporous C/TiO_2 nanocomposites. The crystallization of the surface titanium oxide layer and the formation of carbon frameworks occurred simultaneously during the heat treatment. The formation of anatase TiO_2 with small crystallite sizes was due to the confinement effects by the rigid frameworks of silica and carbon and the suppression of the migration by the covalent bonds between the surface oxide layer and the surface of the template. In addition, the encapsulation was avoided because the formation of TiO_2 nanocrystals occurred in the interstices between the frameworks of the silica template and carbon frameworks owing to the immobilization of titanium oxides on the surface of mesoporous silica. The unique preparative route reported here should be applicable to other composition, which enables further design of nanocomposite materials.

3.5 Reference

1) a) C. Liang, Z. Li, S. Dai, *Angew. Chem. Int. Ed.* **2008**, 47, 3696; b) H. Nishihara, T. Kyotani, *Adv. Mater.* **2012**, 24, 4473.

2) a) H. Jiang, J. Ma, C. Li, *Adv. Mater.* **2012**, 24, 4197; b) P. Zhang, H. Zhu, S. Dai, *ChemCatChem* **2015**, 7, 2788.

3) A. Stein, Z. Wang, M. A. Fierke, *Adv. Mater.* **2009**, 21, 265.

4) a) L. Zeng, C. Zheng, C. Deng, X. Ding, M. Wei, *ACS Appl. Mater. Interfaces* **2013**, 5, 2182; b) S. Zhu, H. Zhou, M. Hibino, I. Honma, M. Ichihara, *Adv. Funct. Mater.* **2005**, 15, 381.

5) a) Z. Li, N. Liu, X. Wang, C. Wang, Y. Qi, L. Yin, *J. Mater. Chem.* **2012**, 22, 16640; b) H. Li, H. Xi, S. Zhu, R. Wang, *Mater. Lett.* **2006**, 60, 943; c) H. Li, S. Zhu, H. Xi, R. Wang, *Microporous Mesoporous Mater.* **2006**, 89, 196.

6) A. Galarneau, H. Cambon, F. Di Renzo, R. Ryoo, M. Choi, F. Fajula, *New J. Chem.* **2003**, 27, 73.

7) a) Y. Ishii, Y. Kanamori, T. Kawashita, I. Mukhopadhyay, S. Kawasaki, *J. Phys. Chem. Solids* **2010**, 71, 511; b) R. Liu, Y. Ren, Y. Shi, F. Zhang, L. Zhang, B. Tu, D. Zhao, *Chem. Mater.* **2008**, 20, 1140; c) J. Ma, D. Xiang, Z. Li, Q. Li, X. Wang, L. Yin, *CrystEngComm* **2013**, 15, 6800.

8) W. Yan, B. Chen, S. M. Mahurin, E. W. Hagaman, S. Dai, S. H. Overbury, *J. Phys. Chem. B* **2004**, 108, 2793.

9) N. Gokulakrishnan, N. Kania, B. Léger, C. Lancelot, D. Grosso, E. Monflier, A. Ponchel, *Carbon* **2011**, 49, 1290.

10) N. Pinna, M. Niederberger, *Angew. Chem. Int. Ed.* **2008**, 47, 5292.

11) D. A. H. Hanaor, C. C. Sorrell, *J. Mater. Sci.* **2011**, 46, 855.

Chapter 4

Stepwise Deposition of Au and Pt within Mesoporous Silica SBA-15 for Preparation of Mesoporous Bimetallic Materials

Chapter 4

4.1 Introduction

Bimetallic nanocrystals are attractive for various applications because synergistic effects between the two kinds of metals provide novel properties that cannot be obtained from monometallic nanocrystals.[1] Bimetallic nanocrystals may be classified into three structural types according to the arrangements of the two metals: 1) alloyed (solid solution or intermetallic) structures,[1a-c] 2) core/shell structures,[1b-e] and 3) phase segregated heterostructures.[1b,1d-f] Because the properties of bimetallic nanocrystals strongly depend on their structures, structural control is essential to tune their physicochemical properties..[2] To date, numerous studies have been reported on structural control in various combinations of metals.[1] However, bimetallic nanocrystals tend to form aggregates due to their high surface energy, resulting in less effective use of their surfaces,[1d,3] except for the mesoporous bimetallic structures described in the next paragraph. Although capping agents, such as thiol and amine molecules, can prevent the formation of aggregates, the properties of the surfaces are undesirably influenced by such agents.

Mesoporous bimetallic materials are expected to be promising candidates because their surfaces can be effectively used owing to their large inner surface areas free from capping agents.[4] There have been several reports on the preparation of mesoporous bimetallic nanostructures with alloyed[5] or core/shell structures.[6] Although mesoporous bimetallic films composed of interstratified layers of mesoporous Pt and Pd have been reported,[4e] mesoporous bimetallic materials with a nanoscale phase-segregated structure, which is generally accepted as a phase-segregated nanostructure,[1b,1d-f] have not been achieved despite the usefulness of the bimetallic structures as unique catalysts.[7] Nanoscale phase segregation is advantageous, compared

with previously reported materials,[4e] from the viewpoint of density of heterojunctions between the two constituent metals, which is essential to obtain the associated unique properties. Therefore, an unconventional approach is required for further development of this field.

Among several approaches for the preparation of mesoporous metallic materials,[4f] the use of mesoporous silica should be very promising for the preparation of bimetals with phase-segregated heterostructures because silica can effectively serve as both a support[8] and a template.[4d,f,9] Therefore, we envisaged that monometallic nanocrystals might be supported on mesoporous silica[8] and that they can be used as seed metals to form heterojunctions via a seed-growth method. Furthermore, the anisotropic growth of the second metal from preformed nanocrystals supported on the mesopores can be achieved irrespective of various synthetic factors (e.g. size, shape, and facets of seed metals, combination of two metals, etc.) owing to the anisotropic shapes of mesopores and rigid frameworks.[1d,4b,f] Although the usefulness of mesoporous silica as both a support and template has been demonstrated in many studies,[4d,f,8-9] the preparation of mesoporous bimetallic materials with phase-segregated heterostructures has yet to be achieved.

This chapter describes stepwise deposition of Au and Pt within two-dimensional mesoporous silica SBA-15[10] for preparation of mesoporous bimetallic Au-Pt with a phase segregated structure. This chapter consists of two sections (Section 4.2 and 4.3). Section 4.2 describes the preparation of controlled nanostructured Au within mesopores. Au nanorods replicated from cylindrical mesopores of SBA-15 and Au nanoparticles were selectively prepared by performing Au deposition under the absence or presence of hexadecyltrimethylammonium bromide (C_{16}TMAB). Section 4.3

describes the preparation of bimetallic Au-Pt with a phase segregated structure by stepwise deposition of Au and Pt. Au nanoparticles were prepared within the mesopores of SBA-15 by using the deposition method described in section 4.2, and then Pt was deposited to form heterojunction between the two metals.

4.2 Preparation of highly controlled nanostructured Au within mesopores using reductive deposition in non-polar environments

This section describes the deposition of Au exclusively inside mesoporous silica by a liquid phase deposition process using a non-polar solvent and unique reducing agent (Scheme 4.1). The method reported here has several advantages, including ease of scale-up, energy consumption, and simple synthetic equipments. Although liquid-phase deposition is an ideal process because of these advantages, this method has not been suited to the templating method because Au precursors incorporated into the template tend to migrate outside the template owing to their dissolution into solvents containing reducing agents. Therefore, we have conceived a protocol employing a reducing agent/solvent combination, both of which have low affinity with the Au precursor, to enable Au deposition inside mesoporous silica. In this section, Au is exclusively deposited inside SBA-15[10] without outside deposition by using hexane and 1,1,3,3-tetramethyldisiloxane. In addition, we have succeeded in separately preparing Au nanorods without simultaneous addition of surfactants and Au nanoparticles using C_{16}TMAB as a surfactant. Because the properties of nanostructured Au are greatly influenced by their morphology and size, the utility of the method reported here becomes apparent since nanoparticles and nanorods can be selectively prepared by simply performing deposition in the presence or absence of the surfactants.

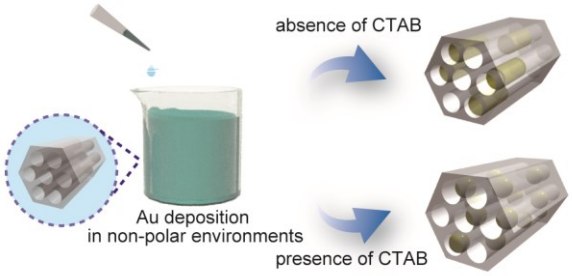

Scheme 4.1 Preparation of controlled nanostructured Au within mesopores

4.2.1 Experimental

4.2.1.1 Materials

Tetraethoxysilane (TEOS, Tokyo Chemical Industry Co., Ltd.), triblock copolymer $EO_{20}PO_{70}EO_{20}$ (Pluronic 123, Aldrich Co.), and hydrochloric acid (35–37 wt%, Wako Pure Chemical Industries Ltd.) were used for the preparation of SBA-15. $HAuCl_4 \cdot 4H_2O$ (Kanto Chemical Co., Inc.) was used as a Au precursor. Anhydrous ethanol (Wako Pure Chemical Industries Ltd.) was used as a solvent for incorporation of the Au precursor. Hexane (Wako Pure Chemical Industries Ltd.) and 1,1,3,3-tetramethyldisiloxane (TMDS, Tokyo Chemical Industry Co., Ltd.) were used as solvent and reducing agent, respectively. C_{16}TMAB (Wako Pure Chemical Industries Ltd.) was used as a capping agent to control the morphology of the nanostructured Au inside mesoporous silica.

4.2.1.2 Preparation of SBA-15

Mesoporous silica SBA-15 was hydrothermally synthesized at 100 °C according to a literature.[10] The temperature of the hydrothermal treatment in this section was different with that in Chapter 3. Therefore, the textural properties of SBA-15

prepared in section 4.2 are different with those of SBA-15 prepared in Chapter 3. The Synthesized SBA-15 had a highly ordered 2D hexagonal mesostructure, as determined by its X-ray diffraction (XRD) pattern (Figure 4.1). The unit cell parameter was calculated as 10.6 nm from the d_{10} spacing of the XRD pattern.

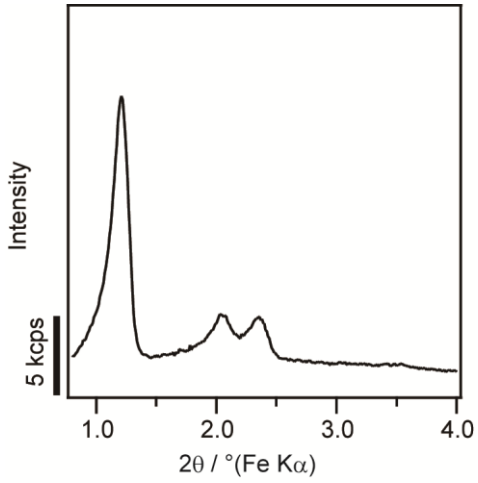

Figure 4.1 Low-angle XRD pattern of SBA-15.

Straight mesochannels were clearly observed in the transmission electron microscopy (TEM) image (Figure 4.2).

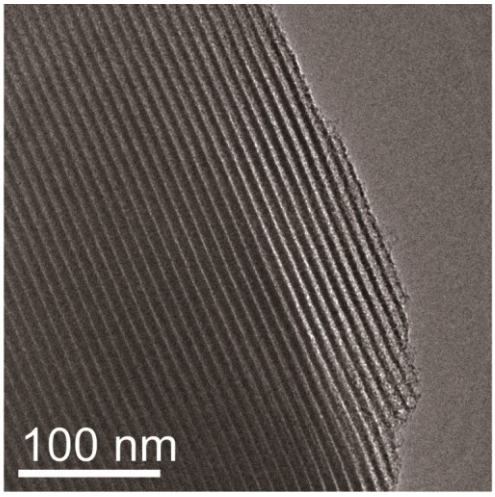

Figure 4.2 TEM image of SBA-15.

The N_2 adsorption desorption isotherm of SBA-15 was typical type IV (Figure 4.3A), which is characteristic of mesoporous materials. The pore size of SBA-15 as calculated by the Barrett–Joyner–Halenda (BJH) method was calculated as 8.1 nm (Figure 4.3B) and the pore volume was estimated as 1.2 cm^3g^{-1} from the volume of adsorbed N_2 at P/P_0 = *ca.* 0.99.

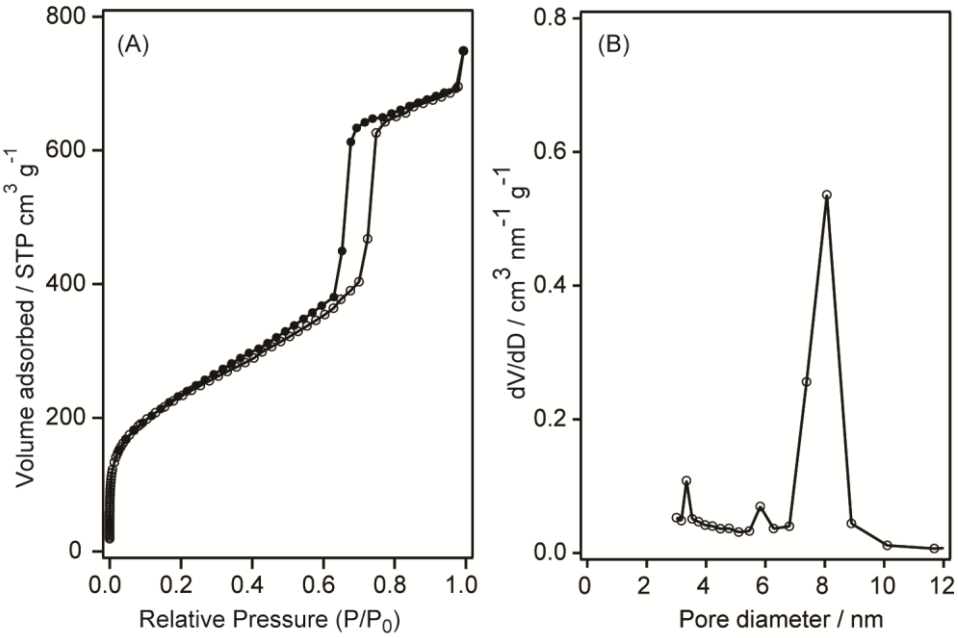

Figure 4.3 (A) N_2 adsorption-desorption isotherm of SBA-15 and (B) BJH pore size distribution of SBA-15.

4.2.1.3 Preparation of Au nanorods inside SBA-15

SBA-15 was dried under reduced pressure at 120 °C to remove adsorbed water. The dried SBA-15 (0.1 g) was then dispersed in anhydrous ethanol (10 mL). A stock solution of $HAuCl_4 \cdot 4H_2O$ in ethanol (12 mL, corresponding to 0.029 mmol of Au) was added to the solution containing SBA-15. The mixed solution was placed under reduced pressure to incorporate the Au precursor into the mesopores of SBA-15 by capillary forces; this process yielded a dried powder. The color of the Au-incorporated SBA-15

powder was yellow. After the powders were dispersed in hexane (5 mL), TMDS (103 m L, 0.58 mmol) was added to the hexane solution under stirring; the color of the powder was observed to change to black-purple within 1 min. After stirring for 1 h, the hexane solution was filtered. The obtained powders were washed with hexane and ethanol and dried at room temperature under an air atmosphere. The obtained product was denoted as SBA-15/Au.

4.2.1.4 Preparation of Au nanoparticles inside SBA-15 by adding C_{16}TMAB

The preparative procedure of Au nanoparticles inside SBA-15 was almost same except the addition of C_{16}TMAB before the reduction. Before the addition of TMDS, C_{16}TMAB (0.091 g, 0.25 mmol) was added into the solution. The color of the powders in the solution turned orange from yellow during stirring, which indicates the formation of a gold complex with C_{16}TMAB.[11] After stirring for 1 h, the reducing agent was added into the mixture. The color of the powders in the solution turned from orange to purple. After stirring for 1 h, the hexane solution was filtered. The obtained powders were washed with hexane and ethanol and dried at room temperature in air atmosphere. The obtained product was denoted as SBA-15/Au_C_{16}TMAB.

4.2.1.5 Characterization

TEM images, selected area electron diffraction (SAED) patterns, and energy dispersive X-ray (EDX) spectra were recorded on a JEOL JEM-2010 electron microscope (accelerating voltage of 200 kV). Samples were dispersed in ethanol and mounted on a STEM microgrid for TEM observations. High-angle XRD patterns were measured using a Rigaku RINT-Ultima III diffractometer with a high-speed X-ray

detector (D/teX Ultra; CuKα radiation of 40 kV, 40 mA). Low-angle XRD patterns were measured using a Rigaku Ultima IV diffractometer (FeKα radiation of 40 kV, 30 mA). N_2 adsorption–desorption isotherms were measured using a Quantachrome Autosorb-1 apparatus. The sample was preheated at 120 °C for 3 h under vacuum. Pore size distributions were calculated from the adsorption branch by the BJH method. Solid-state ^{29}Si magic-angle spinning (MAS) NMR measurement was recorded using a JEOL JNM-CMX-400 spectrometer at a resonance frequency 79.42 MHz with a pulse width of 45 and a recycle delay of 100 s. Chemical shifts for ^{29}Si MAS NMR were referenced to poly(dimethylsilane) at –33.8 ppm. FT-IR spectra were recorded on a JASCO FT/IR 6100 spectrometer by a KBr disk technique.

4.2.2 Results

4.2.2.1 Characterization of SBA-15/Au

The TEM images of SBA-15/Au are shown in Fig. 4.4a and b. A rod-like morphology replicated from the cylinder-like pore of SBA-15 was observed along the mesopores of SBA-15. The diameter of the nanorods was estimated to be about 8 nm, corresponding to the pore size of SBA-15. These results show that Au was deposited inside the mesopores of SBA-15. Furthermore, it should be noted that almost no particles other than nanorods were observed even in the low-magnified TEM image (Fig. 4.4a), indicating that single-phase Au nanorods were obtained.

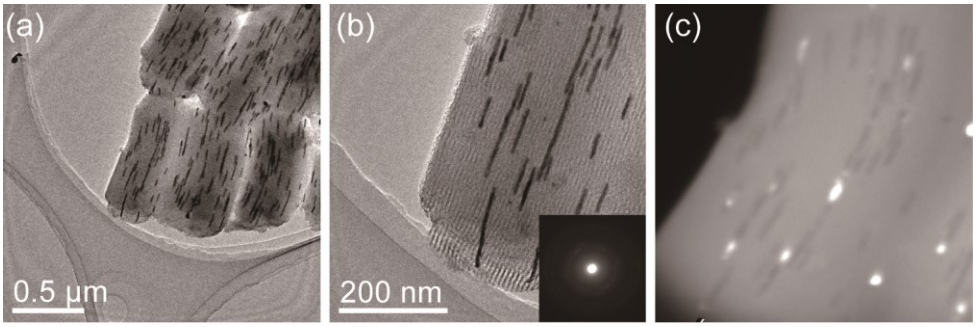

Figure 4.4 TEM images of SBA-15/Au (a) low-magnification, (b) high-magnification (inset: corresponding SAED pattern) and (c) dark-field TEM image in the same area as (b).

The SAED pattern (Fig. 4.4b, inset) showed ring-like diffractions, although the intensity of the diffractions was very weak. This weak intensity can be explained by both the small amount of Au in the area and electron-beam scattering by mesoporous silica. The single-crystalline domain size of the Au nanorods was estimated to be less than 30 nm as determined from dark-field TEM image (Fig. 4.4c), which was smaller than the long-axis length (several tens of nm to *ca.* 200 nm); these data are indicative of the polycrystalline nature of the Au nanorods. As determined from the 111 lattice plane in the XRD pattern of SBA-15/Au (Fig. 4.5), the crystallite size was calculated as *ca.* 16 nm by the Scherrer equation using the Scherrer constant K = 1. This calculated value is close to that estimated from the dark-field TEM image, which suggests that Au nanorods were formed inside SBA-15/Au without the accompanying formation of bulk Au particles. After the reduction, silanol groups located on the surface of SBA-15 were modified with TMDS at least partly, which is supported by the reduction of the signal due to Q^3 units of SBA-15 and the presence of signals due to M and D units of TMDS (Figure 4.6). Three bands at 2924 cm^{-1} (CH_3 sym stretching), 2853 cm^{-1} (CH_3 asym stretching), and 2148 cm^{-1} (Si–H stretching) were observed in the FT-IR spectrum of SBA-15/Au (Figure 4.7), also supporting the surface modification with TMDS.

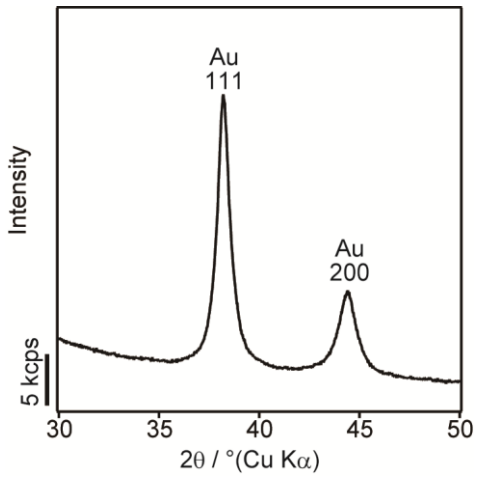

Figure 4.5 XRD pattern of SBA-15/Au.

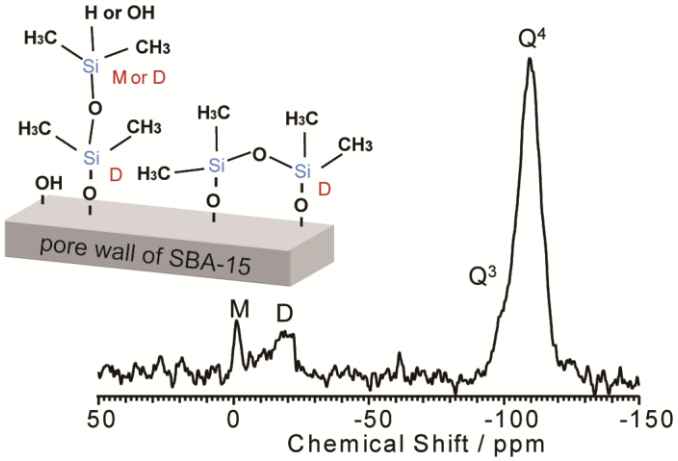

Figure 4.6 ^{29}Si MAS NMR spectrum of SBA-15/Au

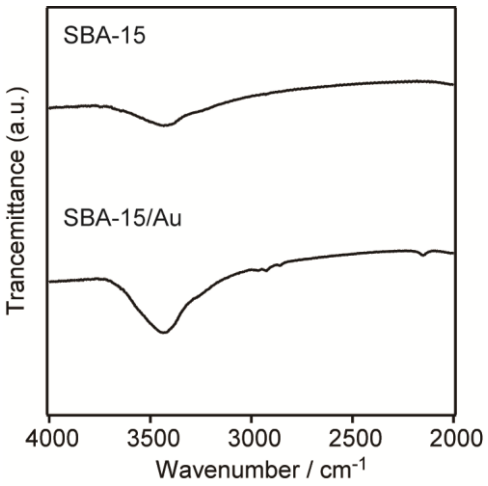

Figure 4.7 FT-IR spectra of SBA-15 and SBA-15/Au.

4.2.2.2 Characterization of SBA-15/Au_C_{16}TMAB

The liquid-phase deposition has advantages from the viewpoint of the control of reductive behavior using capping agents, such as surfactants and polymers. This controllability is important for preparation of nanostructured Au because reductive behavior is related to the morphology and size of deposited Au inside mesoporous silica. Therefore, we added C_{16}TMAB, often used as a capping agent for preparation of nanostructured Au in a liquid phase,[12] to the hexane solution prior to reduction.

The TEM image of SBA-15/Au_C_{16}TMAB is shown in Fig. 4.8a and b. The removal of C_{16}TMAB molecules was confirmed by EDX spectra of SBA-15/Au_C_{16}TMAB before and after washing (Figure 4.8b and c), showing the absence of bromide and chloride ions after washing. Au nanoparticles were observed with morphologies noticeably different from the Au nanorods prepared without C_{16}TMAB. In addition, the formed Au nanoparticles had a noticeably wider distribution than Au nanorods, although accurate three-dimensional distributions could not be obtained from the TEM images. The diameters of the nanoparticles were *ca.* 8 nm, almost identical to the pore size of SBA-15. Outer deposition of Au was not observed even in the low-magnified TEM image (Figure 4.8a) as well as SBA-15/Au. The crystallite size was calculated as about 8 nm from the 111 lattice plane in the XRD pattern (Fig. 4.9) using the Scherrer equation, indicating that each Au nanoparticle was single crystalline. In contrast, when the amount of C_{16}TMAB was decreased, not only nanoparticles but also nanorods were observed (Figure 4.10). These data show that C_{16}TMAB changed the morphology of nanostructured Au inside mesoporous silica; the reason for this morphological variation by the addition of C_{16}TMAB is discussed in the next section.

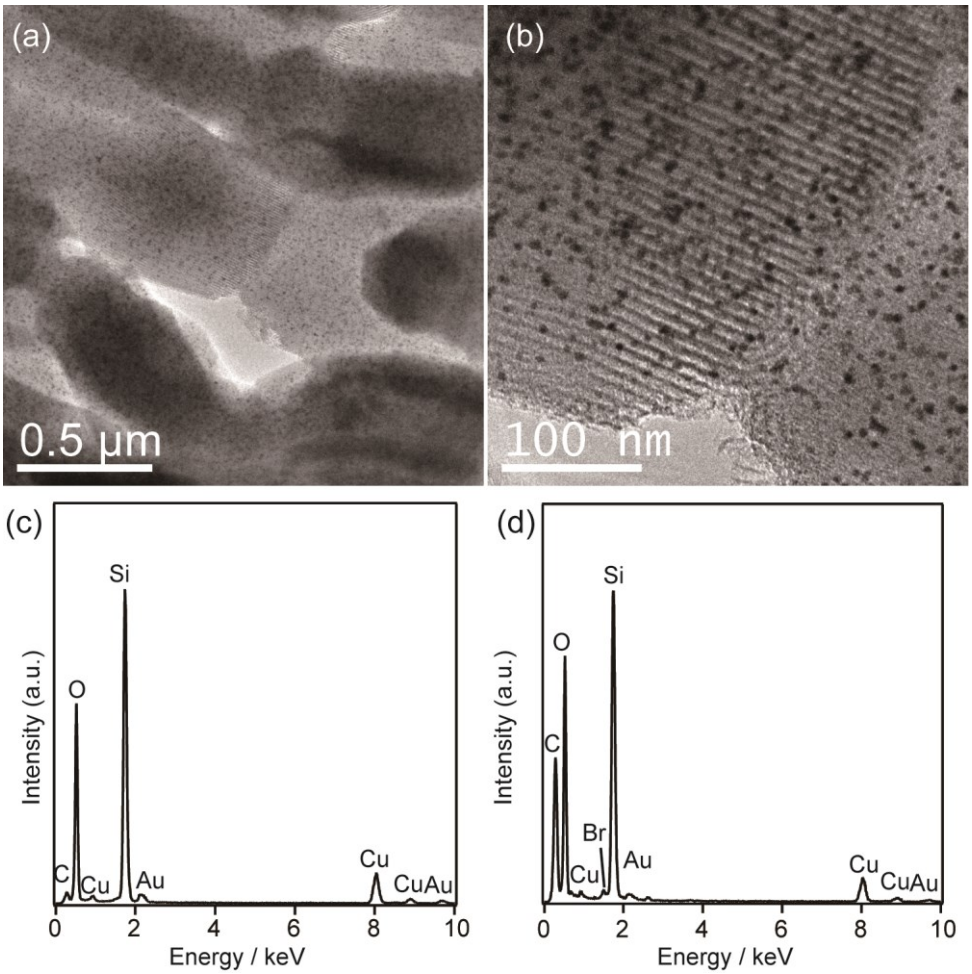

Figure 4.8 (a) Low-magnified and (b) high-magnified TEM images of SBA-15/Au_C_{16}TMAB and (c), (d) corresponding EDX spectra; (c) after and (d) before the washing procedure.

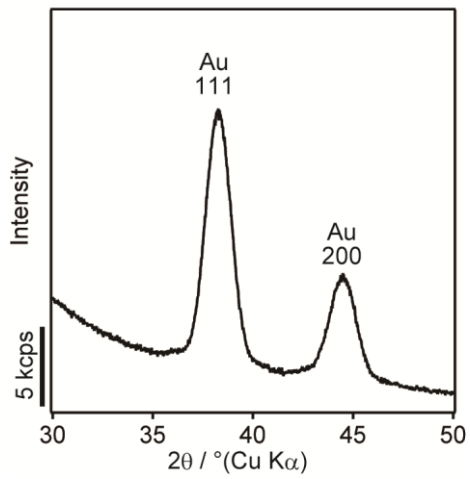

Figure 4.9 XRD pattern of SBA-15/Au_C_{16}TMAB.

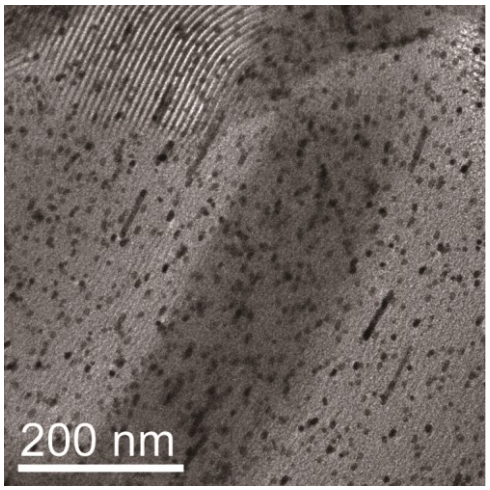

Figure 4.10 TEM image of SBA-15/Au_C_{16}TMAB prepared by the reduction in the presence of 0.025 mmol of C_{16}TMAB.

We have already reported the preparation of nanostructured Pt using a mesoporous silica film in the presence of surfactant molecules using an electrodeposition process.[13] Although electrodeposition is suitable for metal deposition within mesopores in a liquid phase because the deposition site is limited to the surface of substrate, a conductive substrate is necessary for successful preparation. Conversely, the deposition method using a chemical reducing agent reported here is advantageous in terms of its applicability to not only powders but also films on insulating substrates.

4.2.3 Discussion

4.2.3.1 Significance of the use of non-polar compounds as a solvent and a reducing agent

In this study, we have succeeded in performing Au deposition solely inside mesoporous silica without surface modification. The most significant difference between the preparative method reported here and those in previous reports is the use of non- polar-liquid as a medium for reductive deposition. Therefore, this difference is

strongly related to successful Au deposition.

In order to deposit Au inside mesoporous silica, the migration of Au species must be suppressed. Au species migrate inside mesoporous silica either by pore surface diffusion or pore bulk diffusion; pore surface diffusion is the dominant migration mechanism for compounds interacting with the surface of mesoporous silica, whereas pore bulk diffusion predominates for compounds that do not interact with the surface.[34] The diffusion coefficient of pore surface diffusion is much smaller than that of pore bulk diffusion.[14] In addition, stronger interactions will lead to slower pore surface diffusion.[15] Therefore, it is vital to promote stronger interactions of Au species with mesopore surfaces in order to suppress the migration of Au species.

In the initial reduction process, Au precursors and partially reduced precursors, both of which are ionic compounds, exist within the mesopores. The ionic Au compounds interact with the silica surfaces owing to the presence of polar silanol groups. In particular, because hexane has a low affinity with the ionic Au compounds, these species should be located near the surface in the hexane solution; this suggests that the use of hexane leads to the restriction of the Au species migration by pore surface diffusion which is much slower than pore bulk diffusion[14a] –one of roles of hexane for controlled Au deposition inside mesoporous silica. Because the interactions between polar compounds increase inversely with the dielectric constant of the reaction medium, it is reasonable to suggest that the use of solvent with extremely low dielectric constant such as hexane suppresses migration. Outer deposition of Au was slightly observed when other reducing agents, like triethyl-, butyl-, and hexyl-silanes were used (Figure 4.11). The use of triphenylsilane induced larger outer deposition of Au. The function of reducing agent in the non-polar systems needs further studies.

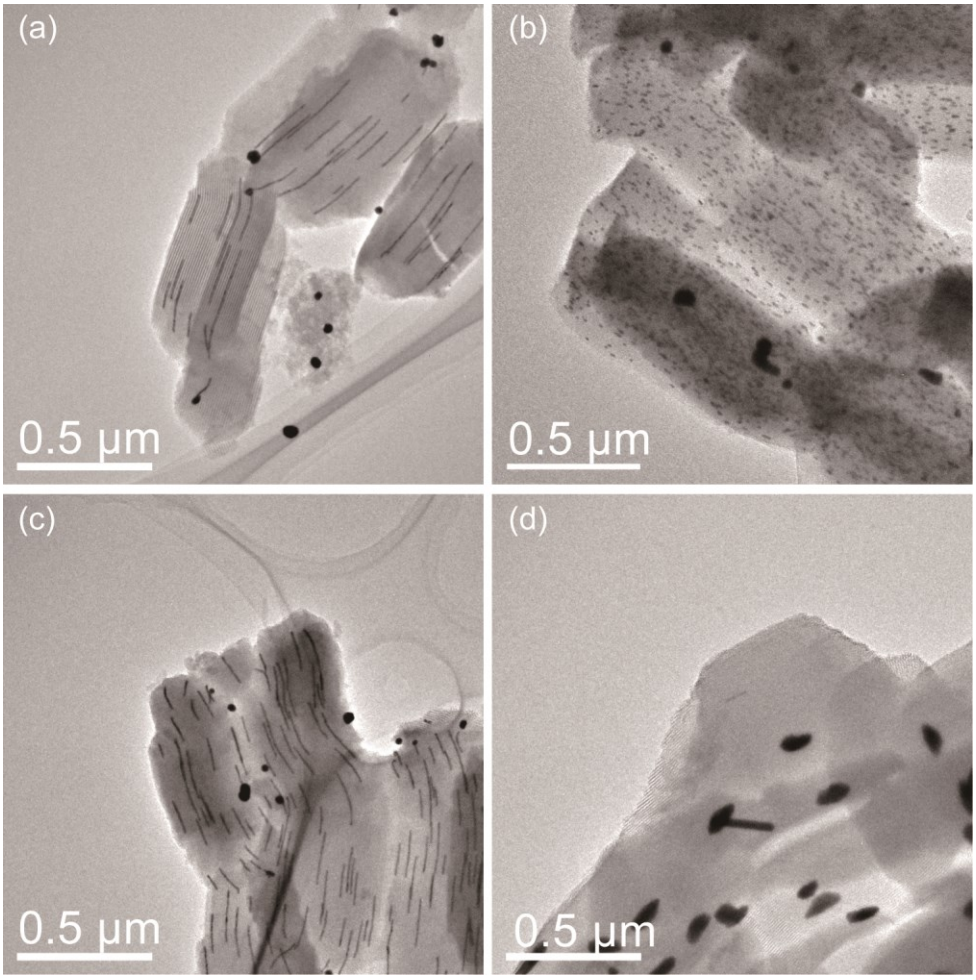

Figure 4.11 TEM images of SBA-15/Au prepared by using (a) triethylsilane, (b) tributylsilane, (c) trihexylsilane, and (d) triphenylsilane as reducing agents, respectively.

With the progress of the reduction process, Au atoms or clusters, which are no longer ionic compounds, are formed within the mesopores. As a result of the weak interactions between silanol groups and Au, Au atoms or clusters should migrate not only by pore surface diffusion but also pore bulk diffusion.[14a] Although this is not related to the state (liquid or gas) of the reductive reaction medium, the diffusion coefficient for pore bulk diffusion in the liquid phase is smaller than that in the gas phase by two to three orders of magnitude.[14b] This means that the use of liquid hexane as the reductive reaction medium suppresses the migration of Au species compared to

the gas phase.

4.2.3.2 Effect of the addition of C_{16}TMAB

As shown in the Results section, the addition of C_{16}TMAB into the hexane solution before reduction resulted in the formation of Au nanoparticles within the mesopores. Here, the effect of the addition of C_{16}TMAB is discussed. C_{16}TMAB forms complexes with $HAuCl_4$ (C_{16}TMA-$AuBr_4$),[11] and is known to strongly interact with Au atoms and clusters.[12] Therefore, the apparent sizes of Au species are presumed to enlarge further in the presence of C_{16}TMAB than in the absence of C_{16}TMAB, which should suppress the migration of Au species within the mesopores. As previously demonstrated, because the molecular size of C_{16}TMAB is comparative to the complementary pores,[10] migration between the mesopores through these pores should be suppressed. This naturally disturbs the crystal growth or aggregation of Au, resulting in the formation of Au nanoparticles.

4.2.4 Summary

The use of non-polar liquid as a solvent and reducing agent is demonstrated to be valuable for controlled Au deposition exclusively inside mesoporous silica. Hexane and reducing agent TMDS play critical roles in suppressing the migration of Au species within the mesopores. In addition, the selective preparation of Au nanoparticles and nanorods was successfully achieved by simply performing reductive deposition in the presence or absence of C_{16}TMAB. The use of surfactants such as C_{16}TMAB for the hard templating method is advantageous for the liquid phase deposition process reported here, which enables further precise design of nanostructured Au materials.

4.3 Preparation of mesoporous bimetallic Au-Pt with a phase segregated heterostructure using mesoporous silica

This section describes the preparation of mesoporous bimetallic Au-Pt with phase segregated heterostructures using SBA-15[10] as a template. Au nanoparticles were prepared as seed metals within the mesopores of SBA-15 by using the deposition method in section 4.2, and subsequently Pt was deposited[16] in between the Au seeds (Scheme 4.2). A combination of Au and Pt was chosen because carbon monoxide can be used to probe the surface compositional properties of bimetallic Au-Pt since the electrooxidation behavior of adsorbed CO on Au and Pt occur at different electrode potential.[17] Hence, CO_{ad} stripping voltammetry should provide information regarding the alloying state of mesoporous bimetallic Au-Pt as well as the surface Au/Pt ratio. Furthermore, the Au/Pt ratio, which has a strong impact on the surface properties of bimetallic Au-Pt, was varied by controlling the deposition time of Au in order to demonstrate the usefulness of the preparative method for tuning the properties.

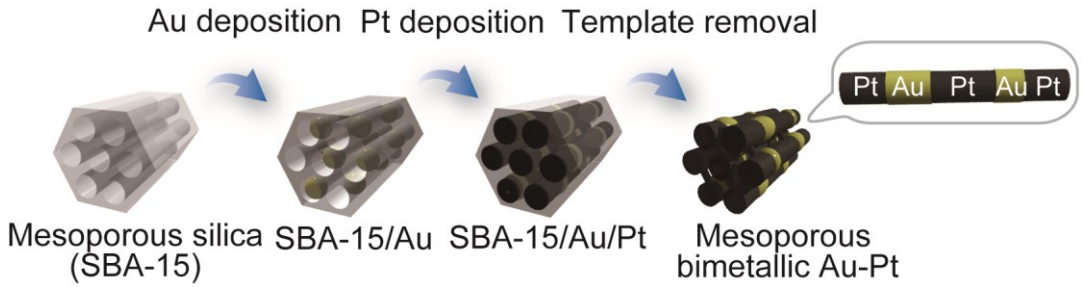

Scheme 4.2 Preparation of mesoporous bimetallic Au-Pt with a phase segregated heterostructure.

4.3.1 Experimental

4.3.1.1 Material

Tetraethoxysilane (TEOS, Kishida Chemical Co.), triblock copolymer $EO_{20}PO_{70}EO_{20}$ (Pluronic 123, Aldrich Co.), and hydrochloric acid (35–37 wt%, Wako

Pure Chemical Industries Ltd.) were used for the preparation of SBA-15. $HAuCl_4 \cdot 4H_2O$ (Kanto Chemical Co., Inc.) and $H_2PtCl_6 \cdot 6H_2O$ (Wako Pure Chemical Industries Ltd.) were used as Au and Pt precursors, respectively. Anhydrous ethanol was used as a solvent for incorporation of the Au and Pt precursors. Anhydrous hexane (Wako Pure Chemical Industries Ltd.), 1,1,3,3-tetramethyldisiloxane (TMDS, Tokyo Chemical Industry Co., Ltd.), and hexadecyltrimethylammonium bromide (C_{16}TMAB, Wako Pure Chemical Industries Ltd.) were used as solvent, reducing agent, and capping agent, respectively, for the preparation of Au nanoparticles incorporated into SBA-15. Dimethylamine borane (DMAB, Wako Pure Chemical Industries Ltd.) was used as a reducing agent to deposit Pt inside the mesopores. Hydrofluoric acid (Wako Pure Chemical Industries Ltd.) was used for removal of the silica template. Ultrapure water was used for all experimental procedures in the electrochemical analyses.

4.3.1.2 Preparation of Au nanoparticles incorporated into SBA-15 (SBA-15/Au(X))

Mesoporous silica SBA-15, used as a template, was synthesized at 130 °C according to a previous procedure.[10] Although the temperature of the hydrothermal treatment was same as that in Chapter 3, the preparation was performed in the different batches. Therefore, the textural properties of SBA-15 prepared in this section are slightly different with those of SBA-15 prepared in Chapter 3. The complementary pores between mesopores, which are characteristic of SBA-15,[10] ensured the accessibility of Pt species into the mesopores even when Au nanoparticles had already been deposited within them. The prepared SBA-15 had a highly ordered 2D hexagonal mesostructure, as evidenced by its small angle X-ray diffraction (XRD) pattern (Figure 4.12) and transmission electron microscopy (TEM) images (Figure 4.13). The unit cell

parameter of SBA-15 was calculated as 11.2 nm from the d_{10} spacing in the XRD pattern.

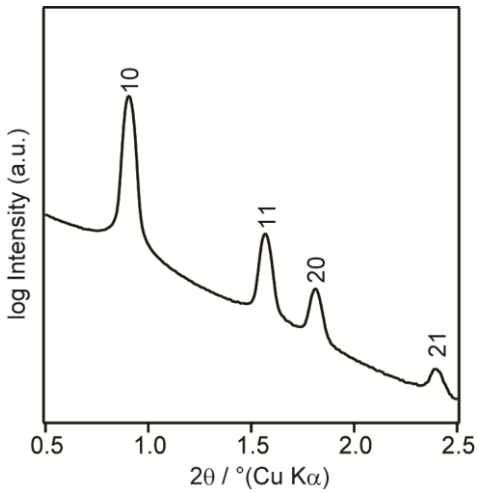

Figure 4.12 Small angle XRD pattern of SBA-15.

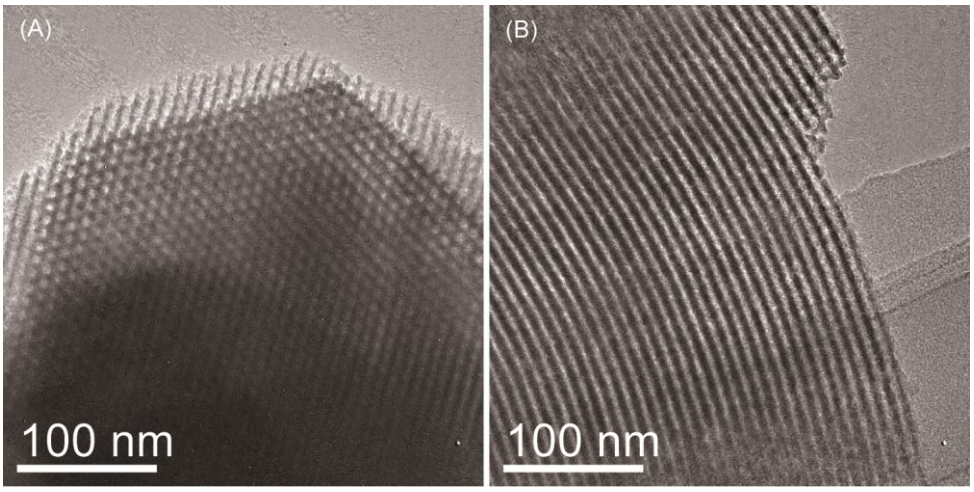

Figure 4.13 TEM images of SBA-15 taken from (A) perpendicular and (B) parallel to the pore axis.

The N_2 adsorption-desorption isotherm of SBA-15 (Figure 4.14A) was a typical type IV curve, and the pore size was calculated as 9.2 nm by using Barrett–Joyner–Halenda (BJH) method (Figure 4.14B).

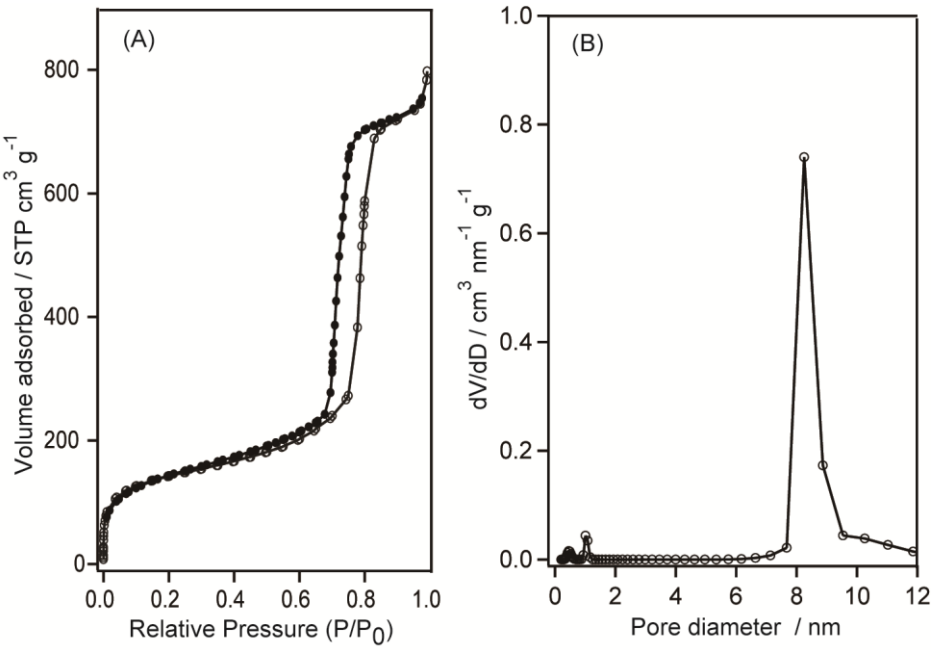

Figure 4.14 (A) N_2 adsorption-desorption isotherm and (B) BJH pore size distribution of SBA-15.

SBA-15/Au with different Au/Si ratios were prepared by slightly modifying the method in section 4.2. SBA-15 was dried under reduced pressure at 120 °C for 3 h to remove adsorbed water. The dried SBA-15 (0.3 g) was dispersed in anhydrous ethanol (30 mL). A stock solution (2.4 M $HAuCl_4 \cdot 4H_2O$) was prepared by dissolving $HAuCl_4 \cdot 4H_2O$ (1.0 g) in anhydrous ethanol (1.0 mL). An aliquot of the stock solution (72 μL, 0.17 mmol) was added to the dispersion of SBA-15 in ethanol. The mixture was placed under reduced pressure to incorporate the Au precursor into the mesopores of SBA-15 until a dry yellow powder was obtained. The obtained powder was further dried under reduced pressure for at least 2 h. This procedure was essential to prevent outer deposition of Au. The dried powder was dispersed in anhydrous hexane (15 mL) containing C_{16}TMAB 0.55 g, 13 mmol), and the solution was stirred at room temperature for 1 h. Then, TMDS (618 μL, 3.6 mmol) was then added to the solution under stirring. After further stirring for 1 h, the dispersion in hexane was filtered. The

obtained powder was washed with hexane and ethanol to remove the reducing agent and C_{16}TMAB, and then dried at room temperature.

For the preparation of SBA-15/Au with a larger amount of Au, the procedure described above was basically repeated once or twice more. The obtained samples are denoted as SBA-15/Au(X), where X is the number of Au deposition cycle.

4.3.1.3 Preparation of mesoporous bimetallic Au-Pt with a phase segregated heterostructure (mp-Au(Y)/Pt)

Pt was deposited through vapor infiltration of DMAB.[16,18] The prepared SBA-15/Au(X) was dried at 120 °C for 3 h to remove adsorbed water. The dried SBA-15/Au(X) (0.2 g) was dispersed in anhydrous ethanol (20 mL). A stock solution (1.9 M $H_2PtCl_6 \cdot 6H_2O$) was prepared by dissolving $H_2PtCl_6 \cdot 6H_2O$ (1.0 g) in anhydrous ethanol (1.0 mL). The amount of stock solution added was set at 600 μL/0.2 g SiO_2. The SiO_2 contents of 0.2 g of SBA-15(X) (X = 1, 2, and 3) were calculated to be 0.19, 0.18, and 0.16 g, respectively, from the inductively coupled plasma optical emission spectroscopy (ICP-OES) data. Therefore, 560, 530, or 490 μL of the stock solution was added to dispersion of SBA-15/Au(X) (X = 1, 2, or 3), respectively, in ethanol. The mixture was placed under reduced pressure to incorporate the Pt precursor into the mesopores of SBA-15/Au(X) until a dry powder was obtained. The obtained powder was put on a dish, and the dish was placed in a closed vessel along with DMAB (2.0 g, 34 mmol) on another dish, at 45 °C for 7 d. The powder was stirred with a spatula once a day. After 7 d, the powder was washed with ethanol and dried at room temperature (SBA-15/Au(X)/Pt). Finally, SBA-15/Au(X)/Pt was stirred in 10 wt% aqueous HF solution at room temperature for 3 h to remove the silica template. The obtained

samples are denoted as mp-Au(Y)/Pt, where Y denotes the Au/Pt ratio calculated from quantitative ICP-OES data. For comparison, mesoporous Pt (mp-Au(0)/Pt) was prepared by omitting the procedure for the incorporation of Au nanoparticles.

4.3.1.4 Analysis of surface compositional properties of mp-Au(Y)/Pt

All electrochemical measurements were performed by using a three-electrode system at room temperature. A beaker-type electrochemical cell equipped with a glassy carbon working electrode, a platinum mesh counter, and an Ag/AgCl/KCl (satd.) reference electrode, connected with a salt bridge, was used. All potentials reported herein are referred to the reversible hydrogen electrode (RHE) scale.

Aqueous solutions of mp-Au(Y)/Pt (1 mg mL^{-1} catalyst) were prepared by sonication of the samples in ultrapure water for 10 min. Working electrodes were prepared by dropping 20 μL of the catalyst solution onto a glassy carbon electrode and drying at 60 °C. This procedure was repeated once more. Then, 20 μL of 1 wt% Nafion ionomer solution (Aldrich Co.) was dropped onto the electrode surface and dried at 60 °C to immobilize the catalysts. The amount of catalyst on each electrode was estimated by ICP-OES measurement of the catalyst solution.

Pre-adsorbed CO (CO_{ad}) stripping voltammetry was utilized to characterize the surface compositional properties of mp-Au(Y)/Pt. Prior to CO_{ad} stripping voltammetry, the potential was cycled between 0.05 V and 1.6 V in 0.5 M H_2SO_4 at a scan rate of 50 mV s^{-1} for 10 cycles to clean the surface. CO gas was introduced to purge the electrolyte for 30 min while maintaining a constant voltage of 50 mV vs. RHE to allow complete adsorption of CO onto the catalyst surface. Excess CO in the electrolyte was then purged out by bubbling N_2 gas for 30 min. CO_{ad} stripping voltammetry was

performed at a scan rate of 10 mV s^{-1}. The electrochemical surface areas (ECSAs) of the catalysts were calculated from the CO stripping voltammograms assuming a monolayer of linearly adsorbed CO on the metal surface and the coulombic charge required for the oxidation to be 420 μC cm^{-2} ($ECSA_{CO}$). The ECSA was normalized by the amount of Pt on the electrode surface, assuming that CO was adsorbed only on Pt surface. For comparison, the ECSA was also calculated from the hydrogen desorption peaks ($ECSA_H$) assuming that the coulombic charge required for the oxidation on polycrystalline Pt was 210 μC cm^{-2}.

4.3.1.5 Characterization

TEM images and energy dispersive X-ray (EDX) spectra of SBA-15, SBA-15/Au(X), and SBA-15/Au(X)/Pt were acquired on a JEOL JEM-2010 microscope using an accelerating voltage of 200 kV. TEM images and EDX spectral mappings of mp-Au(Y)/Pt were acquired on a JEOL JEM-2100F microscope with an accelerating voltage of 200 kV. Samples for TEM and EDX measurements were dispersed in ethanol, and the dispersions were dropped onto a carbon-coated microgrid (Okenshoji. Co). XRD patterns at very small diffraction angles were recorded with a Rigaku NANO-Viewer using CuKα radiation with operating conditions of 40 kV and 30 mA, employing a Pilatus 2D X-ray detector (Dectris). N_2 adsorption-desorption isotherms were measured with a BELSORP-max (MicrotracBEL Co.) at –196 °C. Prior to the N_2 adsorption-desorption measurement, SBA-15 was heated at 120 °C under reduced pressure and mesoporous metal samples were placed under reduced pressure at room temperature. The pore size was determined from the adsorption data. High-angle XRD patterns were recorded with a Rigaku RINT-Ultima III diffractometer using CuKα

radiation under operating conditions of 40 kV and 40 mA, employing a high-speed 1D X-ray detector (D/teX Ultra). Electrochemical measurements were performed with an HSV-100 (Hokuto Denko Co.). ICP-OES analysis was conducted on a Thermo Scientific iCAP 6500 Duo-ICP-OES. X-ray photoelectron spectroscopy (XPS) profiles were measured with a PHI 5000 VersaProbe II (ULVAC-PHI, Inc.) using monochromated AlKα radiation. The peak shift due to the charging was corrected by using the C 1s core-level peak at 284.8 eV as a reference.

4.3.2 Results and discussion

4.3.2.1 Characterization of SBA-15/Au(X)

The Au/Si ratios of SBA-15/Au(X) (X (number of deposition times = 1, 2, and 3) are calculated as 0.020, 0.043, and 0.069, respectively, on the basis of ICP-OES measurements. In the high angle XRD patterns (Figure 4.15A), the peaks could be attributed to face-centered cubic Au. The intensities of the peaks became stronger with increasing number of deposition cycles, consistent with the ICP-OES measurements. As determined from the full-width at half-maximum of the 111 diffraction peaks in the XRD pattern, the crystallite sizes of SBA-15/Au(X) (X = 1, 2, and 3) were calculated as 8 nm, 9 nm, and 12 nm, respectively, by using the Scherrer equation.

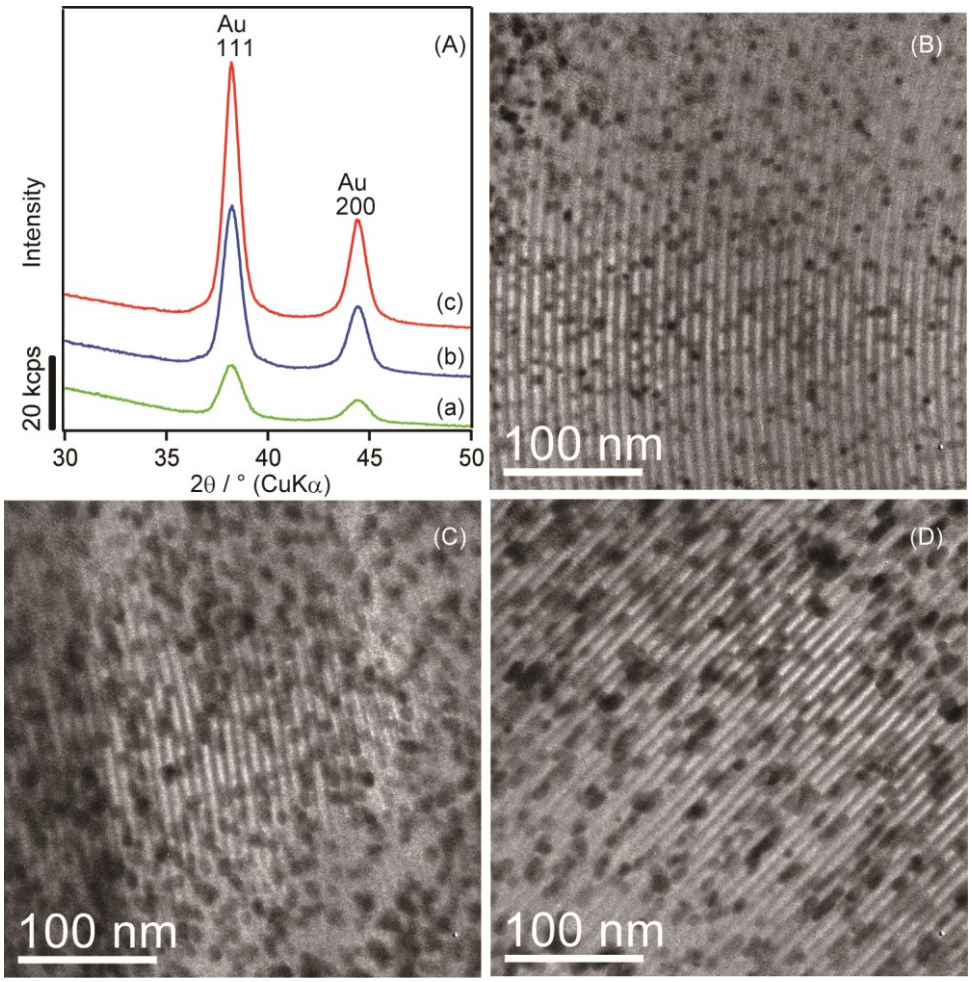

Figure 4.15 (A) High angle XRD pattern of SBA-15/Au(X) (X = 1, 2, and 3). TEM images of SBA-15/Au(X); X = (B) 1, (C) 2, and (D) 3.

The TEM images of SBA-15/Au(X) (Figure 4.15B-D) showed that Au nanoparticles were formed within the mesopores. Elongation of the Au nanoparticles along the mesopores was observed for SBA-15/Au(2) and /Au(3). The sizes of the Au nanoparticles along the mesopores were estimated as 7–14 nm from the TEM images. These data correspond well with the crystallite sizes calculated from the XRD patterns. The particle sizes were consistent with the pore sizes, which is essential for forming a phase-segregated heterostructure within the mesopores. Outer deposition of Au was not observed even in the low-magnified TEM images (Figure 4.16), which is crucial for the

preferential deposition of Pt inside the mesopores. Furthermore, the low-magnified TEM images clearly showed that the number of Au nanoparticles increased with increasing number of deposition cycles. The absence of peaks due to N and Br in the EDX spectra indicated complete removal of C_{16}TMAB molecules (Figure 4.16). It should be noted that the large amount of Au nanoparticles formed within the mesopores (*ca.* 18 wt%) by repeated deposition was remarkable. Previous studies on preparation of Au nanoparticles within mesopores showed that the amount of loaded Au is variable but of the order of a few weight percent. Higher Au loadings reported previously were inevitably due to in part to outer deposition of Au.[8b] The reason for the successful deposition of such a large amount of Au within the mesopores (and without outer deposition) is the presence of C_{16}TMA cations during the reduction, which suppress the migration of capped Au nanoparticles to the outside region as described in section 4.2.

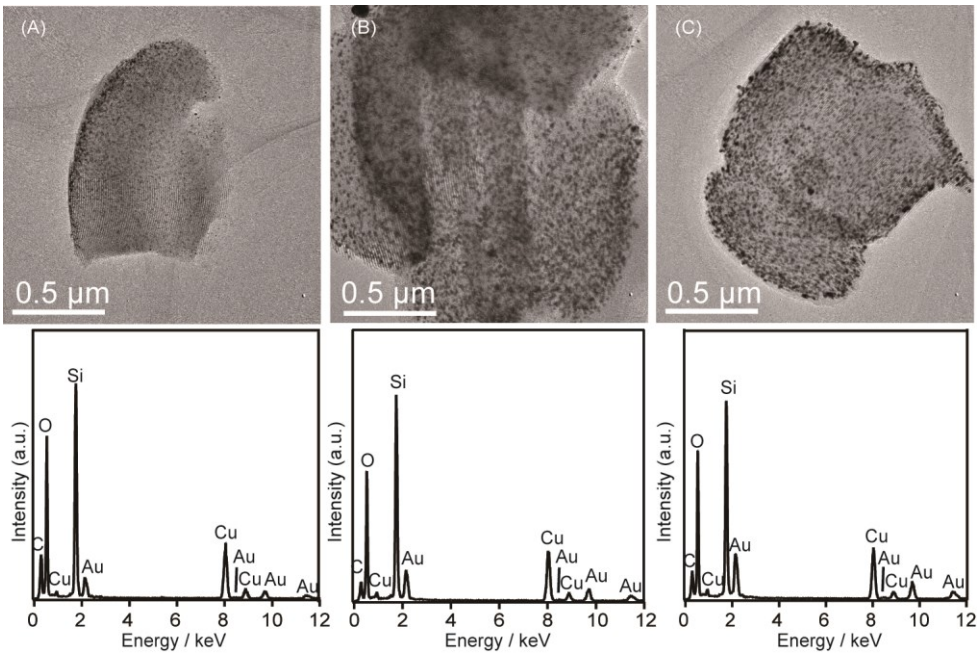

Figure 4.16 Low-magnified TEM images (upper) and corresponding EDX spectra (bottom) of SBA-15/Au(X); X = (A) 1, (B) 2, and (C) 3. The peaks of C and Cu are due to the TEM grid.

4.3.2.2 Characterization of SBA-15/Au(X)/Pt

After 1 day of reduction, Pt was deposited within the mesopores to form nanorods replicated from the pore shape (Figure 4.17).

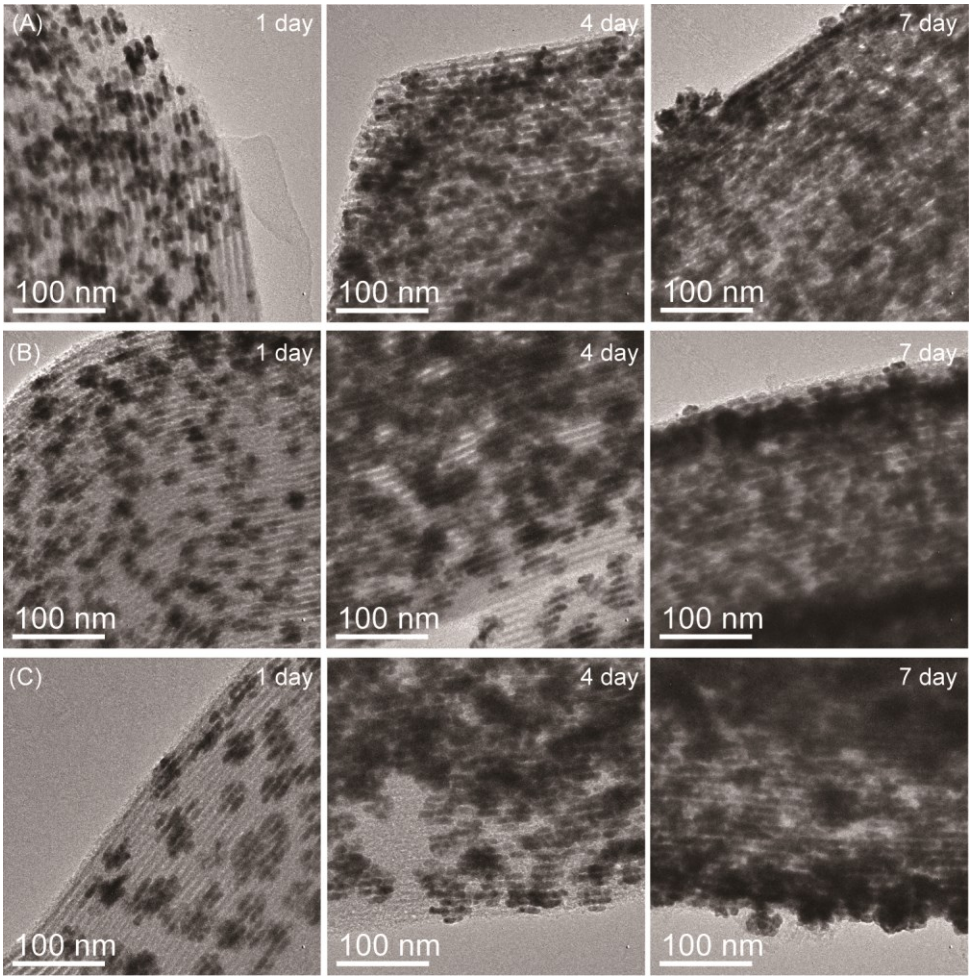

Figure 4.17 TEM images of SBA-15/Au(X)/Pt; X = (A) 1, (B) 2, and (C) 3 for 1 d, 4 d, and 7 d of reduction, respectively.

With increasing reduction time, the nanorods were further elongated along the mesopores. Because the Pt precursor could infiltrate into the mesopores even in the presence of preformed Au nanoparticles owing to the characteristic complementary pores between the mesopores of SBA-15,[10] Pt was successfully deposited within mesopores. Indeed, this is the reason why we chose SBA-15 as a template. It should be

noted that no deposition of Pt was observed on the outer surface of SBA-15. These result showed promise for the successful formation of mesoporous metals replicated from the template.[16] It is remarkable that the original morphology of the Au nanoparticle seeds within the mesopores, as shown in Figure 4.16, could no longer be observed after just 1 day of reduction. This is strong evidence that the growth of Pt proceeded from the surfaces of the Au nanoparticles, implying the successful formation of the heterojunctions between Au and Pt. The seed-growth of Pt was due to the mild reduction condition involving vapor infiltration of DMAB.[16,18]

4.3.2.3 Characterization of mp-Au(Y)/Pt (mp: mesoporous, Y: ratio of Au/Pt)

The Au/Pt ratios of mp-Au(Y)/Pt samples prepared by using SBA-15/Au(X) (X = 1, 2, and 3) were calculated as 0.09, 0.17, and 0.21, respectively. These larger Au/Pt ratios compared to the initial values (0.06, 0.13, and 0.20) mean that the Pt species were not fully reduced. Although a previous report[16] on the preparation of mesoporous Pt with DMAB also showed incomplete reduction of Pt species, the recovery percentages of Pt in the present study (66%, 77%, and 96%) are much higher than that in the previous report (6%).[16] This can be mainly attributed to the presence of the Au nanoparticle seeds, which promote Pt deposition.[19] The increase in the recovery percentage with the increase in the amount of Au is also consistent with the description.

In the high-angle XRD patterns of mp-Au(Y)/Pt (Figure 4.18), the shoulder peaks around 38°, which can be attributed to Au, became more obvious with increasing Au/Pt ratio. The diffraction angles of the peaks attributed to Pt did not shift compared with those of mp-Au(0)/Pt, suggesting that most of the deposited Pt did not form an Au-Pt solid solution alloy. The crystallite sizes of the deposited Pt were almost the same,

calculated as 10 nm for mp-Au(Y)/Pt (Y = 0, 0.09, 0.17, and 0.21) and 9 nm for mesoporous Pt (i.e. mp-Au(0)/Pt) prepared under the same conditions. We have previously reported that the reduction of Pt species with DMAB yields Pt nanowires typically composed of Pt nanocrystallites several nanometer in size.[16] Considering the calculated crystallite sizes of Au and Pt based on the XRD data, mp-Au(Y)/Pt should be polycrystalline. The peak area ratios of Au to Pt of mp-Au(Y)/Pt (Y = 0.09, 0.17, and 0.21) were calculated as 0.11, 0.15, and 0.20, respectively, by deconvoluting the peaks due to 111 lattice planes in the XRD patterns using a Gaussian function. The ratios were in good agreement with those calculated from the ICP-OES data.

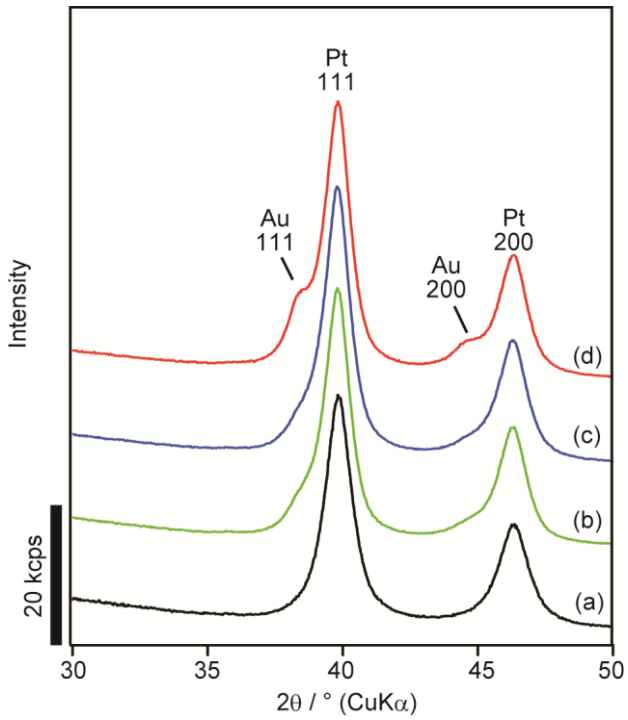

Figure 4.18 High-angle XRD patterns of mp-Au(Y)/Pt; y = (a) 0, (b) 0.09, (c) 0.17, and (d) 0.21.

In the XPS profiles of mp-Au(Y)/Pt (Figure 4.19), the peaks at around 88, 84, 74, or 71 eV were assigned to Au $4f_{5/2}$, Au $4f_{7/2}$, Pt $4f_{5/2}$, or Pt $4f_{7/2}$, respectively. The binding energies were almost consistent with those of pure Au and Pt, respectively.[20]

This indicates the formation of phase segregated structures.

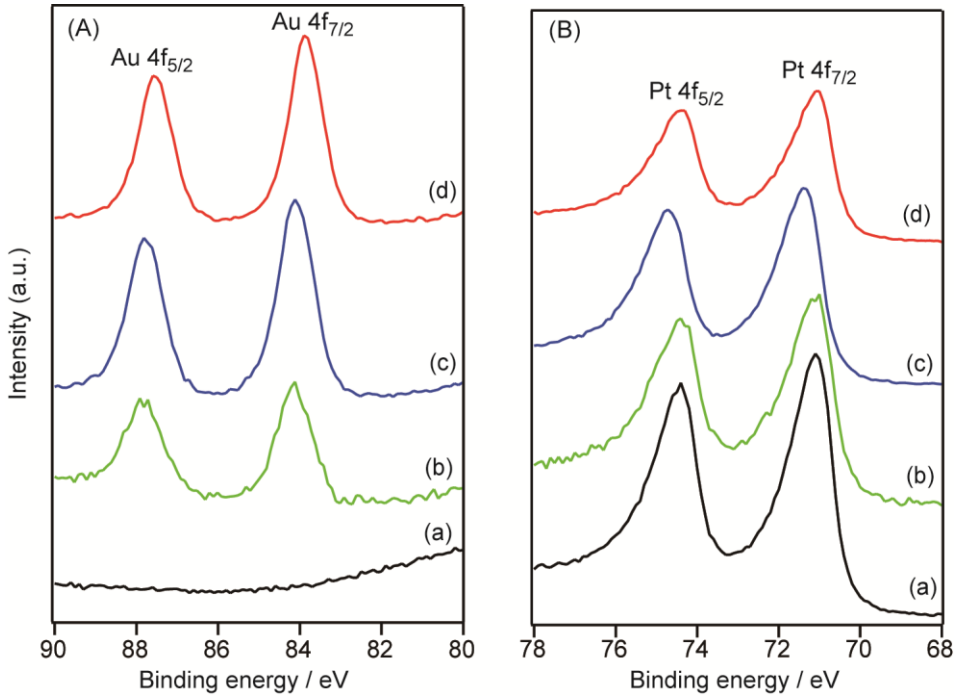

Figure 4.19 XPS profiles of mp-Au/Pt(Y); Y = (a) 0, (b) 0.09, (c) 0.17, and (d) 0.21 for (A) 80–90 eV and (B) 68–78 eV.

The small-angle XRD patterns of mp-Au(Y)/Pt (Figure 4.20) featured a relatively weak and broad peak located at almost the same position as that of the original template. This result indicated the successful formation of ordered mesostructures replicated from the template. The lattice parameters due to the mesostructural ordering of those samples were same (11.2 nm), as determined by the d_{10} spacing in the XRD patterns. The weaker intensities of mp-Au(Y)/Pt in the mesostructural ordering compared to those of the template suggest a decrease in the regularities of the mesostructures, which is a common phenomenon in the hard-templating method.[16]

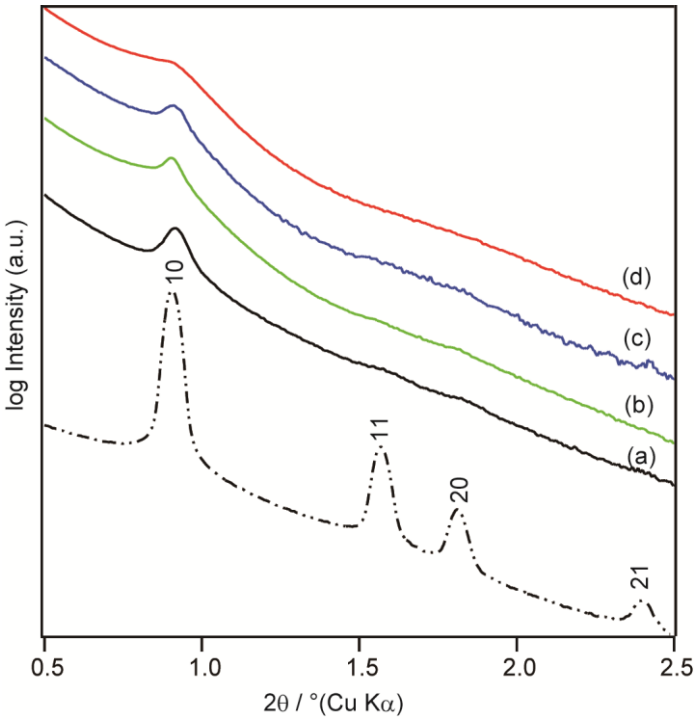

Figure 4.20 Small angle XRD patterns; solid lines: mp-Au(Y)/Pt (Y = (a) 0, (b) 0.09, (c) 0.17, and (d) 0.21); dotted line: SBA-15.

Ordered mesostructures replicated from the template were evident from TEM images of mp-Au(Y)/Pt (Figure 4.21). The periodicity obtained from these TEM images was consistent with that derived from the small angle XRD patterns. EDX spectral mapping of the same area clearly showed that the frameworks of mesostructures were composed of Au nanocrystals and Pt nanowires. This provided direct evidence for the formation of mesoporous bimetallic Au-Pt with a phase-segregated structures. The green dots weakly observed even for the sample with no Au (mp-Au(0)/Pt) are an artifact due to the background signals derived from continuous X-ray source[21] and do not imply Au impurities (Figure 4.21)

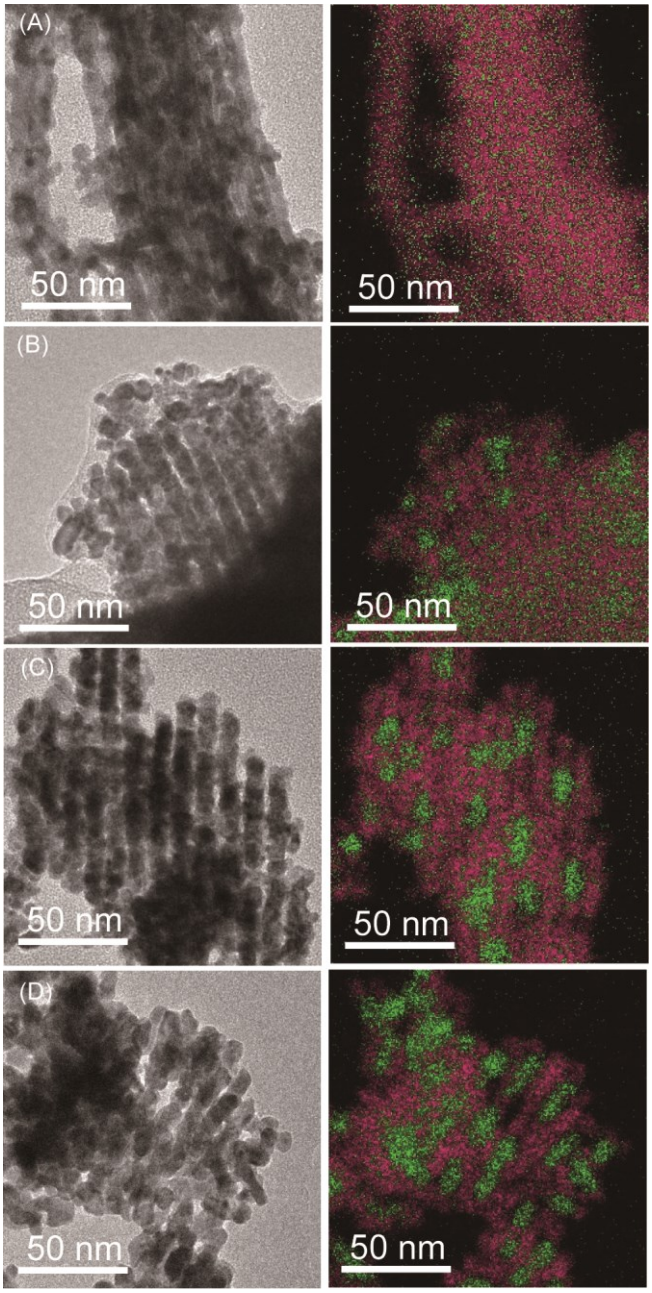

Figure 4.21 TEM images (left) and the corresponding EDX spectral mapping (right) of mp-Au(Y)/Pt (Y = (A) 0, (B) 0.09, (C) 0.17, and (D) 0.21). The purple and green dots indicate Pt and Au, respectively.

N_2 adsorption-desorption isotherms of mp-Au(Y)/Pt (Figure 4.22) showed characteristic profiles due to mesoporous structures, indicating the successful formation of mesoporous materials. The BET surface areas of mp-Au(Y)/Pt (Y = 0, 0.09, 0.17, and

0.21) were calculated as 32, 38, 34, 37 m^2 g^{-1}, respectively. These values are in good agreement with those reported previously for formation of mesoporous Pt prepared by a hard-templating method.[22] Pore size analysis using BJH method showed broad peaks corresponding to a diameter of around 4 nm.

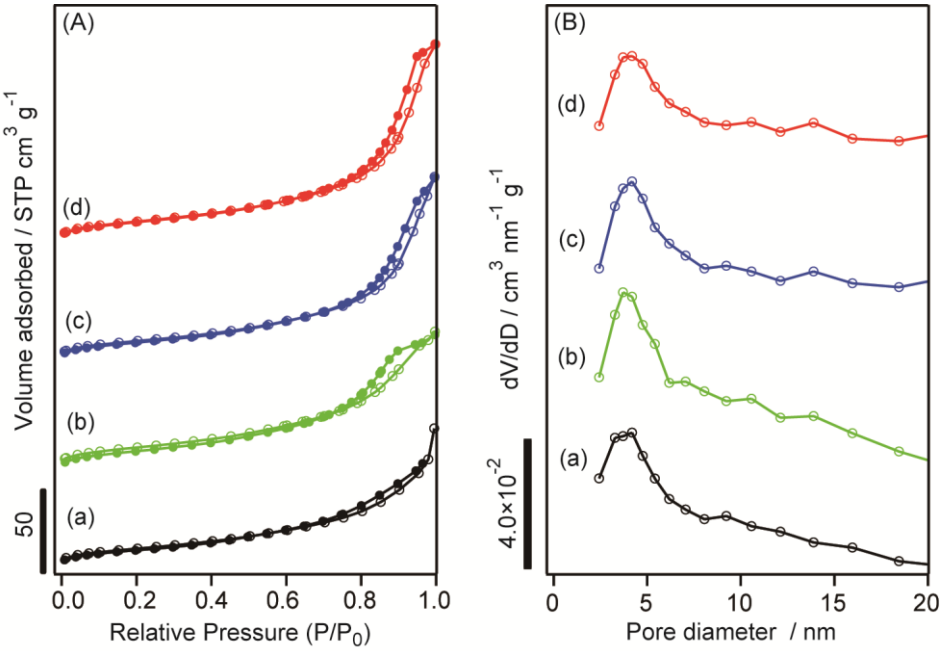

Figure 4.22 (A) N_2 adsorption-desorption isotherms and (B) BJH pore size distributions of mp-Au(Y)/Pt; Y = (a) 0, (b) 0.09, (c) 0.17, and (d) 0.21.

4.3.2.4 Electrochemical analysis of mp-Au(Y)/Pt

In order to analyze the availability of the surfaces of mp-Au(Y)/Pt, electrochemical measurements involving cyclic voltammetry and CO_{ad} stripping voltammetry were performed. In the cyclic voltammograms in the range 0.05–1.6 V (Figure 4.23), oxidation/reduction peaks of both Au and Pt were observed,[17e,g] meaning that the surfaces of both metal components were exposed. The surface Au/Pt ratios of mp-Au(Y)/Pt (Y = 0.09, 0.17, and 0.21) were calculated as 0.10, 0.13, and 0.17, respectively (Table 4.1), from the charge of the oxide reduction peaks of Au and Pt. The

surface Au/Pt ratios of mp-Au(0.17)/Pt and mp-Au(0.21)/Pt were smaller than the Au/Pt ratios obtained from the ICP-OES measurements, which suggests the formation of heterojunctions between Au and Pt as discussed below.

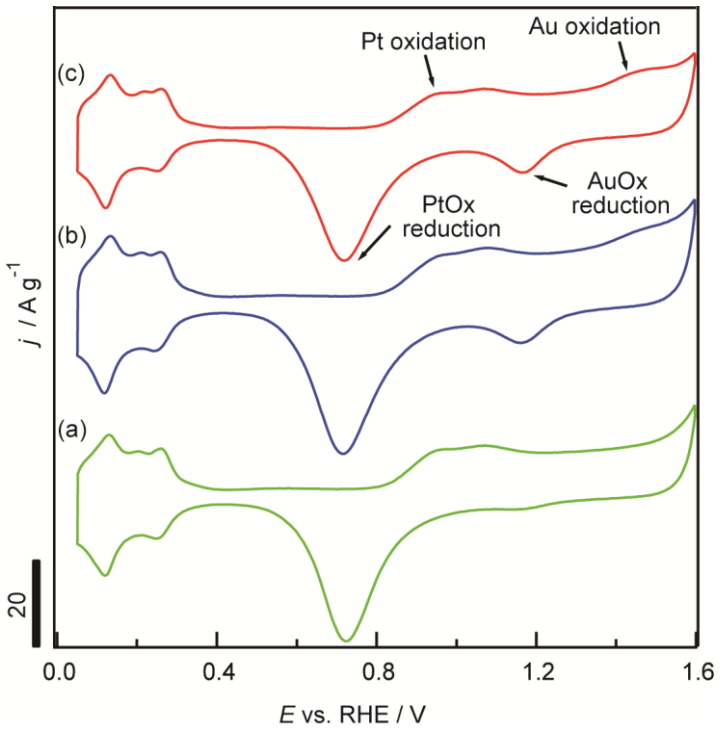

Figure 4.24 Cyclic voltammograms of mp-Au(Y)/Pt (Y = (a) 0.09, (b) 0.17, and (c) 0.21) in 0.5 M H_2SO_4 at 50 mV s^{-1}.

According to previous reports on the CO_{ad} oxidation potential of Pt-coated Au electrodes,[17a-c] the paramters is dependent on the thickness of the Pt coating. Measurement of CO_{ad} oxidation potential should also enable assessment of both the availability of the surfaces of bimetallic structures and the degree of solid solution formation. Table 1 shows $ECSA_{CO}$ and $ECSA_H$. Because Au does not adsorb CO[17c,d] or hydrogen,[23] both $ECSA_{CO}$ and $ECSA_H$ were normalized by the amount of Pt on the electrode surface. The smaller $ECSA_{CO}$ values compared to the $ECSA_H$ values may be explained by the presence of bridged adsorption of CO.[24]

Table 4.1 Results of electrochemical measurements.

Sample name	$ECSA_{CO}$ [m^2 (g-Pt)$^{-1}$]	$ECSA_H$ [m^2 (g-Pt)$^{-1}$]	Surface Au/Pt ratio
mp-Au(0)/Pt	22	28	–
mp-Au(0.09)/Pt	23	30	0.10
mp-Au(0.17)/Pt	29	36	0.13
mp-Au(0.21)/Pt	25	31	0.17

In a previous report on the CO_{ad} stripping measurements of Pt-coated Au nanocrystals,[18a] the oxidation potential was reported to be higher than that of pure Pt by more than 300 mV when a few monolayers of Pt were deposited on Au nanocrystals. The potential shifts to lower values with the increasing Pt thickness. A further increase in the Pt thickness eventually resulted in almost the same potential as that of pure Pt. Therefore, the nature of Pt can be probed by its oxidation potential, which largely depends on the location of Au or the distance from the interface of a heterojunction.

The main CO_{ad} oxidation peaks at around 0.69 V in the CO_{ad} stripping voltammograms slightly shifted to higher potential with increasing Au/Pt ratio. In addition to the main peak, a broad shoulder peak at around 0.75 V was observed for mp-Au(0.17)/Pt and mp-Au(0.21)/Pt. The shift in the broad peak was similar to that in the previous report described above. Therefore, the observed main and broad peaks in the voltammograms of mp-Au(0.17)/Pt and mp-Au(0.21)/Pt show the formation of heterojunction between Au and Pt along with effective use of all the surfaces, including those near the heterojunctions and those of bulk Pt. It should be noted that the accessibility of the surface may be attributed to the mesoporous structures. The difference in the voltammograms between mp-Au(0.17)/Pt and mp-Au(0.21)/Pt may be attributed to the difference in Au/Pt ratio and/or the crystallite size of Au.[18a] The

voltammogram of mp-Au(0.09)/Pt was essentially the same as that of mesoporous Pt (i.e. mp-Au(0)/Pt). The amount of Au was most likely too small to be detected.

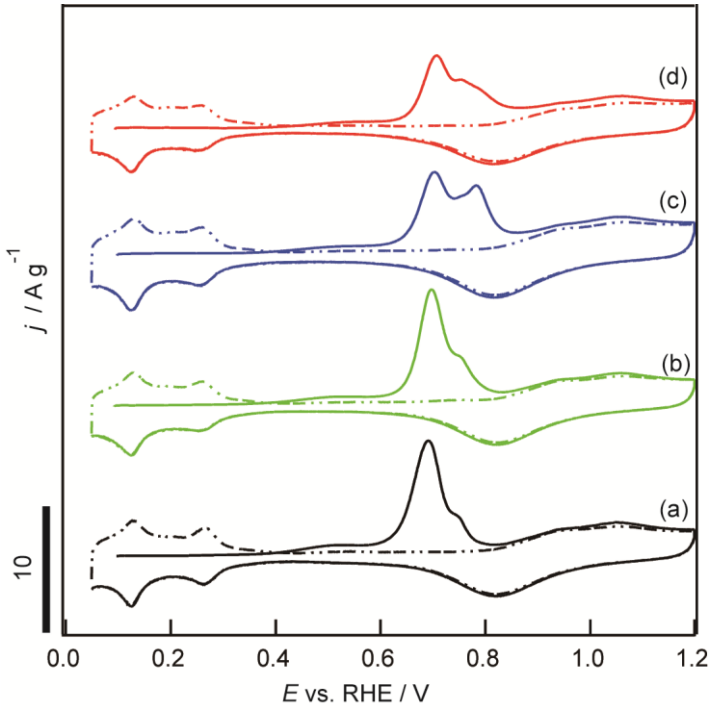

Figure 4.25 CO_{ad} stripping voltammograms of mp-Au(Y)/Pt; Y = (a) 0, (b) 0.09, (c) 0.17, and (d) 0.21. Solid line: 1st cycle after CO adsorption; dotted line: 2nd cycle.

The unique feature of this study is the use of mesoporous silica as a medium for the formation of an Au-Pt bimetallic structure. Normally it is quite difficult to prepare bimetallic structures possessing exposed surfaces of both metals because conventional techniques do not lead to the formation of well-regulated bimetallic structures. The unique hierarchical structure, and the presence of mesoporosity along with the formation of phase-segregated structure (a sort of sandwich structure) reported here may lead to creation of fascinating new nanomaterials, which are expected to be useful for catalytic and electrochemical applications by tuning the composition, metal ratio, the amount of heterojunctions, and so on.

4.3.3 Summary

Mesoporous bimetallic Au-Pt with phase segregated heterostructures was prepared by using SBA-15 as a template. The Au/Pt ratio was controlled by varying the times of Au deposition. The EDX spectral mapping clearly showed that mp-Au(Y)/Pt were composed of Au nanoparticles sandwiched between Pt nanowires. We have demonstrated that the surfaces of the bimetallic Au-Pt heterostructures were electrochemically active owing to the mesoporous structures, as determined by CO_{ad} stripping measurement. The availability of the surfaces of joined bimetallic structure holds a great promise for various applications, such as catalysts and electrodes.

4.4 Conclusion

Mesoporous bimetallic Au-Pt with phase-segregated heterostructures has been prepared by stepwise deposition of Au and Pt within mesoporous silica SBA-15. Mesoporous silica is useful as not only a template for preparation of mesoporous materials but also a reaction field for formation of metal-metal heterojunction. In addition, the surface of the heterojunction was electrochemically active, meaning that Au was not covered with Pt. In order to form such the nanostructure, sizes of metal initially deposited should be comparative to pores sizes of the template. The unique nanostructure and the preparative method reported here can be applied to other compounds, such as metal oxides and carbon, which should contribute to further development of precise design of nanomaterials. In addition, the method will be extended to three- and multi-component systems, which will further expand the possibility of multi-metallic systems. This controllability should also contribute to the fundamental understanding of properties of bimetallic materials.

4.5 Reference

1) a) R. Ferrando, J. Jellinek, R. L. Johnston, *Chem. Rev.* **2008**, 108, 845; b) D. Wang, Y. Li, *Adv. Mater.* **2011**, 23, 1044; c) N. Toshima, T. Yonezawa, *New J. Chem.* **1998**, 22, 1179; d) P. D. Cozzoli, T. Pellegrino, L. Manna, *Chem. Soc. Rev.* **2006**, 35, 1195; e) Q. Yuan, X. Wang, *Nanoscale* **2010**, 2, 2328; f) X. Feng, G. Hu, J. Hu, *Nanoscale* **2011**, 3, 2099.

2) a) S. Zhou, G. S. Jackson, B. Eichhorn, *Adv. Funct. Mater.* **2007**, 17, 3099; b) L. Rivas, S. Sanchez-Cortes, J. V. García-Ramos, G. Morcillo, *Langmuir* **2000**, 16, 9722.

3) Z. Niu, Y. Li, *Chem. Mater.* **2014**, 26, 72.

4) a) Y. Yamauchi, K. Kuroda, *Chem. - Asian J.* **2008**, 3, 664; b) S. Yang, X. Luo, *Nanoscale* **2014**, 6, 4438; c) K. Sekine, Y. Doi, A. Takai, Y. Yamauchi, K. Kuroda, *Chem. Lett.* **2013**, 42, 52; d) K. Ariga, A. Vinu, Y. Yamauchi, Q. Ji, J. P. Hill, *Bull. Chem. Soc. Jpn.* **2012**, 85, 1; e) H. Wang, S. Ishihara, K. Ariga, Y. Yamauchi, *J. Am. Chem. Soc.* **2012**, 134, 10819; f) C. Zhu, D. Du, A. Eychmüller, Y. Lin, *Chem. Rev.* **2015**, 115, 8896.

5) a) H. Ataee-Esfahani, J. Liu, M. Hu, N. Miyamoto, S. Tominaka, K. C. W. Wu, Y. Yamauchi, *Small* **2013**, 9, 1047; b) P. Karthika, H. Ataee-Esfahani, H. Wang, M. A. Francis, H. Abe, N. Rajalakshmi, K. S. Dhathathreyan, D. Arivuoli, Y. Yamauchi, *Chem. - Asian J.* **2013**, 8, 902; c) H. Wang, M. Imura, Y. Nemoto, L. Wang, H. Y. Jeong, T. Yokoshima, O. Terasaki, Y. Yamauchi, *Chem. - Eur. J.* **2012**, 18, 13142; d) Y. Yamauchi, A. Tonegawa, M. Komatsu, H. Wang, L. Wang, Y. Nemoto, N. Suzuki, K. Kuroda, *J. Am. Chem. Soc.* **2012**, 134, 5100.

6) H. Ataee-Esfahani, M. Imura, Y. Yamauchi, *Angew. Chem. Int. Ed.* **2013**, 52, 13611.

7) a) H. Lee, S. E. Habas, G. A. Somorjai, P. Yang, *J. Am. Chem. Soc.* **2008**, 130, 5406; b) B. Lim, H. Kobayashi, T. Yu, J. Wang, M. J. Kim, Z. Y. Li, M. Rycenga, Y. Xia, *J. Am.*

Chem. Soc. **2010**, 132, 2506; c) Q. Yuan, Z. Zhou, J. Zhuang, X. Wang, *Chem. Mater.* **2010**, 22, 2395.

8) a) I. Lee, M. A. Albiter, Q. Zhang, J. Ge, Y. Yin, F. Zaera, *Phys. Chem. Chem. Phys.* **2011**, 13, 2449; b) L. F. Gutiérrez, S. Hamoudi, K. Belkacemi, *Catalysts* **2011**, 1, 97.

9) a) Y. Ren, Z. Ma, P. G. Bruce, *Chem. Soc. Rev.* **2012**, 41, 4909; b) H. Yang, D. Zhao, *J. Mater. Chem.* **2005**, 15, 1217.

10) A. Galarneau, H. Cambon, F. Di Renzo, R. Ryoo, M. Choi, F. Fajula, *New J. Chem.* **2003**, 27, 73.

11) Z. J. Lin, X. M. Chen, Z. M. Cai, M. Oyama, X. Chen, X. R. Wang, *Cryst. Growth Des.* **2008**, 8, 863.

12) a) Y. Xia, Y. Xiong, B. Lim, S. E. Skrabalak, *Angew. Chem. Int. Ed.* **2009**, 48, 60; b) T. H. Tran, T. D. Nguyen, *Colloids Surf. B* **2011**, 88, 1; c) S. E. Lohse, C. J. Murphy, *Chem. Mater.* **2013**, 25, 1250.

13) A. Takai, H. Ataee-Esfahani, Y. Doi, M. Fuziwara, Y. Yamauchi, K. Kuroda, *Chem. Commun.* **2011**, 47, 7701.

14) a) D. Weber, A. J. Sederman, M. D. Mantle, J. Mitchell, L. F. Gladden, *Phys. Chem. Chem. Phys.* **2010**, 12, 2619; b) K. Miyabe, G. Guiochon, *J. Chromatogr. A* **2010**, 1217, 1713.

15) B. E. Feller, J. T. Kellis, L. G. Cascao-Pereira, C. R. Robertson, C. W. Frank, *Langmuir* **2010**, 26, 18916.

16) A. Takai, Y. Doi, Y. Yamauchi, K. Kuroda, *J. Phys. Chem. C* **2010**, 114, 7586.

17) a) S. Kumar, S. Zou, *Langmuir* **2007**, 23, 7365; b) A. Rincón, M. C. Pérez, C. Gutiérrez, *Electrochim. Acta* **2010**, 55, 3152; c) B. Du, Y. Tong, *J. Phys. Chem. B* **2005**, 109, 17775; d) M. D. Obradović, A. V. Tripković, S. L. Gojković, *Electrochim. Acta*

2009, 55, 204; e) F. J. E. Scheijen, G. L. Beltramo, S. Hoeppener, T. H. M. Housmans, M. T. M. Koper, *J. Solid State Electrochem.* **2008**, 12, 483; f) A. Habrioux, W. Vogel, M. Guinel, L. Guetaz, K. Servat, B. Kokoh, N. Alonso-Vante, *Phys. Chem. Chem. Phys.* **2009**, 11, 3573; g) S. Strbac, S. Petrovic, R. Vasilic, J. Kovac, A. Zalar, Z. Rakocevic, *Electrochim. Acta* **2007**, 53, 998.

18) a) A. Takai, Y. Doi, Y. Yamauchi, K. Kuroda, *Chem. - Asian J.* **2011**, 6, 881; b) A. Takai, Y. Yamauchi, K. Kuroda, *Chem. Commun.* **2008**, 4171; c) Y. Yamauchi, A. Takai, T. Nagaura, S. Inoue, K. Kuroda, *J. Am. Chem. Soc.* **2008**, 130, 5426.

19) L. Feng, X. Wu, L. Ren, Y. Xiang, W. He, K. Zhang, W. Zhou, S. Xie, *Chem. - Eur. J.* **2008**, 14, 9764.

20) E. Irissou, F. Laplante, S. Garbarino, M. Chaker, D. Guay, *J. Phys. Chem. C* **2010**, 114, 2192.

21) J. J. Friel, C. E. Lyman, *Microsc. Microanal.* **2006**, 12, 2.

22) Y. Doi, A. Takai, Y. Sakamoto, O. Terasaki, Y. Yamauchi, K. Kuroda, *Chem. Commun.* **2010**, 46, 6365.

23) S. Zhang, Y. Shao, G. Yin, Y. Lin, *Angew. Chem. Int. Ed.* **2010**, 49, 2211.

24) T. Sato, K. Kunimatsu, K. Okaya, H. Yano, M. Watanabe, H. Uchida, *Enery Environ. Sci.* **2011**, 4, 433.

Chapter 4

Chapter 5

Usefulness of Mesoporous Silica as a Template for Preparation of Bundles of Bi Nanowires with Precisely Controlled Diameter below 10 nm

Chapter 5

5.1 Introduction

One-dimensional (1D) nanomaterials, such as nanowires and nanotubes, are attractive materials for potential applications in various areas because of their unique properties owing to finite size effects, anisotropic morphology, and so on.[1] Among various 1D nanomaterials, Bi nanowires are one of the most studied materials regarding both their preparation and properties for fundamental understandings of finite size effects of 1D nanomaterials.[1-2] In addition, the decrease in the diameter of Bi nanowires below 10 nm has been an important target, following theoretical prediction of significant enhancement in thermoelectric performance from confinement effects.[3] However, there still remains a large challenge to reliably prepare such extremely thin Bi nanowires and have good control of the diameter in this size range.

Several preparative methods of Bi nanowires are known, including templating and replicating,[2a,2d-l,4] sputtering,[5] vapour deposition,[6] and solvothermal methods.[7] Although the successful formation of Bi nanowires with diameter below 10 nm was clearly shown in the previous reports using a physical vapour deposition method[6] and a solvothermal method,[7] both of the methods suffered from low uniformity and poor controllability of the diameter. In addition, spherical Bi nanoparticles were undesirably formed as a coproduct in the solvothermal method (the ratio of nanoparticles to nanowires was reported to be *ca.* 4).[6]

For the preparation of Bi nanowires with controlled diameter, a hard-templating method using various solids is promising. In fact, the diameter control of Bi nanowires has been reported in a wide range between *ca.* 0.6 nm to 2 μm by using zeolites,[4a] mesoporous silica,[4b] anodic aluminium oxide,[2d-f,4c-h] polycarbonate membrane,[2a,4i-k] and quartz[2g-l] as templates. However, in the previous reports on Bi nanowires with diameter

below 10 nm, there has been no direct evidence, such as electron microscopy images, to show the successful formation of such thin nanowires after removal of the templates.[2d,2f,4a,4g,4h] One report using mesoporous silica, which is most promising as a template to control the diameter below 10 nm because of its uniform and controllable pore sizes in a range from *ca.* 2 nm to a few tens of nanometers,[8] showed electron microscopy images of products after removal of the template;[4b] however, we should point out that the product did not actually show wire-like morphology replicated from the template. Therefore, a different new preparative method of Bi nanowires with precisely controlled diameter below 10 nm is highly needed.

Here, we report the successful preparation of bundles of thin Bi nanowires with precisely controlled diameter below 10 nm using two-dimensional hexagonal mesoporous silica with different pore sizes (SBA-15[9] and MCM-41[10]) as templates (Scheme 5.1).

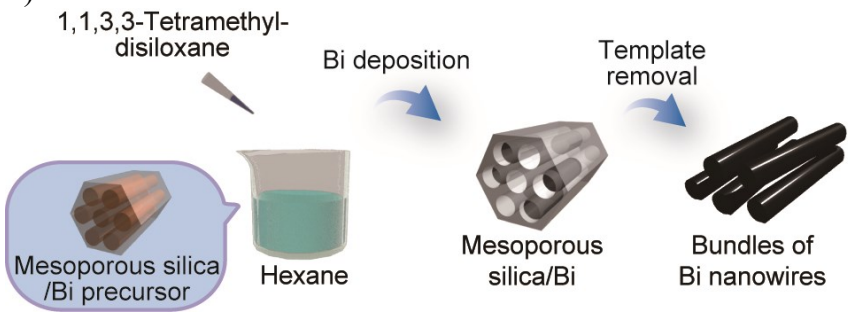

Scheme 5.1 Preparation of thin Bi nanowires using mesoporous silica as a template.

We have employed a liquid phase deposition using hexane and 1,1,3,3-tetramethyldisiloxane as a solvent and reducing agent, respectively, to deposit Bi inside the template.[11] By using the deposition method, Bi was successfully deposited to form nanowires within the mesopores of the templates whose pore sizes were 8.7 nm, 7.6 nm, 6.7 nm, 5.5 nm, and 3.7 nm, respectively. After the removal of the template, the

transmission electron microscopy (TEM) observation clearly showed the successful formation of bundles of Bi nanowires with 8.4 nm, 7.5 nm, and 6.5 nm in mean diameter, although undefined nanostructures were formed when the templates with 5.5 nm and 3.7 nm in pore sizes were used. The diameter distributions of the obtained nanowires were quite narrow, which is due to the uniform pore size of the template. This is the first report that has achieved successful preparation and diameter control of thin Bi nanowires by using mesoporous silica as a template.

5.2 Experimental

5.2.1 Materials

Tetraethoxysilane (TEOS, Kishida Chemical Co.), triblock copolymer $EO_{20}PO_{70}EO_{20}$ (Pluronic 123, Aldrich Co.), hydrochloric acid (35–37 wt%, Wako Pure Chemical Industries Ltd.) were used for the preparation of SBA-15. Hexadecyltrimethylammonium bromide (C_{16}TMAB, Wako Pure Chemical Industries Ltd.) and an aqueous solution of ammonia (25 wt%, Wako Pure Chemical Industries Ltd.) were used for the preparation of MCM-41. Sodium hydroxide (Wako Pure Chemical Industries Ltd.) was used for removal of the silica templates. Bismuth(III) nitrate pentahydrate (Aldrich Co.) was used as a Bi precursor. Acetic acid (Wako Pure Chemical Industries Ltd.) was used as a solvent for incorporation of the Bi precursor into the templates. Hexane (Wako Pure Chemical Industries Ltd.) and 1,1,3,3-tetramethyldisiloxane (TMDS, Tokyo Chemical Industry Co., Ltd.) were used as a solvent and reducing agent, respectively, for the Bi deposition within the mesopores of the templates.

5.2.2 Preparation of SBA-15 and MCM-41

Mesoporous silica SBA-15 were hydrothermally synthesized according to a literature.[9] It has already been known that the pore size of SBA-15 can be controlled by simply varying the temperature of hydrothermal treatment.[9] Therefore, SBA-15 with different pore sizes were synthesized by varying the temperature (100 °C, 80 °C, 60 °C, and 40 °C) for the diameter control of Bi nanowires. The prepared SBA-15 was denoted as SBA-15(X), where X is the temperature of hydrothermal treatment. In order to prepare further thinner Bi nanowires, we focused on and synthesize mesoporous silica MCM-41 whose pore size was much smaller than those of SBA-15(X).[10] The synthesized SBA-15(X) and MCM-41 had ordered two-dimensional hexagonal mesostructures, as determined by their small angle X-ray diffraction (XRD) patterns (Figure 5.1) and transmission electron microscopy (TEM) images (Figure 5.2). The unit cell parameters of SBA-15(X) (X = 100, 80, 60, and 40) and MCM-41 were calculated to be 11.3 nm, 10.7 nm, 10.0 nm, 9.3 nm, and 4.5 nm, respectively, from the d_{10} values of their powder XRD patterns.

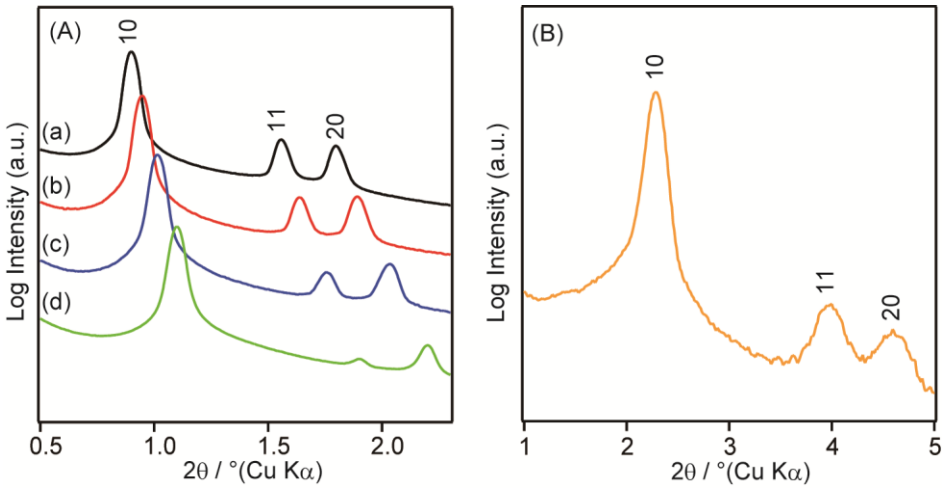

Figure 5.1 Small angle XRD patterns of (A) SBA-15(X) (X = (a) 100, (b) 80, (c) 60, and (d) 40) (Baselines are offset.) and (B) MCM-41.

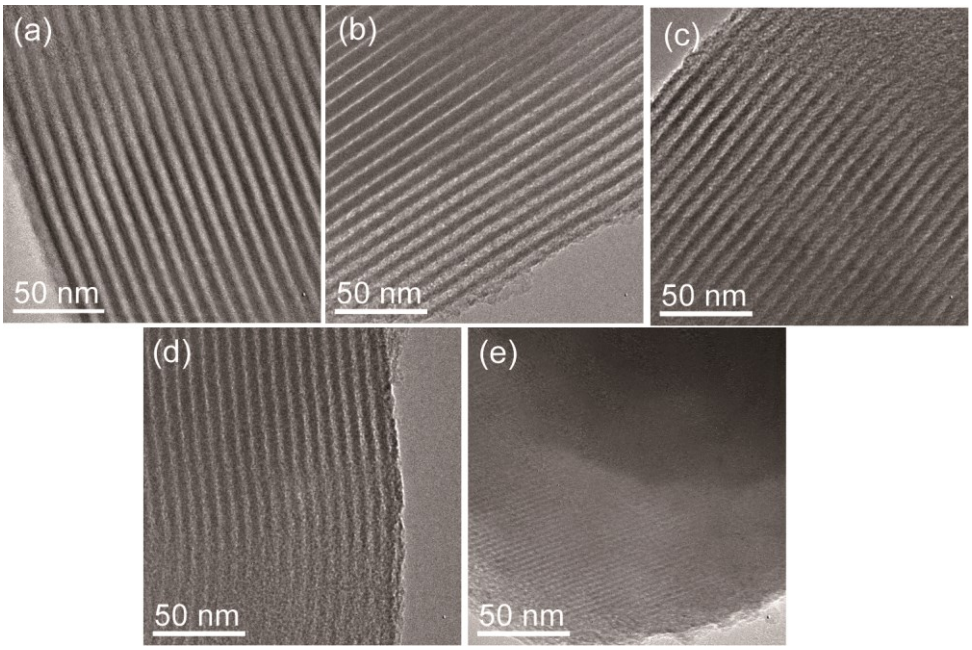

Figure 5.2 TEM images of SBA-15(X) (X = (a) 100, (b) 80, (c) 60, and (d) 40) and (e) MCM-41.

The pore sizes of SBA-15(X) (X = 100, 80, 60, and 40) and MCM-41 were calculated to be 8.7 nm, 7.6 nm, 6.7 nm, 5.5 nm, and 3.7 nm, respectively, by using the non-local density functional theory (NLDFT) method (Figure 5.3B) from the N_2 adsorption-desorption isotherms (Figure 5.3A). The pore volumes of SBA-15(X) (X = 100, 80, 60, and 40) and MCM-41 were calculated to be 1.1 cm^3g^{-1}, 0.92 cm^3g^{-1}, 0.77 cm^3g^{-1}, 0.60 cm^3g^{-1}, and 0.85 cm^3g^{-1}, respectively, on the basis of the volume of adsorbed N_2 at P/P_0 = ca. 0.99.

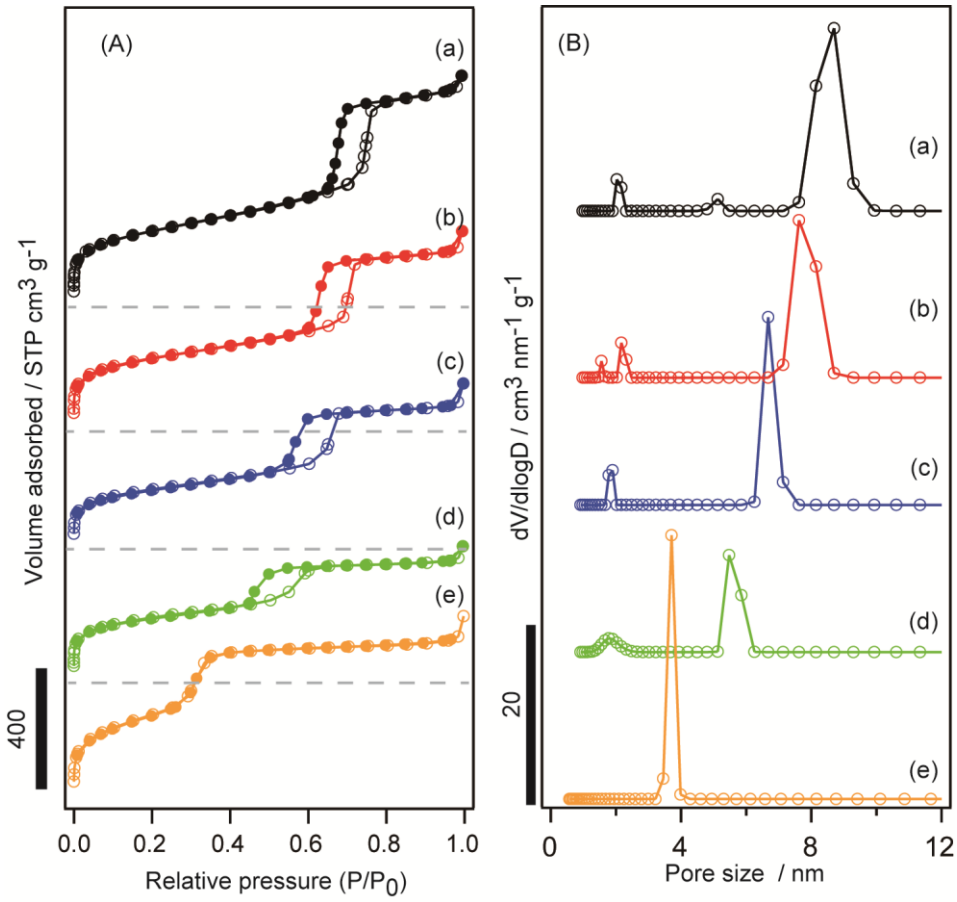

Figure 5.3 (A) N_2 adsorption-desorption isotherms and (B) NLDFT pore size distributions of SBA-15(X) (X = (a) 100, (b) 80, (c) 60, and (d) 40), and (e) MCM-41.

5.2.3 Preparation of bundles of Bi nanowires using SBA-15(X) and MCM-41 as templates

The obtained SBA-15(X) (X = 100, 80, 60, and 40) and MCM-41 were dried under reduced pressure at 120 °C for 3 h. A stock solution (0.5 M $Bi(NO_3)_3 \cdot 5H_2O$) was prepared by dissolving $Bi(NO_3)_3 \cdot 5H_2O$ (10 g) in acetic acid (40 mL). The stock solution (0.4 mL) was added to dried SBA-15(X) and MCM-41 (0.1 g), respectively. The volume fraction of the precursor for the pore volume of SBA-15(X) (X = 100, 80, 60, and 40) and MCM-41 are 32 vol%, 38 vol%, 46 vol%, 59 vol%, and 42 vol%, respectively. Accordingly, the expected volume fractions of deposited Bi are 4.0 vol%,

4.8 vol%, 5.7 vol%, 7.3 vol%, and 5.2 vol%, respectively. The volume of the precursor incorporated into the templates should be smaller than the pore volumes to suppress the outer deposition. The wet powders were placed under reduced pressure to incorporate the Bi precursor into the mesopores of SBA-15(X) and MCM-41 until the odor of acetic acid was not detected. The obtained powders were dispersed in hexane (5 mL). Then, TMDS (4 mL, 23 mmol) was added to the solution under stirring. The color of the solution changed from white to black within 2 h. After stirring for 1 d, the hexane solution was filtered. The obtained powders were washed with hexane and ethanol, and dried at room temperature. The obtained samples were denoted as SBA-15(X)/Bi (X = 100, 80, 60, and 40) and MCM-41/Bi, respectively.

In order to remove the silica template, the powders of SBA-15(X)/Bi and MCM-41/Bi (0.1 g) were dispersed in a mixed solution of 2M NaOH aq. (17.5 mL) and ethanol (2.5 mL). After the solution was shaken for 12 h, the powders were recovered by filtration and washed with ethanol and water. The obtained powders were dried under reduced pressure. As mentioned in the results and discussion section, the following three samples were successfully obtained, and they were denoted as Bi-nw(Y), where Y indicates the mean diameter (nm) of the formed nanowires.

5.2.4 Characterization

TEM images, selected-area electron diffraction (SAED) patterns, and energy dispersive X-ray (EDX) spectra were taken by a JEM-2010 microscope (JEOL Ltd.) using an accelerating voltage of 200 kV. High-resolution TEM (HRTEM) images of the sample prepared by the template removal of SBA-15(100)/Bi were conducted on a JEM-2100F microscope (JEOL Ltd.) using an accelerating voltage of 200 kV. Samples

for TEM, HRTEM, SAED, and EDX measurements were dispersed in ethanol, and the solutions were dropped on a carbon-coated microgrid (Okenshoji. Co). Mean diameters, diameter distributions, and the corresponding standard deviation of Bi nanowires were obtained by measuring the diameter of 50 nanowires in the TEM images. X-ray diffraction (XRD) patterns at small diffraction angles were recorded with a NANO-Viewer (Rigaku Co.) using CuKα radiation under the operating conditions of 40 kV and 30 mA and a Pilatus 2D X-ray detector (Dectris). N_2 adsorption-desorption isotherms were measured with a BELSORP-max (MicrotracBEL Co.) at –196 °C. Prior to the N_2 adsorption-desorption measurement, samples for measurement were heated at 120 °C under reduced pressure. The pore size was determined by using adsorption data. High-angle XRD patterns were recorded with a RINT-Ultima III diffractometer (Rigaku Co.) using CuKα radiation under the operating conditions of 40 kV and 40 mA and a high-speed 1D X-ray detector (D/teX Ultra). Inductively coupled plasma optical emission spectroscopy (ICP-OES) analysis was conducted on an iCAP 6500 Duo-ICP-OES (Thermo Fisher Scientific K.K.). Fourier transform infrared (FT-IR) spectra of SBA-15(X)/Bi and MCM-41/Bi IR were obtained with a FT/IR 6100 spectrometer (JASCO Co.) by a KBr disc method. X-ray photoelectron spectroscopy (XPS) profiles were measured with a PHI 5000 VersaProbe II (ULVAC-PHI, Inc.) using monochromated AlKα radiation. The peak shift due to the charging was corrected by using the C 1s core-level peak at 284.8 eV as a reference. In order to characterize the internal chemical state of Bi nanowires, the surfaces were bombarded by Ar ions with an ion acceleration voltage of 1 kV for total time of 30 s.

5.3 Results and discussion

5.3.1 Characterization of SBA-15(X)/Bi and MCM-41/Bi

The obtained powders of SBA-15(X)/Bi and MCM-41/Bi were grey in colour, suggesting the formation of Bi metals. The TEM images of SBA-15(X)/Bi and MCM-41/Bi showed that Bi was successfully deposited inside the template to form nanowires replicated from the template (Figure 5.4). As observed in Figure 5.4, Bi was not fully deposited within the mesochannels, which is a usual phenomenon for the hard-templating method.[12] This is due to inhomogeneous infiltration of metal precursors into mesopores and/or migration of metal species between mesopores during metal deposition.

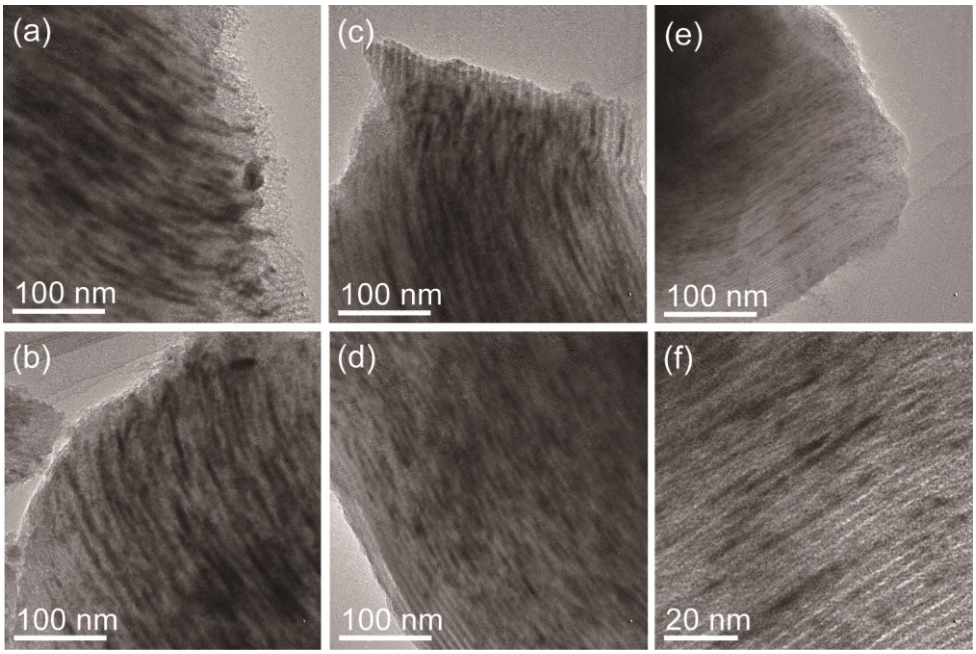

Figure 5.4 TEM images of SBA-15(X)/Bi (X = (a) 100, (b) 80, (c) 60, and (d) 40) and (e), (f) MCM-41/Bi.

In the small angle XRD patterns of SBA-15(X)/Bi and MCM-41/Bi (Figure 5.5), the intensities of the peaks became weaker than those of the original templates, indicating the Bi deposition inside the templates.

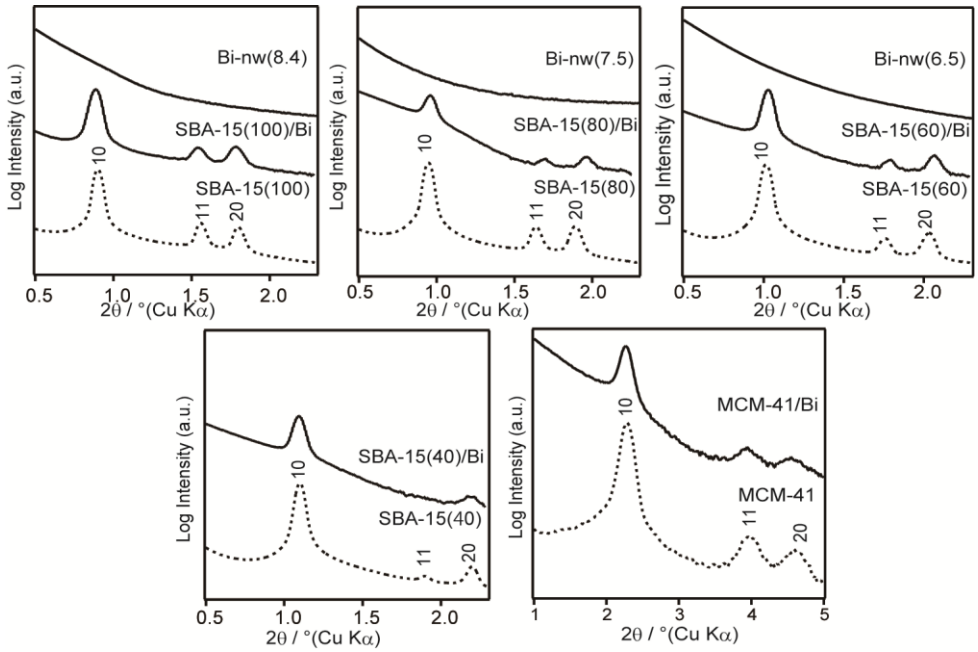

Figure 5.5 Small angle XRD patterns.

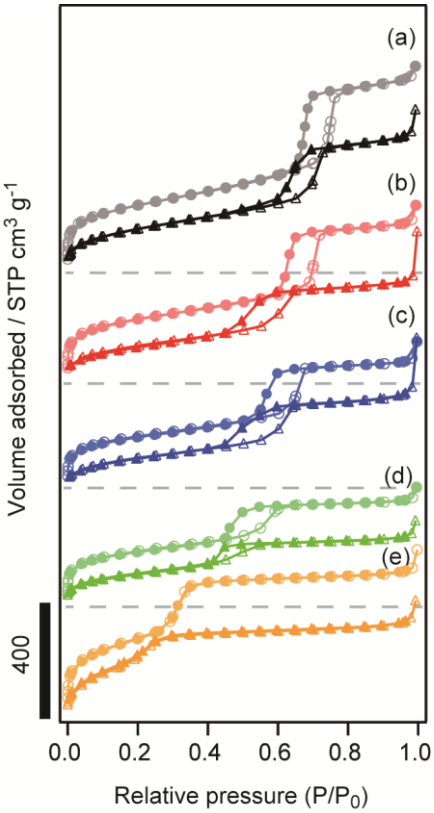

Figure 5.6 N_2 adsorption-desorption isotherms of SBA-15(X)/Bi (X = (a) 100, (b) 80, (c) 60, and (d) 40), and (e) MCM-41/Bi; Circle plots and triangle plots indicate isotherms of the original templates (the reprint of Figure 5.3A) and the templates after the Bi deposition, respectively.

The decrease in the amount of adsorbed nitrogen in N_2 adsorption-desorption isotherms (Figure 5.6) indicated the successful inside deposition. The shifts of the hysteresis loops to lower relative pressure are mainly explained by the surface modification with TMDS, which is one of the characteristics of the reducing agent,[11] as proved by FT-IR measurements (Figure 5.7).

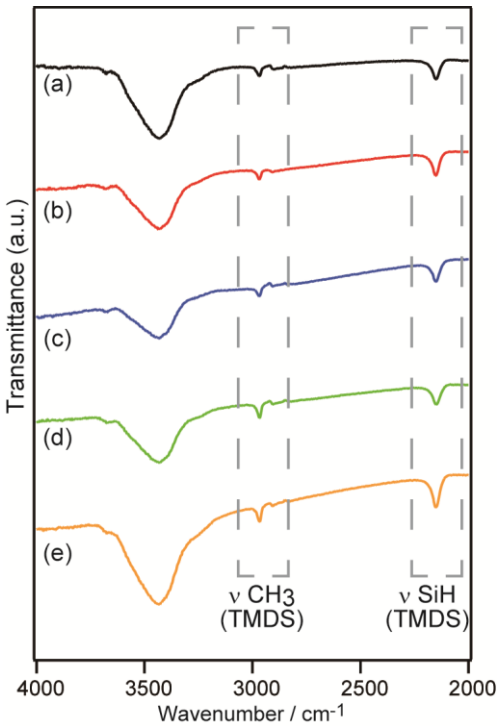

Figure 5.7 FT-IR spectra of SBA-15(X)/Bi (X = (a) 100, (b) 80, (c) 60, and (d) 40) and (e) MCM-41/Bi. Three bands were observed at around 2970 cm^{-1} (CH_3 sym stretching), 2890 cm^{-1} (CH_3 asym stretching), and 2150 cm^{-1} (Si-H stretching), indicating the surface modification with TMDS.

Most of the deposited Bi formed nanowires within the mesopores as far as we observed. However, Bi bulk particles formed by outer deposition were also slightly observed for all the samples studied here (typical image of SBA-15(100)/Bi is shown in Figure 5.8) even though the templates possessed enough pore volumes to accommodate

all the deposited Bi as described in the experimental section. The reason for such an outer deposition is not clear.

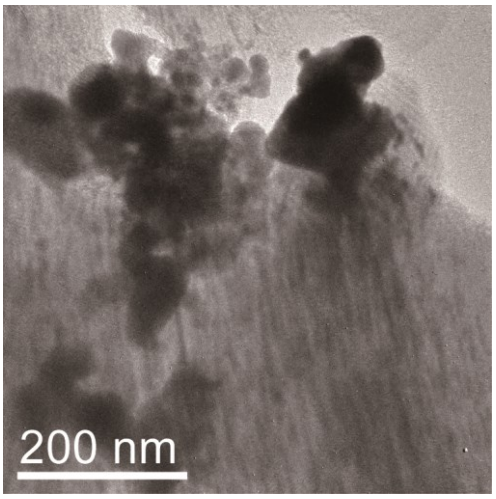

Figure 5.8 TEM image of Bi bulk particles formed by the outer deposition observed for SBA-15(100)/Bi.

The successful deposition of Bi within mesopores can be explained by the following process. The non-polar solvent and reducing agents confined the Bi precursor inside the templates and suppressed the migration of Bi species during the deposition, as described in detail in our previous report on Au deposition.[11] The mild condition of the present deposition process is also a key for the successful deposition of Bi inside the templates because of low melting point of Bi (m.p. 271 °C). In addition, the deposition method reported here is advantageous from the viewpoint of large laboratory scale preparation, which is essential for the potential application as thermoelectric materials, because the method requires neither special equipment nor large energy consumption. Thermal deposition under H_2 flow and electrochemical deposition are useful and most commonly used for metal deposition inside mesoporous silica so far.[8d] However, the former is not suitable for Bi deposition because of its harsh conditions, while the latter is not good for large laboratory scale preparation. Although there has been one report to

fill the nanochannels of anodic aluminum oxide template with Bi by using high-pressure injection of molten Bi, this technique is not suitable for templates with smaller pore sizes, such as mesoporous silica, because of the high surface tension of molten Bi.[4h] Therefore, we can conclude that the deposition method reported here is valuable as a deposition method of Bi inside mesoporous silica.

5.3.2 Characterization of bundles of Bi nanowires

In the TEM images of the three products prepared by using SBA-15(X) (X = 100, 80, and 60) as a template (Figure 5.9), the bundles of nanowires were clearly observed, and their mean diameters were determined to be 8.4 nm, 7.5 nm, and 6.5 nm, respectively. The diameters are in good agreement with the pore sizes of the templates. The obtained diameters are one of the smallest among those reported previously on Bi nanowires as far as we know.

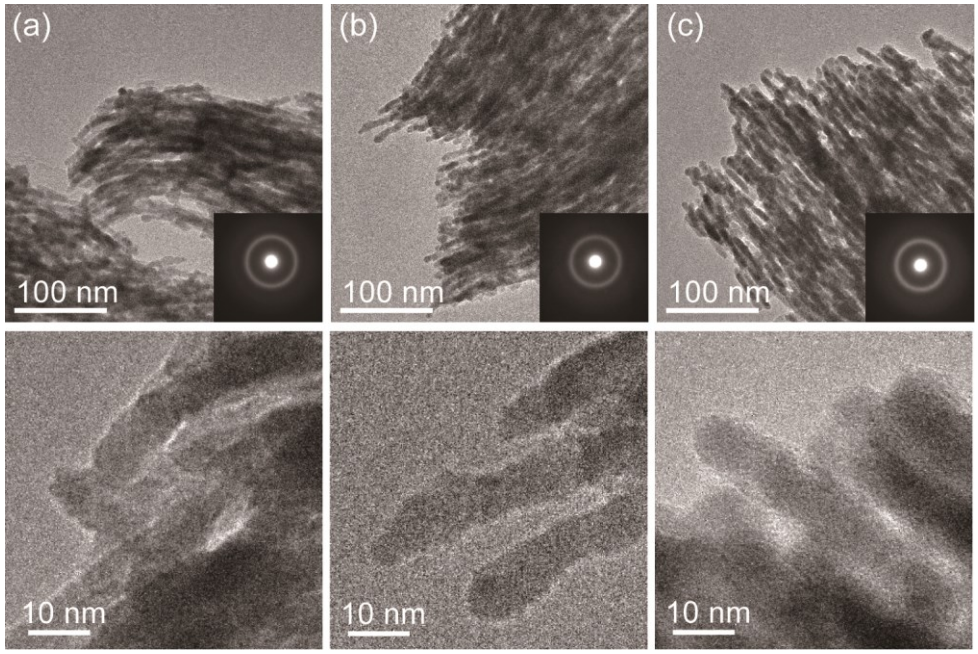

Figure 5.9 TEM images (top and bottom) and SAED patterns (inset) of Bi-nw(Y) (Y = (a) 8.4, (b) 7.5, and (c) 6.5).

It should be noted that the diameter distributions are narrow as shown in Figure 5.10, indicating the preciseness of the control of our synthesis. The standard deviations were calculated to be 3.6 %, 5.9 %, and 3.5 %, respectively. The uniformity of the diameter resulted from the use of mesoporous silica with uniform pore size.

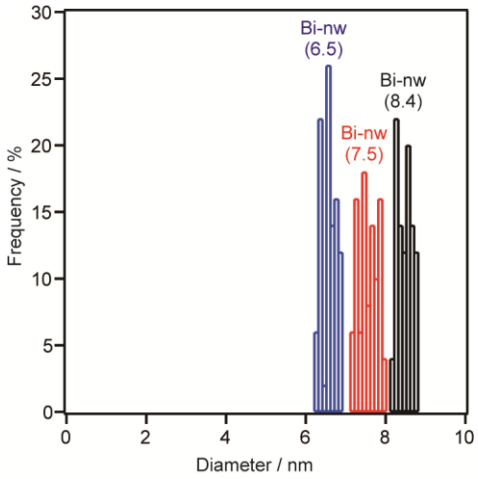

Figure 5.10 Diameter distributions of Bi-nw(Y) (Y = 8.4, 7.5, and 6.5) by measuring the diameter of 50 nanowires in the TEM images.

The ultrasonication (35 W, 1 min) of the products in ethanol solutions to disentangle the bundles resulted in the collapse of the morphology of the nanowires to form somewhat elongated and aggregated nanoparticles. However, it should be emphasized that the diameter of nanoparticles was retained. Such elongated nanoparticles seem to be formed owing to partial structural weakness of each nanowire. (A typical TEM image of Bi-nw(8.4) after ultrasonication is shown in Figure 5.11).

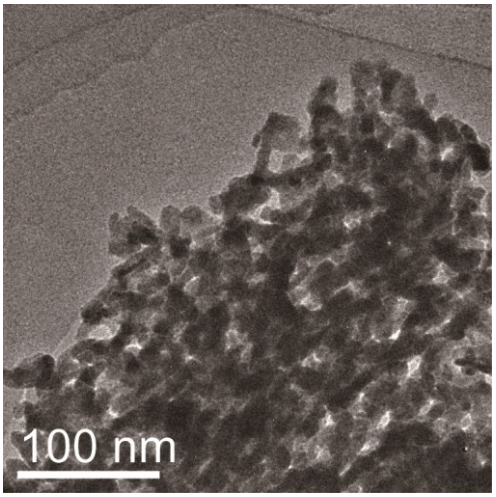

Figure 5.11 TEM images of Bi-nw(8.4) after the ultrasonication (35 W, 1 min) in an ethanol solution.

The successful formation of bundles of Bi nanowires replicated from the templates is due to the filling of the mesopores with Bi as shown in Figure 5.4. In addition, the etching condition of the silica templates is another key to obtain Bi nanowires. Further extension of the etching time resulted in collapse of morphology of Bi nanowires though the amount of Si scarcely changed (Figure 5.12). One reason for the unsuccessful formation of Bi nanowires in the previous report using mesoporous silica would be explained by the collapse of wire-like morphology during the removal of the template due to the relatively harsh condition using 6M NaOH aq.[4b]

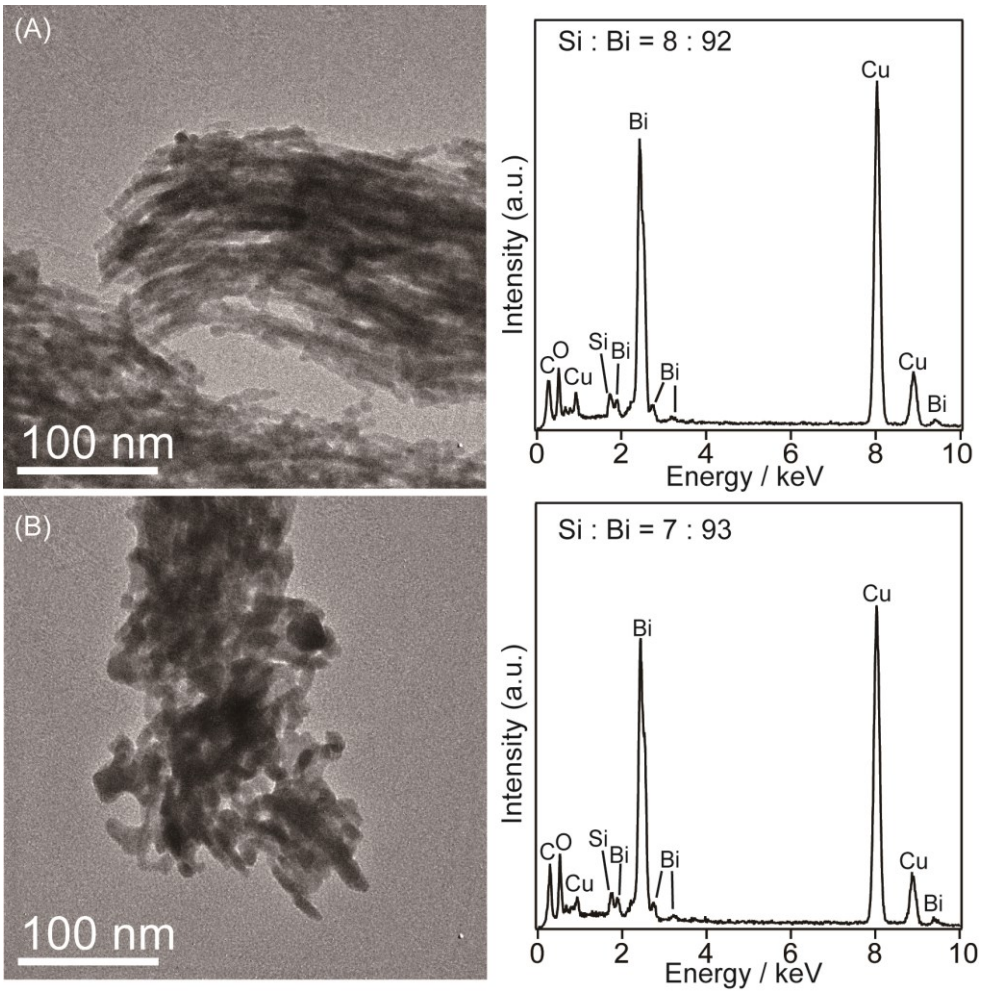

Figure 5.12 TEM images (left) and EDX spectra (right) of Bi-nw(8.4) prepared by shaking SBA-15(100)/Bi in the mixed solution of 2M NaOH and ethanol for (A) 12 h or (B) 24 h. (Figure 5.12A is a reprint of Figure 5.9a) The peaks of C and Cu are due to the TEM grid.

In contrast to Bi-nw(Y) (Y = 8.4, 7.5, and 6.5), the products prepared by the template removal of SBA-15(40)/Bi and MCM-41/Bi did not form bundles of nanowires replicated from the templates but rather resulted in undefined nanostructures (Figure 5.13), although Bi nanowires were indeed formed within the mesopores prior to the template removal as shown in Figure 5.4. From these results, we can surmise that the diameters formed within the mesopores of SBA-15(40) and MCM-41 are too small for Bi to retain the morphology of nanowires under the absence of the templates.

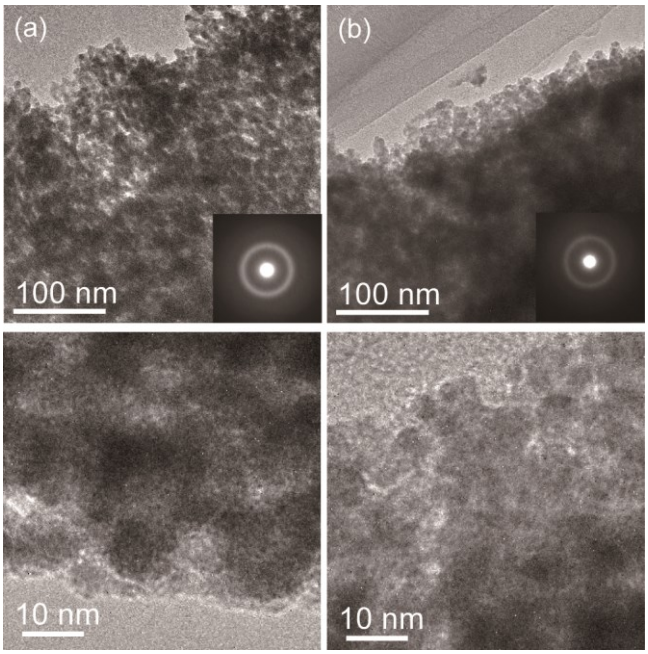

Figure 5.13 TEM images (left and right) and SAED patterns (inset) of the products prepared by the template removal of (a) SBA-15(40)/Bi and (b) MCM-41/Bi.

The small angle XRD patterns of Bi-nw(Y) (Y= 8.4, 7.5, and 6.5) showed no obvious peaks (Figure 5.5). When metals are deposited within both mesopores of SBA-15 and the connecting pores between the mesopores, which is characteristics of SBA-15,[9] nanowires should be bridged and orderly arranged, possessing the same periodicity as that of SBA-15.[12] Therefore, the absence of such peaks at the same position as those of the templates suggests that Bi was not deposited within the connecting pores and nanowires were not bridged. In addition, SBA-15(60) does not possess connecting pores, which is contrast to SBA-15(80) and SBA-15(100) according to the literature.[9] Considering that Bi nanowires were successfully obtained from the three templates (SBA-15(X) (X =100, 80, and 60)), the presence/absence of the connecting pores cannot be a reason for the retention of the morphology after the template removal.

In order to characterize the crystal structure of the obtained nanowires,

HRTEM observation and SAED measurements were performed. As a result, no lattice fringes were observed in the HRTEM image of Bi-nw(8.4) (Figure 5.14).

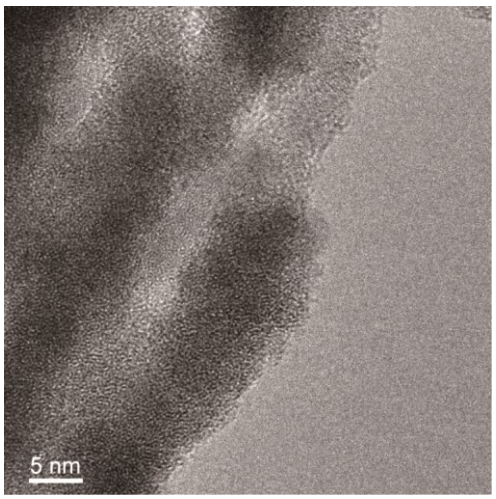

Figure 5.14 HRTEM image of Bi-nw(8.4).

The *d*-values calculated from the ring patterns in the SAED patterns were almost same as those of liquid Bi (Figure 5.9 inset).[13] In addition, the same patterns were also observed in the SAED patterns of the products prepared by the template removal of SBA-15(40)/Bi and MCM-41/Bi (Figure 5.13 inset). These results mean that the obtained products were non-crystalline. In contrast, the SAED patterns of the bulk particles formed by the outer deposition showed spot patterns attributed to rhombohedral crystal structure of Bi (Figure 5.15). Therefore, it is clear that the formation of non-crystalline Bi was caused by the deposition within confined nanospace of the template. The formation of non-crystalline Bi within mesoporous silica should be related to the following points; low melting point of Bi (*ca.* 271 °C) and depression of the melting point due to the high surface to volume ratios in the nanoscale region.[14] Although a lot of studies have been reported on deposition of various metals within mesoporous silica so far, the formation of such non-crystalline metals within

mesoporous silica is quite rare.

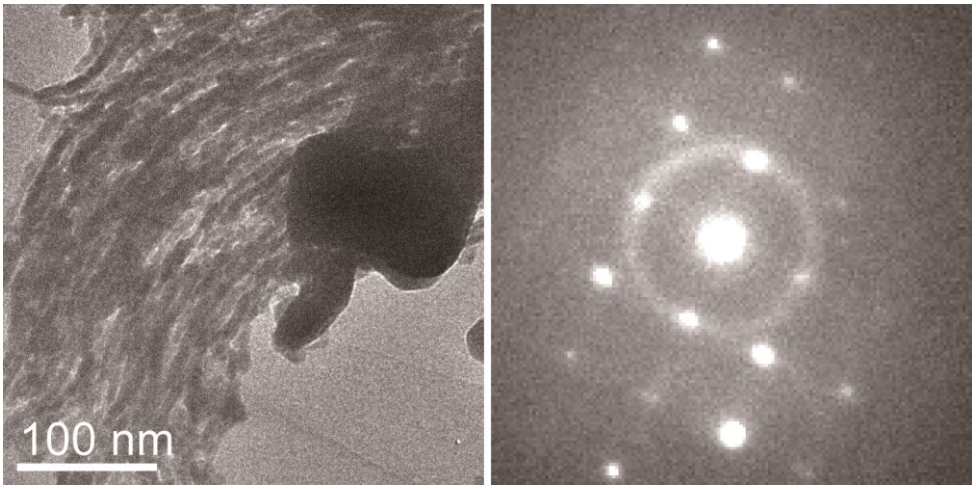

Figure 5.15 TEM image (left) and SAED pattern (right) of Bi bulk particles observed for Bi-nw(8.4).

The surface chemical states of Bi-nw(Y) (Y= 8.4, 7.5, and 6.5) were analysed by XPS combined with Ar ion sputtering (Figure 5.16). In the XPS profiles before the Ar ion sputtering, the peaks observed at around 102 eV, 158.6 eV, and 164.2 eV were assigned to Si 2p, Bi $4f_{7/2}$, and Bi $4f_{5/2}$, respectively. The presence of the peaks due to Si 2p indicated the incomplete removal of the silica templates. The binding energy of Si 2p was lower than that of SBA-15(100) by more than 1 eV. In addition, the binding energies of Bi $4f_{7/2}$ and Bi $4f_{5/2}$ were higher than those of commercial Bi_2O_3 powder (158.2 eV and 163.6 eV). These shifts of the binding energies were well explained by the formation of Bi-O-Si bond.[15] Thus, the surfaces of Bi nanowires were covered with Si oxides, and Bi atoms on the surfaces formed Si-O-Bi bonds with the surface Si oxide layers. The formation of the chemical bonds between the templates and the replicas would be the reason for the incomplete removal of the templates as reported on template synthesis of nanostructured TiO_2 using mesoporous silica.[16] Although the presence of Si

species on the surface may affect the properties of Bi nanowires, Si species should have a positive influence on the structural stability of Bi nanowires.

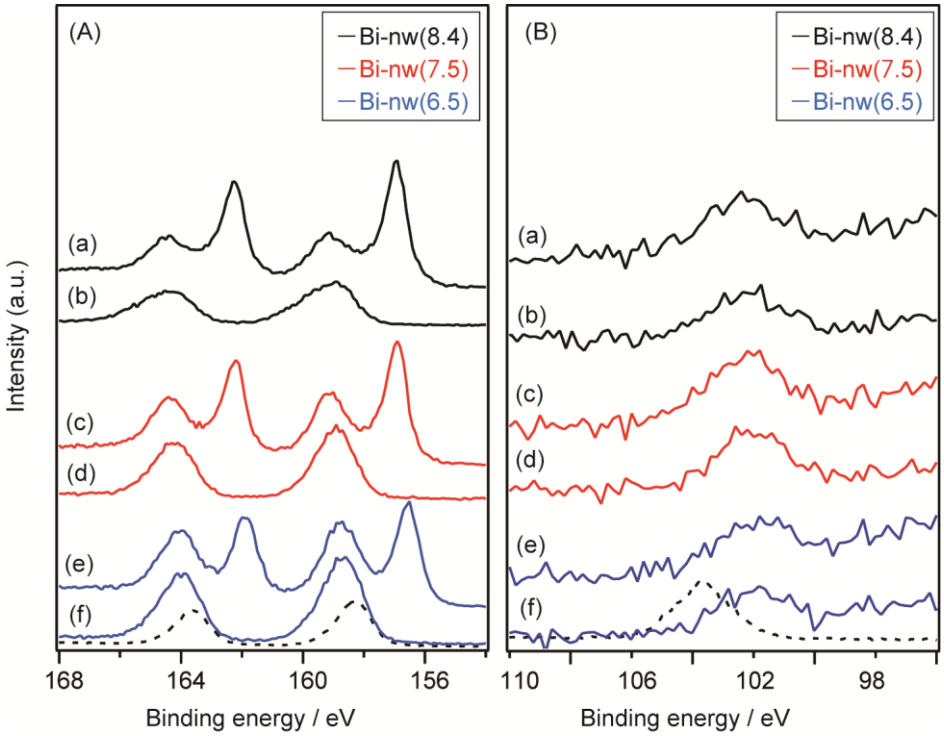

Figure 5.16 XPS profiles. Solid line: Bi-nw(Y) (a, c, e) after and (b, d, f) before Ar ion sputtering for (A) 154–168 eV and (B) 96–110 eV; dotted line: Commercial Bi_2O_3 powder (99.0 %, Wako Pure Chemical Industries Ltd.) for (A) 154–168 eV and SBA-15(100) for (B) 96–110 eV.

After the Ar ion sputtering, the peaks at 162.2 eV and 157.0 eV were newly observed in the profiles of Bi-nw(Y) (Y= 8.4, 7.5, and 6.5). These peaks were assigned to Bi_0, meaning that the Bi precursor was fully reduced, and the interior of the nanowires was not oxidized. The peaks at 102 eV, 158.6 eV, and 164.2 eV due to the surface oxide layers as mentioned above were also observed, which was attributed to the presence of unetched particles of Bi-nw(Y) (Y= 8.4, 7.5, and 6.5) even after 30 s sputtering.

Although it is difficult to estimate the thickness of the surface Si oxide layers

accurately from the XPS profiles, the thickness should be thin. The Si/Bi ratios of Bi-nw(Y) (Y= 8.4, 7.5, and 6.5) were calculated to be 0.09, 0.12, and 0.13, respectively, on the basis of the data of ICP-OES measurements, and the data are well consistent with those calculated from the EDX measurements (Figure 5.17). These Si/Bi ratios were smaller than the roughly calculated surface/interior atom ratios of Bi nanowires with 8.4 nm, 7.5 nm, and 6.5 nm in diameter (0.12, 0.14, and 0.16, respectively). This suggests that the number of the surface Si oxide layers was no more than one.

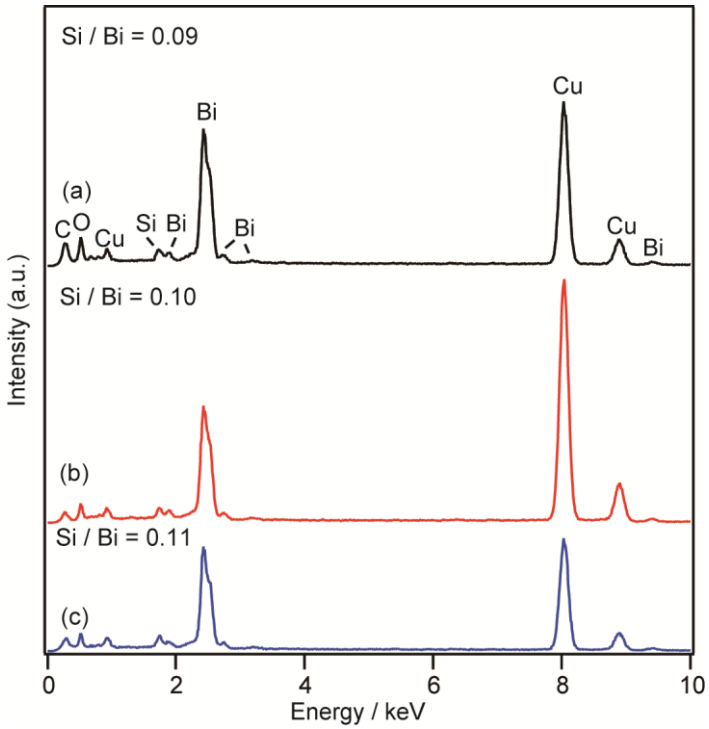

Figure 5.17 EDX spectra of Bi-nw(Y) (Y = (a) 8.4, (b) 7.5, and (c) 6.5).

As shown above, the obtained bundles of thin Bi nanowires were almost non-crystalline. While, unique properties, such as the significant increase in thermoelectric performance from confinement effects, are unlikely to be obtained immediately, it is important that the proper morphology was able to be obtained. This study is meaningful as the first report that has achieved the preparation of thin Bi

nanowires with uniform diameter and highly precise control of their diameters in the range below 10 nm using mesoporous silica as a template. The fact that the same deposition method can be applicable to mesoporous silica with different pore sizes should also be noted because metal depositions within mesopores are often unsuccessful when the pore sizes of the templates are varied.

5.4 Conclusion

In conclusion, we have demonstrated the usefulness of mesoporous silica as a template for preparation of the bundles of thin Bi nanowires below 10 nm and precise control of the diameter. The diameters of the obtained nanowires were uniform, which is due to the use of mesoporous silica with the uniform pore sizes. In addition, the diameter was successfully controlled between *ca.* 6 nm to 9 nm by varying the pore sizes of the templates. The obtained diameters were one of the thinnest ones among those reported previously on Bi nanowires even though the nanowires were non-crystalline. The reliable formation of such thin Bi nanowires opens up exciting new possibilities as the basic enhanced control of morphology, and once higher crystallinity is achieved, 1D physical phenomena such as finite size effects and confinement effects can be probed.

5.5 References

1) a) Y. Xia, P. Yang, Y. Sun, Y. Wu, B. Mayers, B. Gates, Y. Yin, F. Kim, H. Yan, *Adv. Mater.* **2003**, 15, 353; b) L. Cademartiri, G. A. Ozin, *Adv. Mater.* **2009**, 21, 1013; c) Z. Li, Q. Sun, X. D. Yao, Z. H. Zhu, G. Q. Lu, *J. Mater. Chem.* **2012**, 22, 2282.

2) a) M. E. Toimil Molares, N. Chtanko, T. W. Cornelius, D. Dobrev, I. Enculescu, R. H.

Blick, R. Neumann, *Nanotechnology* **2004**, 15, S201; b) K. Liu, C. L. Chien, P. C. Searson, *Phys. Rev. B: Condens. Matter Mater. Phys.* **1998**, 58, R14681; c) Y. Zhu, X. Dou, X. Huang, A. Li, G. Li, *J. Phys. Chem. B* **2006**, 110, 26189; d) J. Heremans, C. M. Thrush, Y. M. Lin, S. Cronin, Z. Zhang, M. S. Dresselhaus, J. F. Mansfield, *Phys. Rev. B: Condens. Matter Mater. Phys.* **2000**, 61, 2921; e) K. Hong, F. Y. Yang, K. Liu, D. H. Reich, P. C. Searson, C. L. Chien, F. F. Balakirev, G. S. Boebinger, *J. Appl. Phys.* **1999**, 85, 6184; f) L. Li, Y. Zhang, Y. W. Yang, X. H. Huang, G. H. Li, L. D. Zhang, *Appl. Phys. Lett.* **2005**, 87; g) Y. Hasegawa, M. Murata, D. Nakamura, T. Komine, T. Taguchi, S. Nakamura, *J. Electron. Mater.* **2009**, 38, 944; h) Y. Hasegawa, D. Nakamura, M. Murata, H. Yamamoto, T. Komine, T. Taguchi, S. Nakamura, *J. Electron. Mater.* **2011**, 40, 1005; i) M. Murata, Y. Hasegawa, T. Komine, T. Kobayashi, *Nanoscale Res. Lett.* **2012**, 7, 505; j) M. Murata, H. Yamamoto, F. Tsunemi, Y. Hasegawa, T. Komine, *J. Electron. Mater.* **2012**, 41, 1442; k) Y. Hasegawa, M. Murata, F. Tsunemi, Y. Saito, K. Shirota, T. Komine, C. Dames, J. E. Garay, *J. Electron. Mater.* **2013**, 42, 2048; l) M. Murata, F. Tsunemi, Y. Saito, K. Shirota, K. Fujiwara, Y. Hasegawa, T. Komine, *J. Electron. Mater.* **2013**, 42, 2143.

3) a) L. D. Hicks, M. S. Dresselhaus, *Phys. Rev. B* **1993**, 47, 12727; b) X. Sun, Z. Zhang, M. S. Dresselhaus, *Appl. Phys. Lett.* **1999**, 74, 4005; c) Y. M. Lin, X. Sun, M. S. Dresselhaus, *Phys. Rev. B: Condens. Matter Mater. Phys.* **2000**, 62, 4610; d) R. Venkatasubramanian, *Phys. Rev. B: Condens. Matter Mater. Phys.* **2000**, 61, 3091.

4) a) S. Romanov, *J. Phys.: Condens. Matter* **1993**, 5, 1081; b) J. Xu, W. Zhang, M. A. Morris, J. D. Holmes, *Mater. Chem. Phys.* **2007**, 104, 50; c) X. F. Wang, J. Zhang, H. Z. Shi, Y. W. Wang, G. W. Meng, X. S. Peng, L. D. Zhang, J. Fang, *J. Appl. Phys.* **2001**, 89, 3847; d) Z. Ye, H. Zhang, H. Liu, W. Wu, Z. Luo, *Nanotechnology* **2008**, 19, 085711; e)

Y. Bisrat, Z. P. Luo, D. Davis, D. Lagoudas, *Nanotechnology* **2007**, 18, 395601; f) Z. Zhang, D. Gekhtman, M. S. Dresselhaus, J. Y. Ying, *Chem. Mater.* **1999**, 11, 1659; g) L. Li, Y. Zhang, G. Li, X. Wang, L. Zhang, *Mater. Lett.* **2005**, 59, 1223; h) Z. Zhang, J. Y. Ying, M. S. Dresselhaus, *J. Mater. Res.* **1998**, 13, 1745; i) M. Tian, J. Wang, N. Kumar, T. Han, Y. Kobayashi, Y. Liu, T. E. Mallouk, M. H. W. Chan, *Nano Lett.* **2006**, 6, 2773; j) A. Holtzman, E. Shapira, Y. Selzer, *Nanotechnology* **2012**, 23, 495711; k) Z. Ye, H. Zhang, H. Liu, W. Wu, Z. Luo, *Phys. B: Condens. Matter* **2008**, 403, 1529.

5) a) W. Shim, J. Ham, K. I. Lee, W. Y. Jeung, M. Johnson, W. Lee, *Nano Lett.* **2009**, 9, 18; b) J. W. Roh, K. Hippalgaonkar, J. H. Ham, R. Chen, M. Z. Li, P. Ercius, A. Majumdar, W. Kim, W. Lee, *ACS Nano* **2011**, 5, 3954.

6) H. L. Zhang, W. Chen, X. S. Wang, J. Yuhara, A. T. S. Wee, *Appl. Surf. Sci.* **2009**, 256, 460.

7) H. Yu, P. C. Gibbons, W. E. Buhro, *J. Mater. Chem.* **2004**, 14, 595.

8) a) Y. Wan, H. Yang, D. Zhao, *Acc. Chem. Res.* **2006**, 39, 423; (b) H. Yang, D. Zhao, *J. Mater. Chem.* **2005**, 15, 1217; c) Y. Ren, Z. Ma, P. G. Bruce, *Chem. Soc. Rev.*, **2012**, 41, 4909; d) S. Yang, X. Luo, *Nanoscale*, **2014**, 6, 4438; e) K. Ariga, A. Vinu, Y. Yamauchi, Q. Ji, J. P. Hill, *Bull. Chem. Soc. Jpn.* **2012**, 85, 1.

9) A. Galarneau, H. Cambon, F. Di Renzo, R. Ryoo, M. Choi, F. Fajula, *New. J. Chem.* **2003**, 27, 73.

10) M. Grün, K. K. Unger, A. Matsumoto, K. Tsutsumi, *Microporous Mesoporous Mater.* **1999**, 27, 207.

11) M. Kitahara, K. Kuroda, *RSC Adv.* **2014**, 4, 27201.

12) A. Takai, Y. Doi, Y. Yamauchi, K. Kuroda, *J. Phys. Chem. C* **2010**, 114, 7586.

13) a) M. Takagi, *J. Phys. Soc. Jpn.* **1956**, 11, 396; (b) A. Wurl, M. Hyslop, S. A. Brown,

B. D. Hall, R. Monot, *Eur. Phys. J. D* **2001**, 8, 205.

14) (a) E. A. Olson, M. Y. Efremov, M. Zhang, Z. Zhang, L. H. Allen, *J. Appl. Phys.*, **2005**, 97; (b) G. L. Allen, R. A. Bayles, W. W. Gile, W. A. Jesser, *Thin Solid Films*, **1986**, 144, 297; (c) F. Frongia, M. Pilloni, A. Scano, A. Ardu, C. Cannas, A. Musinu, G. Borzone, S. Delsante, R. Novakovic, G. Ennas, *J. Alloys Compd.*, **2015**, 623, 7.

15) a) M. E. Simonsen, C. Sønderby, Z. Li, E. G. Søgaard, *J. Mater. Sci.* **2009**, 44, 2079; b) G. Qian, X. Luo, J. Wang, *Microporous Mesoporous Mater.* **2008**, 112, 632.

16) W. Yue, C. Random, P. S. Attidekou, Z. Su, J. T. S. Irvine, W. Zhou, *Adv. Funct. Mater.* **2009**, 19, 2826.

Chapter 6

Conclusions

Chapter 6

This thesis describes the usefulness of the stepwise depositions within the silica templates for precise preparation of inorganic nanostructured materials. The deposition methods should be rationally selected, and then the selected methods should be applied in appropriate order for targeted nanostructured materials. In this section, several critical points related to the templating methods using the stepwise deposition are presented on the basis of the contents of this thesis for the preparation of inorganic nanostructured materials.

Chapter 2 describes the preparation of highly ordered mesoporous Nb-doped TiO_2 with single-crystalline frameworks *via* stepwise deposition of TiO_2 within the silica colloidal crystal template. The use of the hydrothermal reaction and the appropriate setting of their reaction conditions are critical for the formation of single crystalline frameworks. The initially deposited TiO_2 within the template can work as a seed to enable the inside deposition of TiO_2 within the template even by using the hydrothermal reaction. In addition, Nb-doping is shown to affect not only crystalline phases but also nanostructures of the replica. These findings provide the preparative method of novel nanostructured metal oxides using silica colloidal crystal templates.

Chapter 3 describes the stepwise deposition of TiO_2 and C within mesoporous silica SBA-15 for preparation of TiO_2 nanoparticles incorporated mesoporous carbon (mesoporous C/TiO_2). The immobilization of titanium oxide layer on the surface of mesoporous silica through covalent bonds between the titanium oxide layer and the surface of the template is critical to obtain anatase TiO_2 with small crystallite sizes. The formation of small crystallite size can be attributed to the suppression of migration of titanium species by the covalent bonds during the crystallization.

Chapter 4 describes the stepwise deposition of Au and Pt within mesoporous

silica SBA-15 for the preparation of mesoporous bimetallic Au-Pt with a phase segregated heterostructure. Section 4.2 describes the usefulness of hexane and 1,1,3,3-tetramethyldisiloxane (TMDS) as a solvent and reducing agent, respectively, to deposit Au exclusively within SBA-15. Furthermore, the addition of hexadecyltrimethylammonium bromide (C_{16}TMAB) as a capping agent is effective to control the morphology of Au within the mesopores. The combining use of the template and capping agent is shown to be valuable to control the nanostructures of Au. Section 4.3 describes the preparation of mesoporous bimetallic Au-Pt with a phase segregated heterostructure through Pt deposition within Au nanoparticles incorporated SBA-15. The frameworks of the prepared mesoporous bimetallic materials are composed of Au nanoparticles sandwiched between Pt nanowires. Mesoporous silica is useful as not only a template for preparation of mesoporous materials but also a reaction field for the formation of metal-metal heterojunctions.

Chapter 5 describes the preparation of Bi nanowires using mesoporous silica as a template. The deposition method using the non-polar compounds described in Chapter 4 is applicable for the inside deposition of Bi. In addition, it is remarkable that the deposition method is also successful for the inside deposition of Bi within the template with different pore sizes between 3.7 nm to 8.7 nm. From the studies in Chapter 4 and 5, the deposition method is expected to be applicable to various metals.

On the basis of the contents of this thesis described above, several critical points related to the templating methods using the stepwise deposition are shown below.

This thesis indicates that the initially deposited compounds can work as a seed to induce the crystal growth of the following deposited compounds even within the templates as shown in Chapters 2 and 4. These findings are quite meaningful as

described below.

In the author's opinion, liquid phase deposition methods, such as hydrothermal deposition and electroless chemical deposition, are ideal to deposit targeted materials within the templates because liquid phase deposition methods are typically superior with regard to the controllabilities of various structural parameters, such as crystal structure, crystallite size, and composition. However, liquid phase deposition methods are unsuitable because a precursor incorporated into template tend to flow to outside due to dissolution. In addition, there is typically no driving force to deposit a targeted compound only inside the template from the precursors in the solution (outside the templates). In contrast, as demonstrated in Chapter 2, inside deposition of TiO_2 can be achieved even by using hydrothermal deposition, which is one of the liquid phase deposition methods, under the presence of the TiO_2 seeds within the template. Considering this result, various liquid phase deposition methods, such as solvothermal deposition and electroless chemical deposition, are applicable to the templating method by stepwisely depositing targeted compounds within the templates, which will enable further precise design of nanostructured materials.

In addition, Chapter 4 shows that the stepwise deposition of two different kinds of metals within the template is quite useful for the formation of bimetallic nanostructures with a phase segregated heterostructure. In general, there are various complicated synthetic factors (e.g., size, shape, and facets of seed metals, combination of two metals, etc.) to be satisfied in order to achieve the anisotropic crystal growth of metals and the formation of the phase segregated structure. In contrast, as demonstrated in Chapter 4, anisotropic crystal growth of Pt from the Au seeds and the formation of the phase segregated structure can be achieved irrespective of the various synthetic

factors by stepwisely depositing the two metals within the template. This concept using stepwise deposition of metals within the template for preparation of bimetallic nanostructures with a phase segregated structure is expected to be applicable to various combinations of metals and multi-metallic system, which leads to creation of novel metallic nanomaterials.

This thesis also indicates that rational separation of the deposition processes into individual steps is valuable for the preparation of nanostructured materials composed of two different compounds as shown in Chapters 3 and 4. In the conventional processes, two different precursors are simultaneously added into the templates. Therefore, it is difficult to apply suitable deposition methods to each component, separately, which leads to the controllabilities of nanostructures of the components. In contrast, as shown in Chapters 3 and 4, the use of stepwise deposition enables the application of appropriate deposition methods to each component, resulting in the improved controllability of the nanostructures.

In the templating method, the deposition process is the most influential on final products. However, the most of previous studies used only the one step deposition methods which have been already known to be applicable to the templating method. Therefore, the deposition methods in the templating method have not been sufficiently developed. As shown in this thesis, the use of stepwise deposition enables precise designs of nanostructured materials which have not been achieved by using the conventional deposition methods. I strongly believe that the concepts of this thesis will stimulate the development of synthetic chemistry of nanostructured materials, and accordingly their material chemistry.

List of Achievements

1. Original articles

(1) M. Kitahara, H. Kamila, A. Shimojima, H. Wada, T. Mori, I. Terasaki, K. Kuroda

"Usefulness of Mesoporous Silica as a Template for the Preparation of Bundles of Bi Nanowires with Precisely Controlled Diameter below 10 nm"

Chem. Asian J., Published online, **2016**. DOI: 10.1002/asia.201501433.

(2) M. Kitahara, S. Kubara, A. Takai, D. Takimoto, S. Enomoto, Y. Yamauchi, W. Sugimoto, K. Kuroda

"Preparation of Mesoporous Bimetallic Au-Pt with a Phase Segregated Heterostructure Using Mesoporous Silica"

Chem. Eur. J., **2015**, 21, 19142–19148.

(3) M. Kitahara, Y. Shimasaki, T. Matsuno, Y. Kuroda, A. Shimojima, H. Wada, K. Kuroda

"The Critical Effect of Niobium Doping on the Formation of Mesostructured TiO_2: Single-Crystalline Ordered Mesoporous Nb-TiO_2 and Plate-like Nb-TiO_2 with Ordered Mesoscale Dimples"

Chem. Eur. J., **2015**, 21, 13073–13079.

(4) M. Kitahara, K. Kuroda

"Preparation of highly controlled nanostructured Au within mesopores using reductive deposition in non-polar environments"

RSC Adv., **2014**, 4, 27201–27206.

2. Other original article (not related to this thesis)

(1) E. Yamamoto, M. Kitahara, T. Tsumura, K. Kuroda

"Preparation of Size-Controlled Monodisperse Colloidal Mesoporous Silica Nanoparticles and Fabrication of Colloidal Crystals"

Chem. Mater., **2014**, 26, 2927−2933.

3. Review article

(1) K. Kuroda, A. Shimojima, K. Kawahara, R. Wakabayashi, Y. Tamura, Y. Asakura, M. Kitahara

"Utilization of Alkoxysilyl Groups for the Creation of Structurally Controlled Siloxane-Based Nanomaterials"

Chem. Mater., **2014**, 26, 211−220.

4. Oral and poster presentations

(1) 鈴木康平, 久原早織, 北原真樹, 下嶋敦, 和田宏明, 黒田一幸

"メソポーラスシリカ表面へのチタニア析出によるシリカ/チタニア複合体の作製と、それを鋳型としたメソポーラスカーボン/チタニア複合体の作製"

第 5 回 CSJ 化学フェスタ, P9-112, タワーホール船堀, 東京 (2015/10)

(2) M. Shoji, M. Kitahara, A. Shimojima, H. Wada, K. Kuroda

"Formation of Au Nanoparticles Embedded in Mesoporous CeO_2"

5th CSJ Chemistry Festa, P6-113, Tower Hall Funabori, Tokyo, Japan (2015/10)

(3) Y. Shimasaki, M. Kitahara, T. Matsuno, Y. Kuroda, A. Shimojima, H. Wada, K. Kuroda

“Fabrication of Nb-doped Single Crystalline Mesoporous TiO_2 by Hard Templating Method”

XVIII International Sol-Gel Conference, P-Tu-5-13, Kyoto University, Kyoto, Japan (2015/9)

(4) M. Shoji, M. Kitahara, A. Shimojima, H. Wada, K. Kuroda

“Preparation of Au Nanoparticles Embedded in the Frameworks of Mesoporous CeO_2”

International Symposium on Zeolite and Microporous Crystals 2015, RRR2-013, Sapporo Convention Center, Sapporo, Japan (2015/7)

(5) Y. Shimasaki, M. Kitahara, T. Matsuno, Y. Kuroda, A. Shimojima, H. Wada, K. Kuroda

“Preparation of Highly Ordered Mesoporous Nb-Doped TiO_2 with Single Crystalline Framework and Plate-like Nb-Doped TiO_2 with Ordered Mesoscale Dimples”

International Symposium on Zeolite and Microporous Crystals 2015, RRR2-012, Sapporo Convention Center, Sapporo, Japan, (2015/7)

(6) 鈴木康平, 久原早織, 北原真樹, 下嶋敦, 和田宏明, 黒田一幸

“メソポーラスシリカ表面への段階的なチタニア析出によるメソポーラスシリカ/チタニアナノ複合体の作製”

セラミックス協会 2015 年年会, 2L04, 岡山大学, 岡山 (2015/3)

(7) 島崎佑太, 北原真樹, 黒田義之, 松野敬成, 下嶋敦, 和田宏明, 黒田一幸
“シリカコロイド結晶を鋳型に用いた Nb ドープ単結晶性 TiO_2 メソ構造体の作製”
セラミックス協会 2015 年年会, 2G30, 岡山大学, 岡山 (2015/3)

(8) 山本瑛祐, 北原真樹, 津村卓也, 黒田一幸
“単分散コロイド状メソポーラスシリカナノ粒子の作製およびコロイド結晶の構築”
第 1 回 ZAIKEN フェスタ, 16, 早稲田大学・東京 (2014/12)

(9) 北原真樹, 久原早織, 高井あずさ, 山内悠輔, 下嶋敦, 黒田一幸
“Au/Pt ヘテロ接合を有する金属ナノ構造体の合成”
第 4 回 CSJ 化学フェスタ, G2-05, タワーホール船堀, 東京 (2014/10)

(10) 北原真樹, Hasbuna Kamila, 黒田一幸, 寺崎一郎
“メソポーラスシリカを鋳型とした Bi ナノワイヤの合成”
第十一回日本熱電学会学術講演会, PS-59,物質・材料研究機構千現地区, 茨城 (2014/9)

(11) E. Yamamoto, M. Kitahara, T. Tsumura, K. Kuroda
“Size Control of Monodisperse Colloidal Mesoporous Silica Nanoparticles and Fabrication of Colloidal Crystals”
The 15th International Union of Materials Research Societies International Conference in Asia, B12-025-008, Fukuoka University, Fukuoka, Japan (2014/8)

(12) M. Kitahara, K. Kuroda
“Controlled Metal (Au, Pt) Deposition only Inside of Mesoporous Silica by Utilizing a Liquid Phase Deposition Process for Preparation of Nanostructured Metals”
7th International Symposium NANOPOROUS MATERIALS-7, 092, Scotiabank CONVENTION CENTRE, Naiagara Falls, Canada (2014/6)

(13) M. Kitahara, H. Kamila, K. Kuroda, I. Terasaki
“Preparation of Bi Nanowires Using Mesoporous Silica”
The 5th NIMS/MANA-Waseda University International Symposium, W-14, NIMS Sengen, Ibaraki, Japan (2014/3)

(14) M. Kitahara, K. Kuroda
“Controlled Au Deposition inside Mesoporous Silica for Preparation of Nanostructured Au”
International Symposium on Integration of Chemistry and Bioscience, P8, Waseda University, Tokyo, Japan (2014/1)

(15) E. Yamamoto, M. Kitahara, T. Tsumura, K. Kuroda
“Preparation of Monodispersed Colloidal Mesoporous Silica Nanoparticles and Fabrication of Colloidal Crystals”
23rd Annual Meeting of MRS-J, K-P9-019, Yokohama Port Opening Plaza, Kanagawa, Japan (2013/12)

(16) 山本瑛祐, 北原真樹, 津村卓也, 下嶋敦, 黒田一幸
“単分散コロイド状メソポーラスシリカナノ粒子の合成およびコロイド結晶の作製”
新学術領域研究「融合マテリアル：分子制御による材料創成と機能開拓」第 8 回若手スクール, 蒲郡市ホテルたつき, 愛知 (2013/11)

(17) M. Kitahara, H. Kamila, K. Kuroda, I. Terasaki
“Preparation of Bi Nanowires Using Mesoporous Silica as a Template”
3th CSJ Chemistry Festa, P7-96, Tower Hall Funabori, Tokyo, Japan (2013/10)

(18) 北原真樹, 下嶋敦, 黒田一幸
“メソポーラスシリカ細孔内での金属(Au, Pt)析出挙動”
セラミックス協会第 26 回秋季シンポジウム, 2C27, 信州大学, 長野 (2013/9)

(19) 山本瑛祐, 北原真樹, 津村卓也, 黒田一幸
“単分散コロイド状メソ構造体シリカナノ粒子の合成および粒径制御”
日本ゾル-ゲル学会第 11 回討論会, 69, 広島大学, 広島 (2013/8)

(20) M. Kitahara, K. Kuroda
“Novel Synthesis Method of Nanostructured Gold by Using Mesoporous Silica as a Template”
8th International Mesostructured Material Symposium, P-1-025, Awaji Yumebutai International Conference Center, Awaji, Japan (2013/5)

(21) E. Yamamoto, M. Kitahara, T. Tsumura, K. Kuroda
“Preparation of Highly Monodispersed Colloidal Mesoporous Silica Nanoparticles”
8th International Mesostructured Materials Symposium, RRR-1-002, Awaji Yumebutai, Hyogo International Conference Center, Awaji, Japan (2013/5)

(22) 北原真樹, 山本瑛祐, 津村卓也, 黒田一幸
“単分散コロイド状メソポーラスシリカナノ粒子の合成およびコロイド結晶の作製”
日本セラミックス協会 2013 年年会, 2F02, 東京工業大学, 東京 (2013/3/18)

(23) 北原真樹, 黒田一幸
“メソポーラスシリカを鋳型とした Au ナノ構造体の新規合成法”
第 28 回ゼオライト研究発表会, A20, タワーホール船堀, 東京 (2012/12)

(24) 東田盛さゆり, 山田紘理, 氏家裕人, 北原真樹, 浦田千尋, 黒田一幸
“有機トリアルコキシシランのみを用いたコロイド状ナノ粒子の作製”
第 2 回 CSJ 化学フェスタ, P1-82, 東京工業大学, 東京 (2012/10)

(25) 北原真樹, 榊原孝記, 黒田一幸

“メソポーラスシリカ/カーボン複合体のマグネシウム還元生成物の検討”
第 1 回 CSJ 化学フェスタ, P7-39, 早稲田大学, 東京 (2011/11)

(26) 北原真樹, 榊原孝記, 黒田一幸

“メソポーラスシリカ／カーボン複合体の Mg 還元生成物の組成と構造”
第 15 回ケイ素化学協会シンポジウム, P7-39, シーパル須磨, 兵庫 (2011/10)

Acknowledgment

I would like to express the deepest appreciation to Professor Dr. Kazuyuki Kuroda for his supervision and valuable advices. I would like to acknowledge Professor Dr. Hiroaki Wada, Professor Dr. Atsushi Shimojima, and Dr. Yoshiyuki Kuroda for their helpful discussions and advices. I would like to acknowledge to Professor Dr. Tetsuya Osaka and Professor Dr. Yoshiyuki Sugahara for their valuable advices and suggestions on my Ph.D. thesis. Also, I would like to acknowledge Professor Dr. Ichiro Terasaki, Professor Dr. Takao Mori, Professor Dr. Yusuke Yamauchi, and Professor Dr. Wataru Sugimoto for their insightful comments and suggestions on my researches. I want to thank Mr. Minekazu Fuziwara, Mr. Shinpei Enotomo, and Mr. Takahiro Goto for their kind and helpful advices on TEM observations, STEM observations, and XPS measurements.

I would like to thank to all laboratory members in Kuroda-Shimojima-Wada group. Thanks to the members, I really enjoy my research life in the laboratory. Especially, I appreciate Dr. Kazufumi Kawahara, Dr. Ryutaro Wakabayashi, and Mr. Takanori Sakakibara for their kind teaching and encouragement. Also, I want to offer my special thanks to Ms. Saori Kubara, Mr. Yuma Komata, Mr. Eisuke Yamamoto, Mr. Takamichi Matsuno, Ms. Hasbuna Kamila, Mr. Kohe Suzuki, Mr. Yuta Shimasaki, and Ms. Miho Shoji for their supporting my researches. In addition, I received many kinds of supports from Mrs. Sadae Himeshima, Dr. Yusuke Asakura, Ms. Maho Kobayashi, Mr. Shintaro Hara, and Mr. Masashi Yoshikawa. I would like to thank them.

I gratefully acknowledge a fellowship (Human Resources Fostering Program in Chemistry) for financial support. Thanks to the fellowship, I can spend all my time on my studies and researches without worrying about money for living and tuition.

Finally, I would like to appreciate my parents, Mr. Tatsuo Kitahara and Mrs. Eiko Kitahara, for a lot of kindly cares.

February, 2016

Masaki Kitahara